Non-linear Finite Element Analyses of the Aortic Heart Valve

Thorsten M. Koch

Department of Mathematics and
Applied Mathematics

University of Cape Town

September 2004

Submitted in fulfilment of the requirements for the degree of

Master of Science in Applied Mathematics

at the University of Cape Town, South Africa.

To my parents
Dieter & Rosi Koch

"Alle Menschen haben Vorurteile, nur von verschiedener Art. Der allein ist davon frei, dem es leicht wird, die Sache aus einem ganz andern Gesichtspunkt zu betrachten."

IMMANUEL KANT [54]

Abstract

Finite element models of the aortic heart valve have been successfully used in the past to gain insight into the mechanics of the valve and to aid in understanding of valve failure. Moreover such models are indispensable tools for further developments in heart valve prosthetic design. In previous stress analyses linear elastic constitutive models have predominantly been used to model aortic valve leaflets, despite aortic valve tissue showing highly non-linear behaviour in tension tests. In view of recent developments towards tissue engineering of heart valves, these linear constitutive models of aortic valve leaflets are not likely to produce results sufficiently accurate to correlate cell behaviour with mechanical stimuli. To study how non–linear material behaviour affects the results of stress analyses of the aortic valve, static finite element analyses of the valve including the aortic root and leaflets have been carried out. An isotropic linear elastic material model was assigned to the aortic root with Young's modulus adjusted for the simulated compliance to match physiological values. Linear elastic models for the aortic valve leaflets with parameters used in previous studies were then compared with hyperelastic materials. The parameters used for the exponential strain energy function of the latter were obtained from fits of uniaxial tension test results of fresh porcine aortic valve leaflets. As natural leaflets show anisotropy with a pronounced stiff direction along the circumference of the valve, isotropic models of the leaflets were extended to account for this behaviour by incorporating transverse isotropy. The results display a stark impact of a transversely isotropic hyperelastic material on leaflet mechanics, i.e. increased coaptation with peak values of stress and strain in the elastic limit. Interestingly, the alignment of maximum principal stress of all models seems to approximately follow the coarse collagen fibre distribution found in aortic valve leaflets.

Ngiyabonga!

I would like to express my deepest gratitude to my supervisor Prof. B. Daya Reddy for his patient guidance that led to the completion of this project.
I would further like to thank Prof. Peter Zilla, who welcomed me in the Cardiovascular Research Unit, that provided a fruitful environment for working on the interface of medicine, biology and engineering. I thus want to thank my co-workers at the group, especially Dr. Deon Bezuidenhout, Dr. Thomas Franz, Ryan Benjamin, Dr. Mark Yeoman, and Louise Bezuidenhout.
I have appreciated many enlightening discussion on heart valves with Dr. Martin Matthäus. He also made the experimental tests on aortic valve tissue possible. In this context I would also like to thank Mr. Raymond Michaels for many trips to the abattoir, and Mr. Len Watkins and Mr. Horst Emrich of the Mechanical Engineering workshop for manufacturing the clamps used to test soft tissue.
I am lucky to have many delightful friends who are a great source of encouragement and inspiration:
Wilnelia Adams, Cindy Arendse, Marlise Baron, Nhlanhla Dlamini, Marion Dümmler, Ahminah Fakier, Dr. Lamiz Fayker, Pakama Gcabo, Keshni Gopal, Anastacia Haddon, Andreas Köster, Laetitia Lukunku, Sonja Marković, Karsten Markus, Nobuhle Mgidi, Dr. Firdows Noor, Roshina Ratnam, Boitumelo Sebambo, Gadija Sonday, and Busi Zondi.
I would furthermore like to express special thanks to my brother Rüdiger, particularly for his never-tiring, contagious and inspiring passion for science.
Lastly, and most importantly, these few words of appreciation certainly fall short of paying tribute to the complete support I am fortunate to enjoy from my parents, Dieter and Rosi Koch.

Contents

List of Figures

List of Tables

Chapter 1

Introduction

1.1 Motivation

Diseased heart valves are routinely replaced with prosthetic devices with reasonable success. There are many prosthetic designs available for that purpose, with two main categories of prosthetic heart valves to choose from. Mechanical valves are produced from biocompatible artificial materials, e.g. a carbon disc mounted on a stent in a way that allows it to tilt open and closed. Bioprostheses on the other hand are derived from natural tissues, e.g. xenografts from porcine heart valves, or auto– and homografts from human valves. Bioprostheses are available either with the tissue mounted on a stent, or stentless in the form of whole aortic roots [162].

Both categories of valve prostheses have their specific advantages and disadvantages. Mechanical valves portray excellent long-term durability, but impose the need for lifelong anticoagulation treatment to prevent the formation of a thrombus at the interface of blood and the artificial surface and possible thromboembolism [47]. They furthermore may produce a disturbing metallic sound [8]. Bioprostheses are haemodynamically superior since no parts of these valves obstruct blood flow in their open position. For immunological reasons these tissues have to be chemically modified, e.g. by treatment with glutaraldehyde [165]. Altered mechanical properties due to this treatment and immune response [71] cause calcification of the tissue with detrimental effects on long-term durability. As a result, they structurally deteriorate about 8 to 12 years after implantation in the aortic position [111].

In view of these characteristics, the choice of a prosthesis and hence the outcome of the operation is largely patient-dependent. Bioprostheses are mostly used in patients older than 60 years only, since structural deterioration leading to failure of these valves is not as severe as in younger patients. For the latter, mechanical valves provide a more durable alternative but due to lifelong anticoagulation treatment, leave the patient an artificial bleeder [111].

The quest for the design of the ideal prosthetic heart valve is therefore still ongoing [164]. The most promising ansatz is probably tissue engineering, the development of a living substitute for the valves. In this approach appropriate cells are seeded onto a scaffold in the shape of the desired heart valve, providing the framework for the cells to produce extracellular matrix material. This engineered tissue has then the potential to adapt to its physiological environment, to remodel and repair itself and maybe even grow [51, 102].

Mechanical stimuli seem to play a vital role in triggering the production of extracellular matrix material [128, 20]. In–depth knowledge of internal stresses and external loads under physiological conditions then becomes important for understanding and eventually controlling this process. This is especially true if a pre–conditioning phase is required prior to implantation to ensure that the engineered tissue possesses the structural integrity to survive in vivo. Suitable mechanical models may aid in optimizing such a process. They may furthermore help in preventing such a tragic outcome of a clinical trial that was recently reported by Simon et al. [133]. Three of the four children with a tissue engineered porcine heart valve died within a year after implantation and the fourth was reoperated prophylactically.

1.2 Computational Models of the Aortic Heart Valve

The usefulness of detailed knowledge of stress and strain in the aortic heart valve for the design and improvement of prostheses was recognized more than 30 years ago. Modern computational methods, in particular the finite element method, can deliver detailed information about the stresses and strains in the valve under physiological conditions. This has first been demonstrated for the aortic valve by Gould et al. [56, 17].

Since then, a lot of work has been done, especially on finite element models of stented prostheses. Sabbah et al. [119, 66] have employed a finite element model of a trileaflet bioprosthesis with isotropic linear elastic material properties in the closed position to shed some light on tissue degeneration. They have later correlated high stress regions with frequent sites of calcification, which is an important factor in bioprosthetic failure [120]. They have further carried out vibrational analyses to calculate fundamental frequencies of intact and damaged porcine bioprosthetic valves [67]. Christie et al. [27] have investigated the role of non-linear and anisotropic material properties of trileaflet bioprostheses and later possible stress reduction by flexible stents [23]. Rousseau et al. [118] have included viscoelastic material properties of bioprosthetic tissue in their model of a closed prosthesis. Krucinski et al. [81, 152] studied the opening mechanics of a bovine pericardium bioprosthesis with an isotropic hyperelastic material model and found reduced flexural stresses if an expansile stent was used. Finite element models have also been used to improve the designs of polyurethane trileaflet heart valves, e.g. Knierbein et al. [80] have used an isotropic linear elastic model to find that their blood pump valve prototype is subject to strains exceeding the long-term failure limit of the material. Chandran et al. [18] have used their model to investigate the design of the stent, while Clift et al. [32] modelled various leaflet shapes to find one with reduced stresses, where both used an isotropic linear elastic model of a polyurethane valve. Cacciola et al. [12, 40] have used similar models to improve the layout of fibre reinforcement in their prosthetic designs. All studies mentioned above drastically simplify the interaction of blood flow with the structural parts of the valve by a static application of pressure. A step in the direction of including fluid-structure interaction in the context of stented bioprosthetic models has been taken by Makhijani et al. [93].

The natural aortic valve operates in a distensible aortic root (discussed in further detail in Chapter 2), which has to be taken into account in finite element models to gain more knowledge of valve mechanics. With the availability of stentless bioprostheses this becomes especially important, particularly for understanding possible failure mechanisms and to discover possibilities for their improvement. Grande Allen et al. [58] have developed a finite element model of the aortic valve including the aortic root from magnetic-resonance images of human valve–root specimens and have used it to investigate the role of anatomical valve asymmetry, which is usually omitted for the sake of saving computational time. They have further used their models to investigate the effects of normal aging [59] by increasing both the thickness and stiffness of the structure and have demonstrated, that this may result in valvular regurgitation. Another application of their model has been a study of aortic root dilation as a cause for valve incompetence [60]. They have shown that root dilation leads to higher stress and strain in the leaflet, which they argue may lead to tissue remodelling in vivo. Furthermore, they have illustrated the applicability of finite element models to clinical questions. A common treatment for aortic valve insufficiency due to aortic root dilation is the valve–sparing procedure, i.e. only the dilated root is surgically replaced, but the natural valve is spared. Grande Allen et al. have shown, by modifying their finite element models to simulate this procedure, that re-creation of the sinus cavities produces stress and strain in the leaflets closer to normal, than a replacement of the root with a cylindrical graft [62] does. They have argued that optimization of the shape and material properties of the graft may result in improved longevity of the spared valve [63]. In all their models they have used static, geometrically linear analyses of the valve in the closed diastolic configuration and have assigned anisotropic linear elastic material properties to the structures. Their model has recently served as the basis for a coupled fluid-structure finite element analysis [105].

Beck et al. [2] have employed similar models, but with constructed valve geometries under the assumption of symmetry. They have also investigated the influence of graft shape of the valve sparing procedure in a static, diastolic model with isotropic linear elastic material parameters and have also come to the conclusion that the presence of the sinuses is important to reduce leaflet stress. Ferraresi et al. [48] have used their model to probe into the opening mechanics of the valve and more recently, Gnyaneshwar et al. [55] have used a dynamic model, with linear elastic material, that has simulated the whole cardiac cycle to shed some light on the interaction of the aortic root and the leaflets. They have found features not reflected in static analyses, e.g. aortic root dilation prior to the opening of the leaflets.

De Hart et al. have recently carried out analyses taking into account fluid–structure interaction in the aortic valve in a model of a stented [41, 42] and a stentless [39] prosthesis, extending earlier work by that group on the fibre layout in reinforced aortic valve prostheses [11]. They have been the first to employ a non–linear material model for the aortic valve leaflets in a simulation of the whole aortic root. Their models were however limited by the assumption of a stress free configuration at diastolic pressure and they have only applied loads with a maximal magnitude of the difference in diastolic and systolic pressure. They have confirmed earlier findings, that fibre reinforcement of leaflets and a distensible aortic root reduce leaflet stress. Their results have furthermore displayed a complete wash-out of blood in the sinus cavities and stabilized systolic leaflet motion in the fibre reinforced leaflet.

The simulation of the aortic valve is a challenging task, as it is a complex structure undergoing large deformation and rotation from the open to closed position, interacting with pulsatile blood flow and exhibiting highly non–linear material behaviour, all of which will be further discussed in Chapter 2. From the above review of previously published models, it is evident, that some simplifications are still necessary to carry out a finite element analysis of the aortic valve, although they become decreasingly restrictive with the improvement of numerical techniques and computational power. Black et al.[7] for instance have highlighted, in an extension of an earlier static diastolic model of a bileaflet bioprosthesis [70], that it is important to use shell elements with bending stiffness as opposed to membrane elements without. One of the most limiting assumptions in many simulations discussed here, is the use of a linear elastic and possibly even isotropic material model for aortic valve leaflets, when an appropriate non–linear anisotropic constitutive model should be used to accurately reflect experimental evidence. Patterson et al.[109, 10] have shown a significant impact on the results with the use of an anisotropic non linear material model in a dynamic analysis of a stented bileaflet bioprosthesis, and later have applied their approach to a stented trileaflet bioprostheses [19]. Likewise, Li et al.[88] have found it important to include anisotropic leaflet properties in their static diastolic model of a stented bioprosthesis to understand failure mechanisms of bioprosthetic heart valves.

1.3 Aims

To address the need for detailed information of aortic valve stresses and strains under physiological conditions, the aim of this thesis is to develop a finite element model of the valve, including a distensible aortic root. In view of the limitations of published work detailed in the previous section, a specific aim is to investigate the influence of the non–linear material properties of aortic valve leaflets in a static finite element model, but subject to full physiological pressures. To this end, an appropriate constitutive model capable of expressing important non–linear features of experimentally determined leaflet material behaviour has been chosen. Analysis results of non–linear leaflets are then compared with linear elastic models. Additionally, isotropic models are extended to incorporate transverse isotropy to account for directional properties of leaflets as observed experimentally.

1.4 Outline of the Thesis

The rest of the thesis is structured as follows. A review of anatomy and physiology of the aortic heart valve relevant for the properties of a finite element model is presented in Chapter 2. Aortic valve geometry and dimensions are discussed in detail in Section 2.1.3 and Section 2.1.4. This chapter furthermore includes a report on uniaxial tension tests of fresh porcine aortic valve tissue in Section 2.2.1. Governing equations of the continuum mechanics framework are summarized in

Chapter 3, along with details on the choice of a constitutive model for valve leaflets in Section 3.2. A portrait of the finite element method in Section 3.3 concludes that chapter. The succeeding Chapter 4 contains a description of the computational models of the aortic valve and discusses the results of the simulations. A detailed description of stress and strain fields in the aortic root in Section 4.2.2 is followed by a presentation of these fields for the various leaflet models in Sections 4.2.3–4.2.6. Details on how the results of these models compare can be found in Section 4.2.7 followed by the Discussion in Section 4.2.8. Final remarks can be found in Chapter 5, preceding some technical details in the appendices.

Chapter 2

The Aortic Heart Valve

In this chapter a brief review of the aortic heart valve is presented, especially of those aspects that function as input data for the computational models discussed later in Chapter 4.

Starting from the location of the valve within the heart, aortic valve anatomy will be presented in further detail. Following a characterization of aortic valve geometry and dimensions, material properties of various parts of the aortic valve are reviewed. A brief look into the microstructure of these parts will enhance interpretation of material properties. Finally, results of uniaxial tension tests of porcine aortic valves conclude the chapter.

2.1 Anatomy and Physiology of the Aortic Heart Valve

2.1.1 The Aortic Valve within the Heart

In humans and other mammals the heart maintains blood pressure and flow through two distinct circuits [13]. The systemic circuit delivers oxygen-rich blood throughout the body and returns oxygen-depleted blood to the heart. The pulmonary circuit transports deoxygenated blood through the lungs for oxygenation. The separation of the circuits is made in the heart by four chambers, two atria and two ventricles, schematically shown in Figure 2.1.

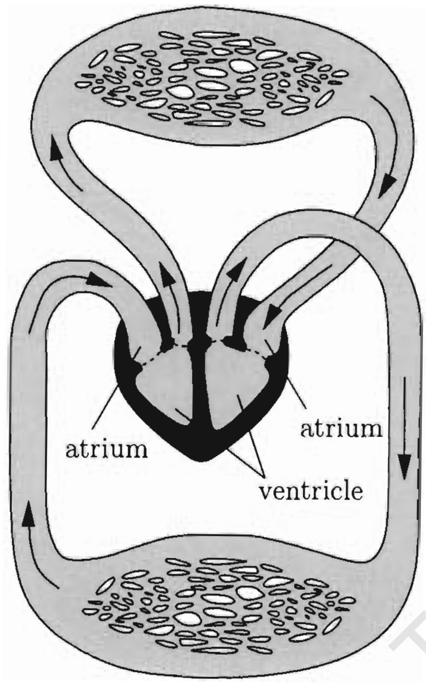

Figure 2.1: The systemic and pulmonary circuits are separated by the four chambers of the heart.

Starting with the pulmonary circuit, oxygen-depleted blood is ejected from the right ventricle, carried through the pulmonary artery to the lungs and returned oxygen-enriched through the pulmonary vein into the left atrium. From here it enters the systemic circuit in the left ventricle, where it is pushed into the aorta, the main artery, from which branches to the rest of the body originate. Deoxygenated blood is returned to the heart by a large vein (in humans the superior vena cava) arriving in the right atrium.

For complete separation of the two circuits the heart has four valves, one each at the in- and outflow of the ventricles as shown in Figure 2.2. There are two atrioventricular valves between the atria and ventricles and two semilunar or arterioventricular valves at the outflow of the ventricles, between the ventricles and the ascending arteries [141]. From the right to the left side of the heart, the four heart valves are:

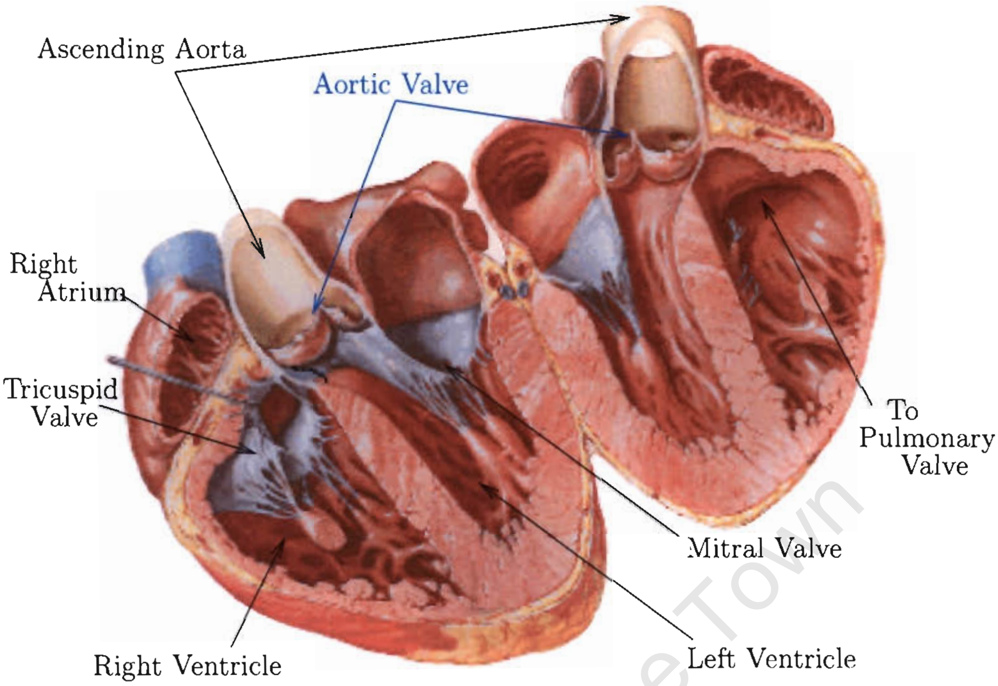

Figure 2.2: Schematic diagram of the heart showing its chambers and valves. Figure modified from [101].

- the tricuspid valve between the right atrium and the right ventricle,
- the pulmonary valve at the outflow of the right ventricle,
- the mitral valve between the left atrium and the left ventricle, and finally
- the aortic valve at the outflow of the left ventricle.

All valves are one-way or check valves [136], regulating the blood flow through the heart in the direction specified earlier and thus, by preventing back flow, enable optimal translation of chamber contraction into blood pressure.

Contraction and relaxation of the heart chambers repeatedly occurs during the cardiac cycle, the pumping of the heart. In humans the average heart rate is about 80 bpm (beats per minute) [129], resulting in a time of about 752 ms for one cycle.

The cardiac cycle is composed of two phases, the filling phase or diastole and the emptying phase or systole. During diastole, which lasts about 64% of the cardiac cycle, both the left and right ventricles fill with blood from the atria and get ready for ejection. Consequently, the atrioventricular valves are open during this phase but the arterioventricular valves are closed, preventing back flow from the arteries. The remaining 36% of the cardiac cycle are spent in systole, the forceful ejection of blood out of the ventricles. During this phase the atrioventricular valves are pushed closed while the pulmonary and aortic valves at the outflows are opened, as illustrated in Figure 2.3.

In view of this a functional characterization of the aortic valve can be given as follows: The aortic valve is a check valve at the outflow of the left ventricle permitting ejection of blood into the aorta during systole but preventing retrograde flow from the aorta into the left ventricle during diastole.

2.1.2 Anatomy of the Aortic Valve

The most prominent feature of the aortic valve is its assembly of three leaflets and three sinuses [65, 141, 138], as shown in Figure 2.4.

The leaflets are the most flexible part of the valve and they undergo the most dramatic changes from the diastolic to systolic configurations, i.e. from the closed to the open positions respectively. Looking from the left ventricle into the ascending aorta, only the load bearing part or the belly of the leaflet can be seen during diastole [141]. The line of leaflet apposition where adjacent leaflets come into contact with each other is referred to as the line of coaptation. A view from the other side onto the closed leaflets reveals that this line is one of the borders of the coaptation surface, the part of the leaflet that is in contact with adjacent leaflets during valve closure. The coaptation surface is also known as the redundant surface or the lunula [138]. The top end of the lunula is the only edge of the leaflet that is not attached to the aortic wall and consequently is named the free edge of the leaflet [141]. At the centre of the free edge there is a little thickening, the node of Arrantius.

The leaflet is attached to the aortic wall at the line of leaflet attachment [141]. The top ends of this line, as viewed from the ventricle, converge with the ones

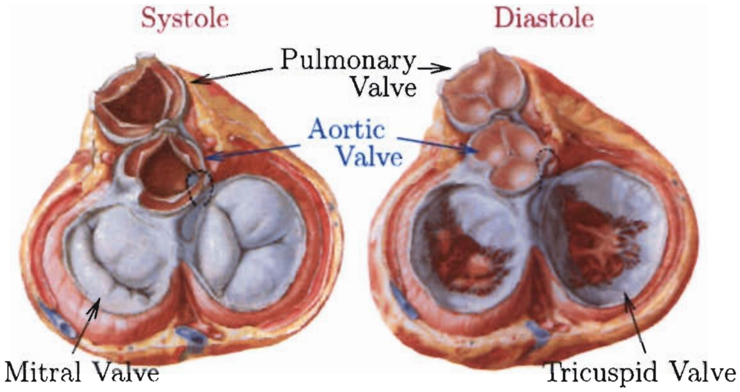

Figure 2.3: Top view of the heart with the semilunar valves open during systole and closed during diastole. Figure modified from [101].

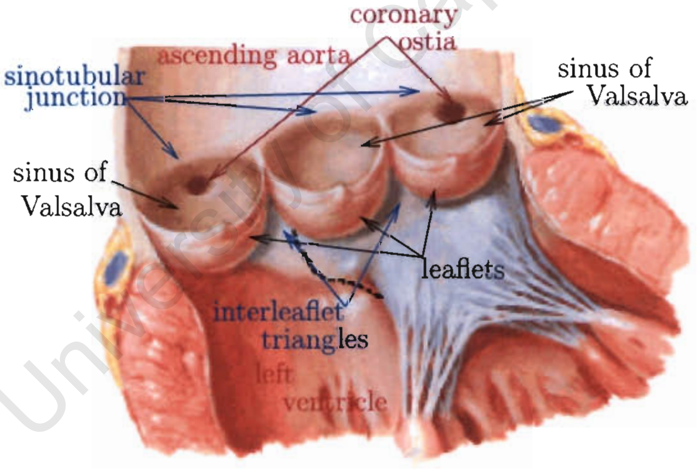

Figure 2.4: Schematic diagram of the developed aortic valve showing the three leaflets, sinuses of Valsalva and coronary ostia. Figure modified from [101].

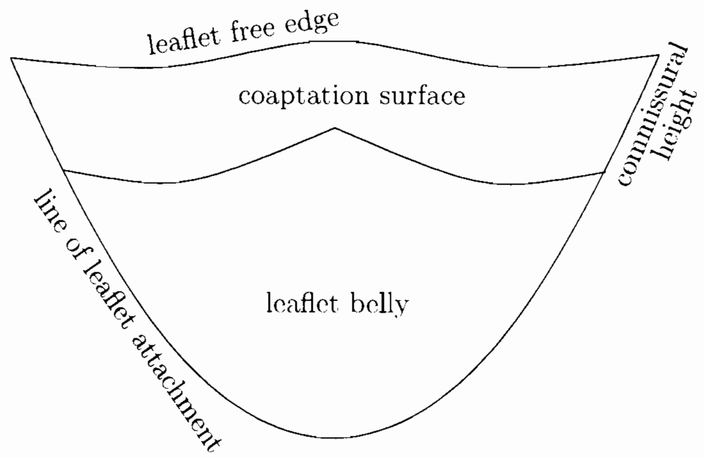

Figure 2.5: Projected view of the open leaflet defining anatomical sites of aortic valve leaflets.

from adjacent leaflets to form the commissures. These are not mere points but small lines and are sometimes referred to as commissural heights [141]. The three lines of attachment of the leaflets form a three-pointed coronet, called the aortic annulus [138], annulus fibrosus [65], fibrous coronet, or somewhat misleadingly, fibrous or aortic ring [141]. The various parts of the leaflet are shown in Figure 2.5.

Ballooning outwards from the aortic wall at the aortic annulus are the three sinuses of Valsalva, which form cavities behind the leaflets [141]. Above the commissural heights they merge with the ascending aorta forming a scalloped line, the sinotubular junction or sinotubular ridge [138], sometimes simply referred to as the top of the sinus cavities [141]. Much like the aortic ring, the sinotubular junction is a coronet-like line, but of lesser height and mirrored, as can be seen in Figure 2.4. In addition to providing space behind the leaflets, two of the sinuses of Valsalva are also the origin of the coronary arteries by means of small ostia, just below the sinotubular junction [112]. Accordingly the individual sinuses and corresponding leaflets are named left coronary, right coronary or non-coronary.

There seems to be no clear definition of the extent of the aortic valve. While a common definition is a span from the aortic annulus to the sinotubular junction [137], it was argued to widen this definition, so that the aortic valve extends from a ring formed by a cut through the lowest points of the aortic annulus up to the sinotubular junction [138]. This ring is referred to as basal ring and it lies slightly beneath the ventriculoarterial junction, where the aorta originates. The lines of attachment of two adjacent leaflets together with the basal ring then form the borders of a three-sided surface, the interleaflet triangles, also shown in Figure 2.4. Henceforth, the term aortic root will refer to the structure between the basal ring and the sinotubular ridge and the term aortic valve will also include the leaflets.

Based on the anatomy of the aortic valve and its leaflets, the following defines the coordinate directions used throughout the rest of this thesis. Figure 2.6 shows the directions to be used for the valve leaflets, defined by imagining a leaflet to be fixed onto a cylinder in such a way, that the commissures lie on a circle of the same height, and the line from the nadir of leaflet attachment to the node of Arrantius is parallel to the cylinder axis. The circumferential direction of the leaflets then coincides with the circumferential direction of the cylinder. The direction along the cylinder axis is the radial direction of the leaflets. And finally the radial direction of the cylinder is the thickness direction of the leaflet. Figure 2.7 shows the directions to be used referring to the aortic root. It is a cylindrical coordinate system defined by the cylinder passing through the basal ring and the sinotubular junction. The circumferential direction of the root again coincides with that of the cylinder. The height, axial or z-direction of the aortic root is defined by lines parallel to the axis of the cylinder. And again the radial direction of the cylinder is the thickness direction of the aortic root.

To further enhance an impression of the aortic valve, pictures of a fresh, excised porcine aortic valve in various views are included in Figure 2.8.

2.1.3 Geometry of the Aortic Valve

The qualitative shape of the aortic valve is consistent among different human specimens [112, 82] and even between different mammalian species [124, 112]. Differences are mostly in dimensions but lie in the range of natural fluctuations within one species [141]. Moreover, it has been reported that the size of the human aortic valve is not correlated to body height or weight and only weakly correlated to body surface area [160]. In terms of absolute numbers the aortic valve is slightly

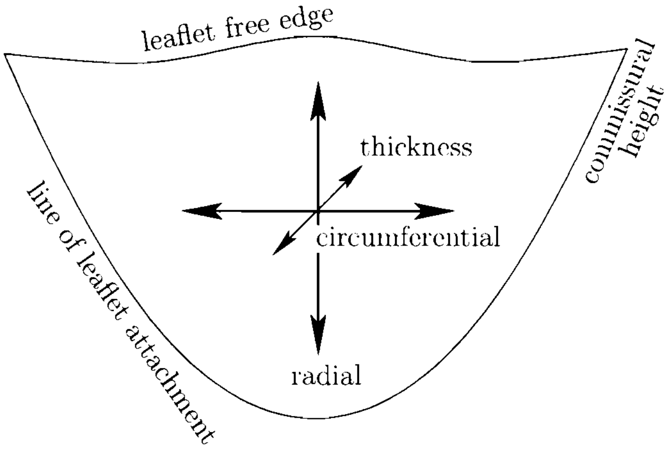

Figure 2.6: Projected view of the open leaflet with an indication of the coordinate directions of aortic valve leaflets.

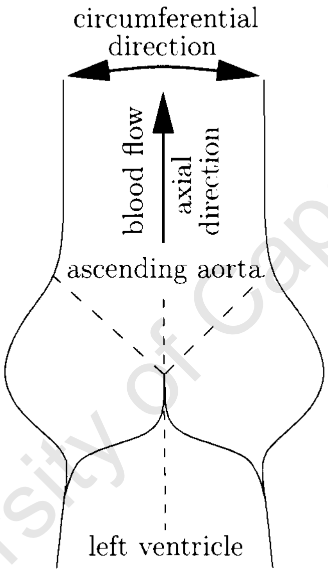

Figure 2.7: Coordinate directions of the aortic root.

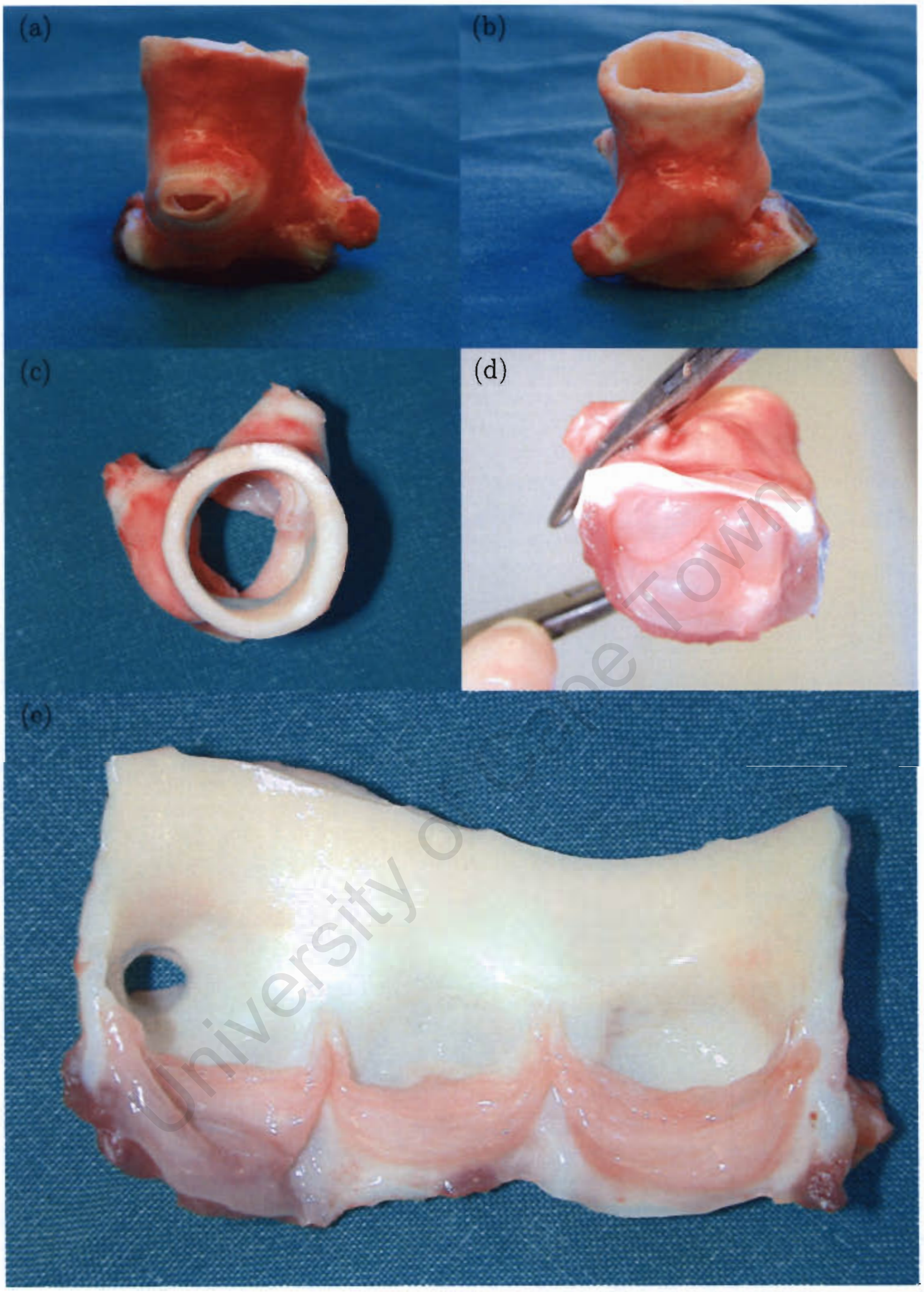

Figure 2.8: Different views of an excised porcine aortic valve. (a) and (b) side views showing the aortic sinuses, coronary ostia and ascending aorta. (c) top view on the relaxed valve in the natural open position. (d) bottom view on the closed valve. (e) developed valve with a clear view on the leaflets.

larger in males [160, 79], but appears to be larger in females when related to body surface area [79]. It seems that the dimensions of the aortic valve are determined by function and that changes exceeding natural fluctuations of its normal geometry can lead to specific valvular diseases [156, 113].

The geometry of the aortic valve has been studied using a variety of techniques: direct measurements on excised hearts at autopsy [156, 79] after fixation in formalin [112, 160, 132, 123], direct measurements on cryopreserved hearts [82], measurements on air inflated aortic roots rapidly frozen in nitrogen [124], measurements on silicone rubber casts made at different pressures [99, 139], measurements on projections of angiographic films [113], and computer tomography scans of cryopreserved roots [21].

When comparing results from these studies it has to be kept in mind that fixation and preservation of soft tissues alters their properties and that results have been obtained at different fixation pressures. All studies resemble the aortic valve in diastole except [113], where measurements have been obtained during mid systole. Furthermore, the dimensions of the aortic valve change with age. It has been observed that the circumference of heart valves increases with age and is most pronounced in the aortic valve [79]. Additionally, the thickness of aortic valve leaflets increases with age [156, 123].

All studies mentioned utilize a limited amount of dimensions to characterize the geometry of the aortic valve or one or more aspects thereof. Such a characterization is only meaningful under a number of geometrical assumptions and only gives a representative approximation of the aortic root. Details of such assumptions will be discussed in what follows.

Most studies report some form of slight asymmetry of the aortic valve [112, 139, 156, 132, 123, 61, 82, 21]. It was noted that the thickness varies from leaflet to leaflet [139], the non-coronary leaflet being the thickest and no significant difference between the left and right leaflets [123]. Size differences between leaflets have been studied and it was found that only in 5 out of the 200 aortic valves studied have they been of the same size. However, a regular pattern of asymmetry was not found [156]. Differences in the size of the sinuses have been noted as well. One study reporting the non-coronary sinus the smallest [139] in contradiction to the more common finding that it is the largest of the three [112, 132, 82, 21]. Only the two most recent investigations report a regular pattern of asymmetry, the non-coronary sinus being the largest, followed by the right coronary sinus, and the left coronary sinus being the smallest [82, 21]. However, only [57, 21] considers this pattern of asymmetry significant and usually the aortic valve is said to have 120° symmetry, consisting of three identical sinuses and leaflets.

The aortic root without the sinuses is a conical frustrum with the larger diameter at the basal plane [112]. The sinuses of Valsalva bulge out from the annulus fibrosus and join the aortic root again at the curved sinotubular junction, the overall shape being ellipsoidal [141]. In fact, they are not merely slight dilations of the aortic root but in systole the greatest depth at the midpoint of the sinus lies on a circle of twice the radius of the conical root at that height [112]. The cross-section at that height can be approximated by an epitrochoid [113]. An epitrochoid is the trajectory of a point within a circle rolling on the perimeter of another circle. In the case of the aortic root the inner circle is three times larger in diameter, so that the outer circle rotated three times on completion of the inner perimeter and thus outlining the three sinuses.

The aortic root can be rotated in such a way that the part of the line of leaflet attachment corresponding to the load-bearing part of the leaflet projects as a straight line [139]. Consequently, this part of attachment lies in a plane. It has been suggested that the line in this plane is a parabola. Furthermore, as deduced from vertical cross-sections through the centre of closed valve rubber casts, the shape of the leaflet belly has been reported to be that of a paraboloid of revolution [99]. However, two of the three cross-sections depicted in that study show a relatively straight profile with no curvature in the radial direction of the leaflet in accordance with the finding of a later study, that the belly is in fact essentially cylindrical [139], i.e. curved only in the circumferential direction of the leaflet. The line of attachment of a cylindrical leaflet forms part of an ellipse [139], not a parabola. This approximation of the load-bearing part of the leaflet seems now to be generally agreed upon [141]. The coaptation surface of the closed leaflet forms two planes [139], resulting in a straight line attachment, forming the commissural heights [99, 141].

2.1.4 Dimensions of the Aortic Valve

Various dimensions of the aortic valve are reported in the studies cited in the previous section. The most complete set of measurements for the purpose of reconstructing the valve geometry is from rubber casts of fresh human aortic valves [139], which is the main source of the dimensions cited here.

From the characterization of valve geometry of the previous section, a limited set of dimensions is sufficient for reconstruction. Together with wall thicknesses of valve leaflets t_l and aortic root walls t_s, only the diameters at the ventricular inlet d_v, the aortic outlet d_a, the diameter of a circle circumscribing the sinuses of Valsalva at greatest depth in a plane normal to the valve axis d_s, the height measured from the lowest point of leaflet attachment to the highest point on the sinotubular junction h_s, the height from the bottom of leaflet attachment to the top of the commissural heights h_l, and finally the height from bottom to top of the leaflet in its centre h_c.

These dimensions are schematically shown in Figure 2.9 together with reported values normalized to the ventricular diameter d_v. These values are averages from rubber casts of five fresh human aortic valves at a pressure of 100 mmHg. They are thus derived from the diastolic valve but seem to better represent valve geometry than averages at 0 mmHg. To get a feel for the size of the human aortic valve, for the reported range of ventricular diameter between 22.0 mm and 28.0 mm, d_s ranges between 31.1 mm and 40.9 mm, h_s between 19.1 mm and 24.4 mm, and h_l and h_c between 15.6 mm and 19.9 mm and 15.4 mm and 19.6 mm respectively. The thickness of the aortic root wall (measured on 10 cryopreserved adult human aortic valves) increases from 0.8 mm at the nadir of the leaflet annulus, to 1.3 mm at the centre of the sinuses, to 1.8 mm at the sinotubular junction [82]. Leaflet thickness ranges between 0.25 mm and 1.33 mm according to the thickness contour map in Figure 2.10.

2.1.5 Aortic Valve Dynamics

As in each living second the aortic valve opens and closes at least once, it is a dynamic structure, virtually never at rest. By preventing retrograde flow into the

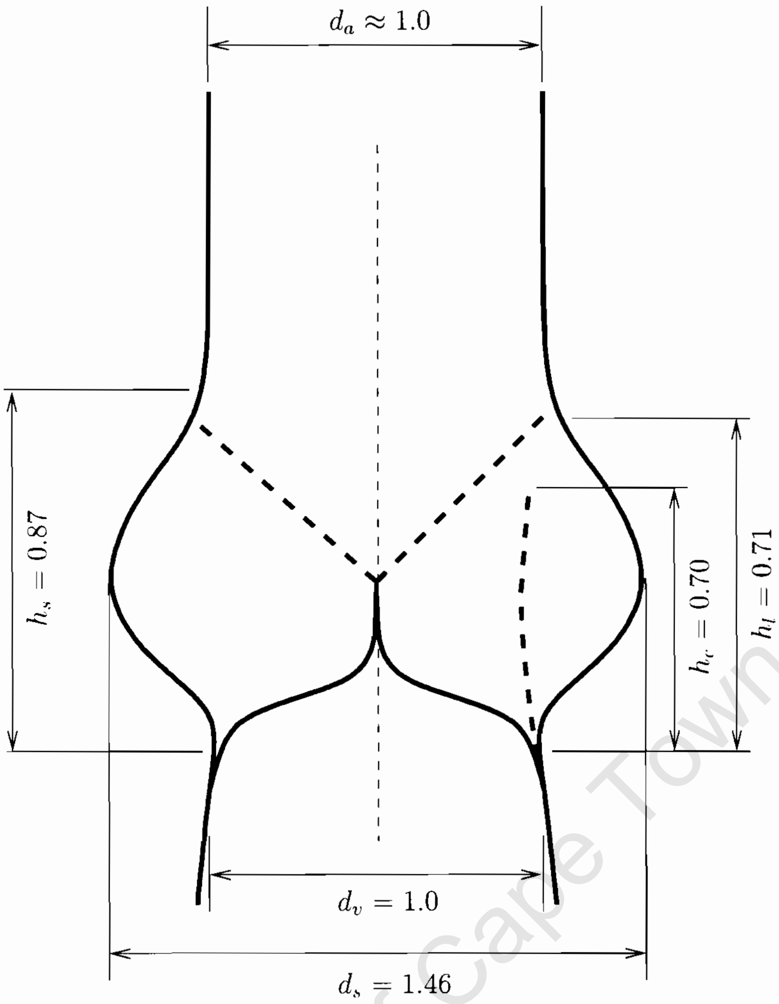

Figure 2.9: Relative dimensions of the aortic valve normed to the ventricular diameter d_v [139]. d_a denotes aortic diameter, d_s the diameter of a circle circumscribing the aortic root in the plane perpendicular to the direction of blood flow at maximum sinus depth. h_s is the maximal height of the sinuses of Valsalva, h_l the height of the open leaflets measured from the base to top of the commissures and h_c the height of the open leaflets from the base to the centre.

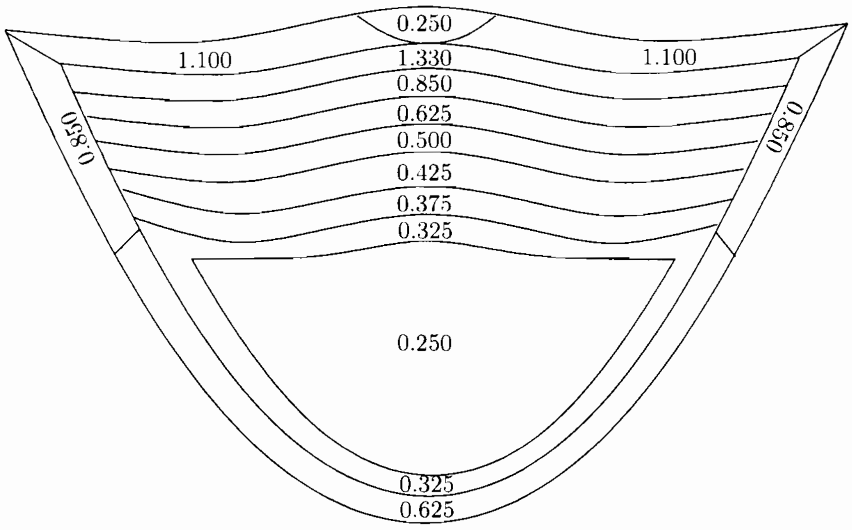

Figure 2.10: Thickness contour map of human aortic valve leaflets in mm [16]. The leaflets are the thinnest in the belly, their load-bearing part. They become thicker towards the line of attachment and the leaflet free edge. The thickest part is the nodule of Arrantius just below the centre of the free edge.

ventricle during diastole, the valve maximizes the energy output of the heart [141] and enables the Windkessel function of the ascending aorta, damping the pulsatility of blood flow [49, 104]. This is achieved by the leaflets going from their open separated position in systole to a closed, coapting configuration during diastole.

Opening and closing of the valve is a passive process [145, 141, 148], and governed by the pulsatile blood flow from the left ventricle which in turn is a function of blood pressure, or the gradient thereof across the valve. The blood pressure in the left ventricle and the aorta during one normal cardiac cycle as a function of time is represented by Figure 2.11. During diastole, the longest part of the cycle when the aortic valve is closed, the pressure gradient across the valve is roughly 80 mmHg or 10.67 kPa. During blood ejection in the systolic part of the cycle, blood pressure rises in both the ventricle and aorta to about 120 mmHg or 16.00 kPa. The rise time from diastolic to systolic pressure is short, so that on a different scale the pressure-time function resembles a step function.

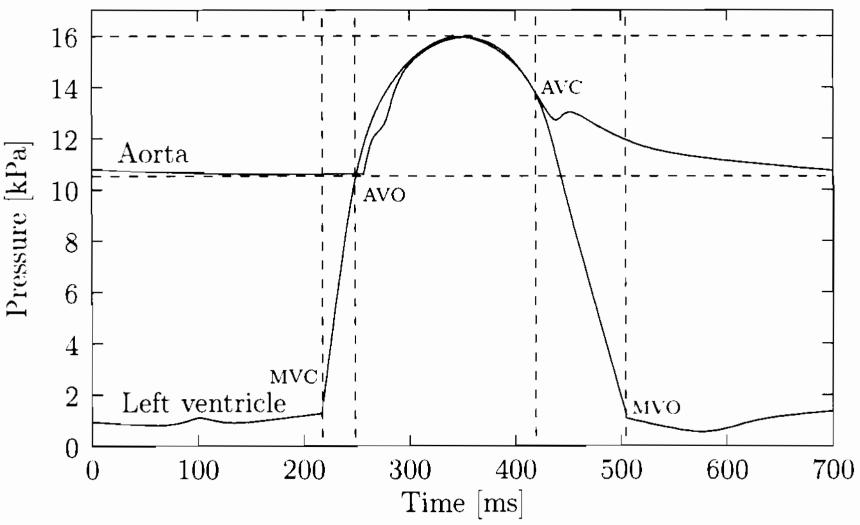

Figure 2.11: Pressure in the left ventricle and ascending aorta during one cardiac cycle. Vertical lines correspond to the times of mitral valve closure (MVC), aortic valve opening (AVO), aortic valve closure (AVC), and mitral valve opening (MVO) [98].

To increase the degree of complexity even further, the aortic valve leaflets do not operate in a rigid tube, but in a compliant structure [145, 37], where the presence of the sinuses of Valsalva allow the formation of vertices behind the open leaflets [3], and the aortic walls expand and contract as a passive reaction to varying blood pressure. Many of these features play a vital role for the exquisite longevity of the aortic valve, e.g. the compliant aortic root minimizes stresses in the leaflets during the cardiac cycle [115, 116] and the sinus vortices apart from adding rapid valve closure [163] perform a wash-out function preventing the build-up of thrombi behind the leaflets [39].

2.2 Mechanical Properties of Aortic Valve Tissue

2.2.1 Review of the Mechanical Behaviour of Aortic Valve Tissue

The problem of determination of the mechanical properties of aortic valve tissue has been tackled using various experimental techniques over the last 30 years. In vitro experiments include bulge tests [161, 103, 89], where a circular tissue specimens is clamped within a tube and one side pressurized. measurements on whole pressurized aortic roots [91, 150], and uniaxial [30, 29, 140, 157, 144, 127, 117, 143, 151, 95, 38, 110, 149, 14] and biaxial [97, 22, 24, 25, 26, 5, 121, 106] tension tests. In vivo the tissue response to physiological pressures was examined invasively using radiographic techniques [144, 143] and non-invasively utilizing ultrasound measurements [77]. Every technique has its specific limitation. Bulge tests and in vivo measurements borrow results from linear mechanics to arrive at results but emulate physiological conditions well. Uniaxial and biaxial tension tests on the other hand do not necessarily draw a physiologically accurate picture but also do not rely on assumptions as limiting as those of their counterparts.

Apart from different experimental setups, various species and/or preservation treatments have been subject to investigation. Those include fresh and cryopreserved human aortic valve tissue, explanted allografts, fresh and preserved (formaldehyde, glutaraldehyde, antibiotics) porcine tissue, and fresh canine tissue. The focus of most of these studies was on the heart valve leaflets and comparatively little data is available on the properties of the walls of the sinuses of Valsalva.

In spite of the broad spectrum of techniques and specimens all experiments confirm some or all aspects of the qualitative behaviour inherent in not only heart valves, but many soft tissues [52]:

- (almost) full elastic recovery up to very large strains,
- an exponential-type stress-strain relation characterized by an initial compliant phase followed – after a transition phase – by rapid stiffening,

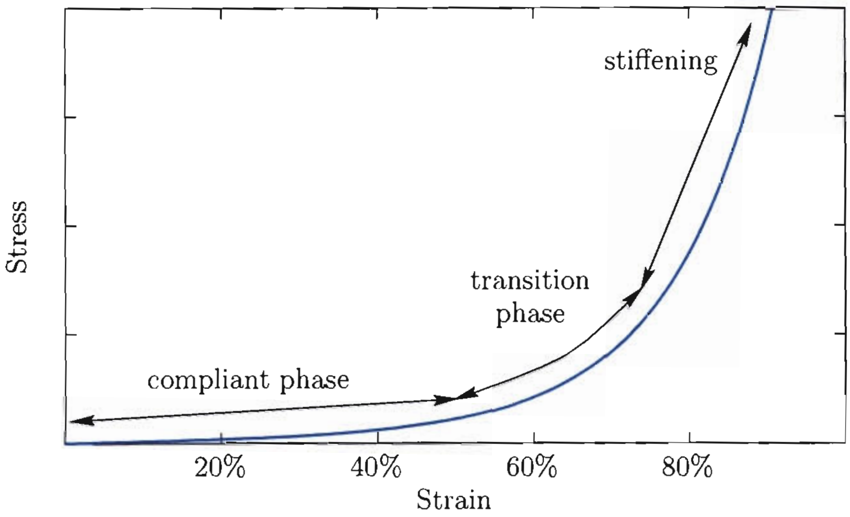

Figure 2.12: The typical stress response to straining of soft tissues. An initial compliant phase precedes a transition to a rapid stiffening.

- hysteresis, i.e. the loading and unloading path form a loop,
- pre-conditioning, i.e. reproducible results in cyclic loading and unloading of any experiment are only obtained after a couple of cycles,
- the stress-strain characteristics are strain rate dependent,
- tissue samples show stress relaxation when held at constant strain after stretching, or creep when subjected to constant stress,
- at least for the aortic valve leaflets, very pronounced anisotropy.

Although not explicitly investigated in the experiments mentioned, aortic valve tissue is commonly assumed to be (almost) incompressible, similar to tissue of the arterial wall [15, 28]. In addition to the above properties the aortic leaflets show very pronounced anisotropy leading to a much stiffer reaction in the circumferential leaflet direction.

The prominent shape of soft tissue stress-strain behaviour is qualitatively shown in Figure 2.12. The strains given in this figure are only examples. The actual values, e.g. the location and spread of the transition zone, depend very much on the

Figure 2.13: Porcine aortic valve leaflet clearly showing macroscopic collagen fibre architecture. Figure from [125].

origin of the tissue. The softer the tissue the more the curve is shifted to the right. Similarly, the dependence on strain rate of a specific specimen results in a slight shift of the curve for varying strain rates.

2.2.2 Tissue composition of Aortic Valve Tissue

The prominent exponentially shaped stress-strain response of aortic valve tissue is a result of the microscopic constitution of the material. As the valve consists of the aortic root and the valve leaflets, there are two distinct tissue types.

The aortic root is continuous with the ascending aorta, and macroscopically, apart from thickness and shape, the sinuses of Valsalva seem to be similar to aortic wall tissue, appearing macroscopically homogeneous. Indeed, the sinus walls consist of circumferentially oriented smooth muscle cells in a matrix of randomly oriented elastic and few small collagen fibres, suggesting no or little anisotropy [126, 125].

In contrast, even macroscopically, the valve leaflets can be seen to assemble a fibre-reinforced composite material. Thick collagen fibres can be seen to largely run in a circumferential direction, e.g. in Figure 2.14 and more clearly in Figure 2.13.

A more thorough investigation reveals that the leaflets are a layered structure, consisting mainly of collagen, elastin and glycosaminoglycans. Between the endothelial layer on both the aortic and ventricular sides of the leaflets (a mono-cell lining of endothelial cells, that can be found on all surfaces interfacing with blood flow), three distinct layers can be identified. On the aortic side of the leaflet, there is a layer consisting of dense collagen fibres embedded in an elastin matrix largely aligned with the circumferential direction, the fibrosa. The ventricularis, as the name suggests located on the ventricular side of the leaflet, is a layer similar in constitution to the fibrosa but with collagen fibres more randomly distributed [122]. And finally these two layers are separated by a loose, gelatinous spongiosa [65, 31].

Given the complex composition of leaflets of layers that in turn are complex composite structures, and moreover are connected preloaded, i.e. a compressed fibrosa attached to a stretched ventricularis [155, 153, 154], their highly non-linear and anisotropic stress-strain behaviour is not surprising. As the cells in the valve cusps do not significantly contribute to mechanical stresses [94], the mechanical behaviour is a function of this complex structure. Collagen gives the leaflets the strength for their load-bearing function during diastole. Collagen is however relatively inflexible (only about 1% to 2% strain to failure [78]), and the comparatively high extensibility of the leaflets can only be a consequence of their crimped and wavy occurrence. The compliant phase of the model stress-strain curve in Figure 2.12 is thus associated with uncrimping and unfolding of collagen fibres. As more and more fibres become straight, they take up an increasing portion of the load in the transition phase. Finally, when most of the collagen fibres are uncrimped they dominate the mechanical behaviour and cause a lock-up in the stiffening phase. Although half of the dry weight of leaflets is collagen and only 13% elastin [1], the latter seem to play a vital role in leaflet elastic recoil. The collagen fibres are embedded in a spongelike elastin matrix that, because of its elasticity, allows for reconfiguration of the fibres and acts as a return spring to retract the fibres to their crimped state upon unloading [130, 147, 87].

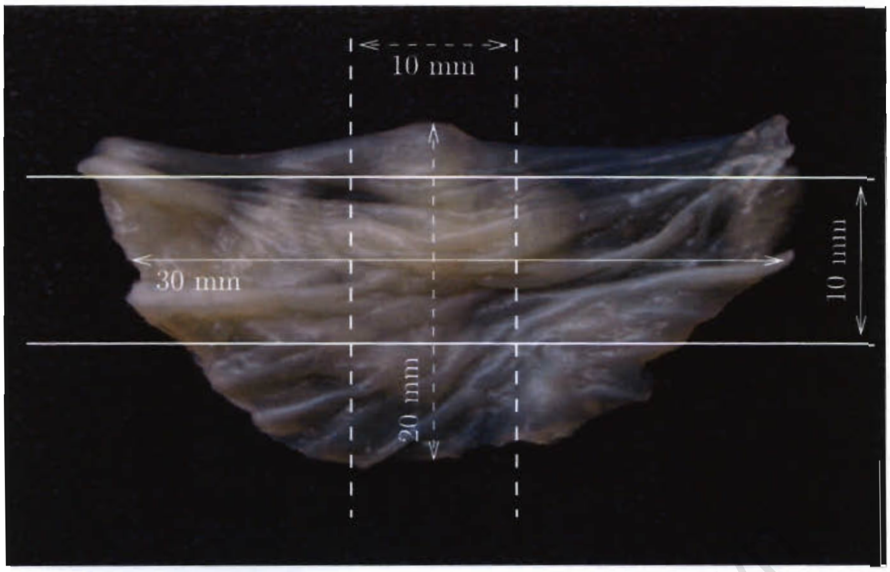

Figure 2.14: Approximate dimensions of the strips cut from porcine aortic valve leaflets in circumferential (solid line) and radial (dashed line) directions.

2.2.3 Experimental Setup for Uniaxial Tension Tests of Porcine Aortic Valve Tissue

To obtain input data for the constitutive models used later on, uniaxial tension tests have been performed on fresh porcine aortic valve tissue. To this end, fresh porcine hearts were harvested immediately after killing of the animals at a local abattoir and shipped to the laboratory on ice, stored in Hanks balanced salt solution (HBSS, Sigma, Germany) containing a Penicillin/Streptomycin solution (Pen/Strep. 100U/ml/10mg/ml, Sigma, Germany) and Amphotericin B (25μg/ml, Sigma, Germany). The aortic valves were exposed and the leaflets as well as strips of ascending aorta and sinus tissue were removed gently, rinsed in sterile phosphate-buffered salt solution (PBS), and subsequently stored in MCDB (Sigma, Germany) containing Pen/Strep.(100U/ml/10mg/ml) and Amphotericin B (25μg/ml) at 4°C for not longer than two hours before they were tested.

Approximate dimensions for the aortic strips in both directions as well as the leaflets in circumferential direction were 30mm in length and 10mm in width, for the leaflets in radial direction only 20mm in length and a width of 10mm as shown in Figure 2.14. The strips were mounted in customized clamps that allow this preparation off the test rig, holding the clamps apart a gauge length of 15mm for the aortic specimens and 10mm for the leaflets. The width and thickness of each clamped specimen was measured at three different locations and the mean value was used for stress calculations. In most cases the tissue buckled as a result of clamping and the length of zero extension had to be adjusted in the test rig accordingly. This was done until no buckling could be seen in the strips.

The tests were carried out using an Instron® 5544 H1821 test rig equipped with a 500N load cell and customized to fit the clamps designed for soft tissue specimens that are mounted in a temperature controlled fluid bath (see Figure 2.15). Phosphate-buffered salt solution (PBS) at pH 7.4 and a temperature of 37°C has been used for all experiments. After mounting of the clamps, the tissue strips have been tested with the following protocol. The first consisted of six loading and unloading cycles up to an engineering strain of 50% for all samples except leaflets in circumferential direction which have been tested only up to 10% engineering strain. This was followed by a stress relaxation test where the tissue strips have been held at the same respective values of maximal strain for 3 minutes. A last loading cycle until failure concluded the test sequence. Apart from an experiment to establish strain rate sensitivity all tests of circumferential leaflets have been done at a strain rate of 0.25%/s, the tests of the remaining strips at a strain rate of 2.5%/s.

2.2.4 Results

The results of a typical tensile test with cyclic loading and unloading are shown in Figure 2.16 for a circumferential leaflet strip and in Figure 2.17 for a leaflet sample in radial direction. Hysteresis, i.e. different paths for loading and unloading, can clearly be seen. In both cases the first cycle produces higher stresses, and pre-conditioning has the effect of shifting the curves to the right with the first few cycles until, after a couple of cycles, a stable, repeatable path is achieved. In most cases six cycles were sufficient for pre-conditioning. otherwise the first cycling protocol was repeated.

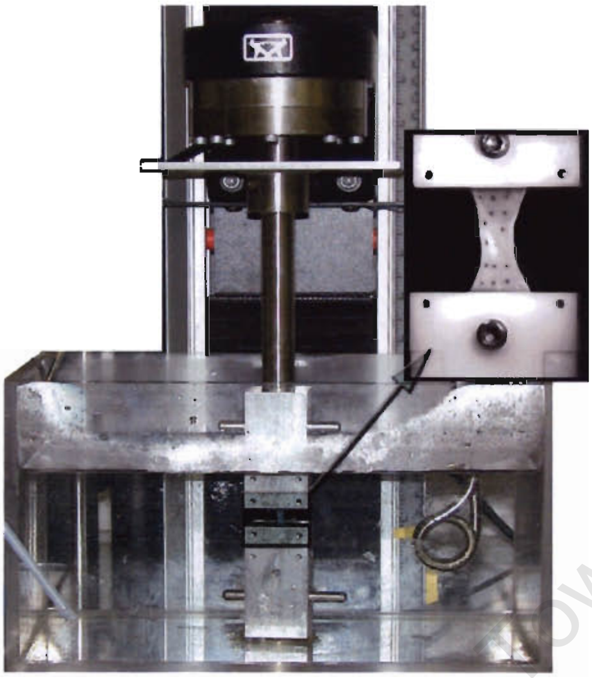

Figure 2.15: Clamped test specimen in PBS at 37°C.

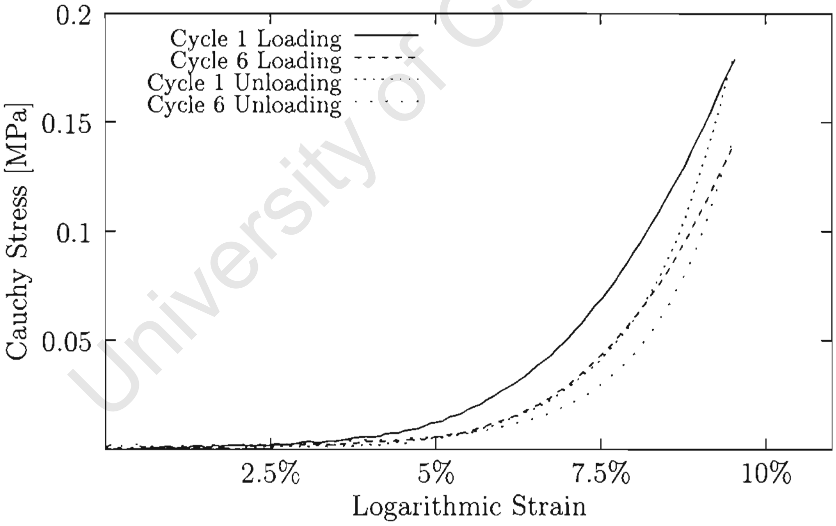

Figure 2.16: Uniaxial stress-strain curves of porcine aortic leaflet specimens in circumferential direction in loading and unloading for different cycles.

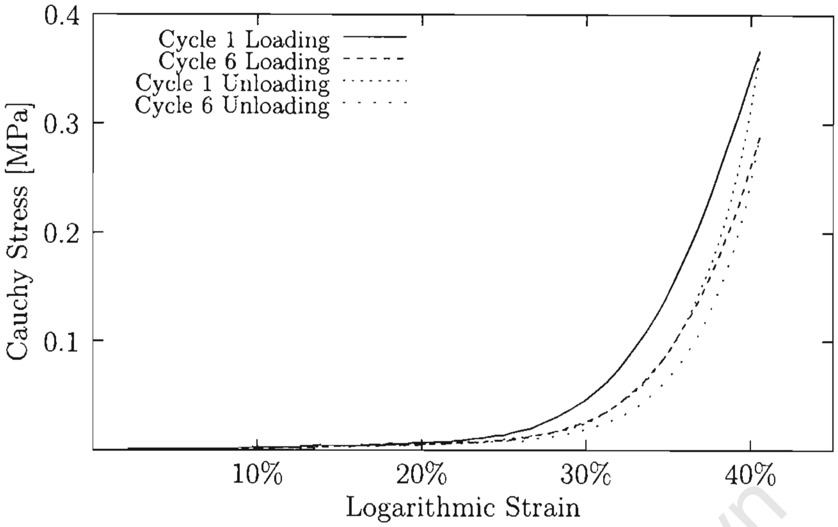

Figure 2.17: Uniaxial stress-strain curves of porcine aortic leaflet specimens in radial direction in loading and unloading for different cycles.

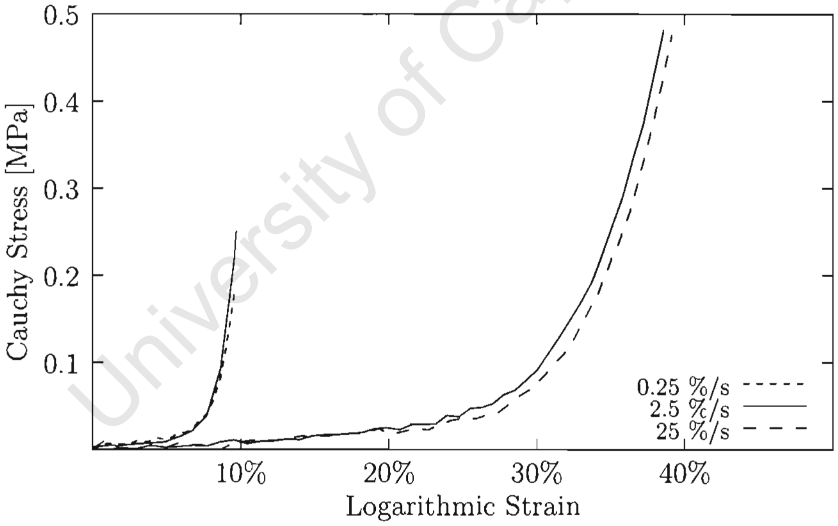

Figure 2.18: Uniaxial stress-strain curves of porcine aortic leaflet specimens in both radial and circumferential directions at various strain rates.

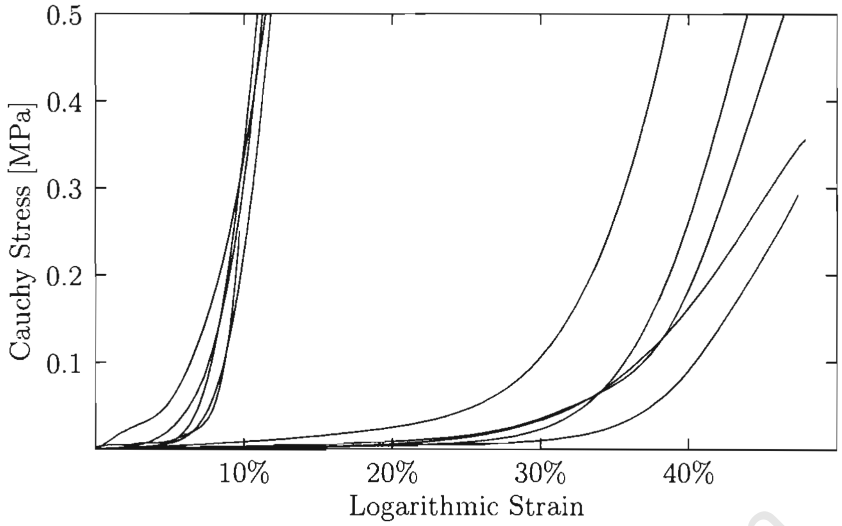

Figure 2.19: Uniaxial stress-strain curves of different porcine aortic leaflet specimens in both radial and circumferential directions.

Only a relatively small effect of varying strain rate on the results can be seen in Figure 2.18, where the results of the same leaflet sample are shown at a strain rate of 0.25%/s and 2.5%/s for the circumferential strip and 2.5%/s and 25%/s for the radial direction, justifying – for the sake of experimental convenience – the use of different strain rates for circumferential and radial leaflet specimens.

Stress-strain plots of five leaflets in each direction are plotted in Figure 2.19. The curves for circumferential strips lie comparatively close together, the radial curves scatter more. The pronounced anisotropy of leaflets, e.g. the much stiffer response in the circumferential direction, can clearly be seen.

Plots of stress-strain curves of one sinus wall sample and four samples of the ascending aorta each in a circumferential and axial direction are shown in Figure 2.20. The response for all these specimens is much more compliant as compared to aortic leaflets. Furthermore, results of circumferential and axial specimens are scattered evenly and hence a clear decision on anisotropy cannot be made from these plots.

The results of the relaxation tests are shown in Figure 2.21 and Figure 2.22.

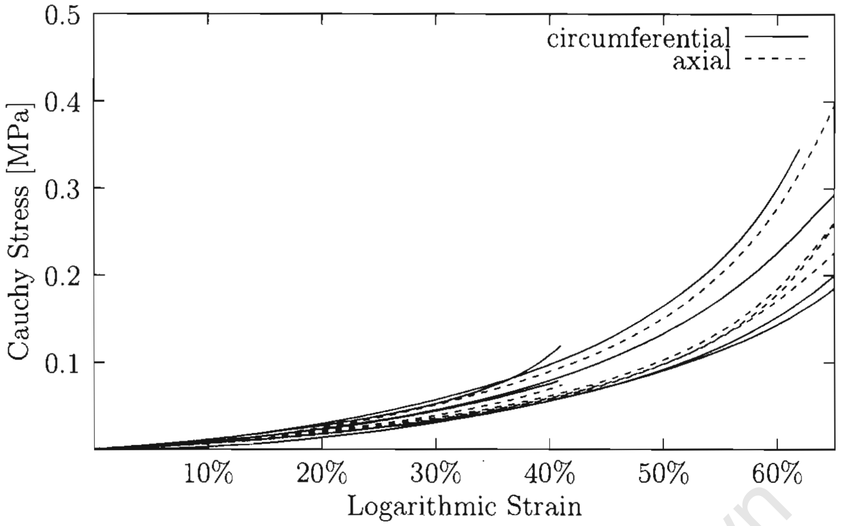

Figure 2.20: Uniaxial stress-strain curves of different porcine aortic sinus and ascending aorta specimens in both axial and circumferential directions.

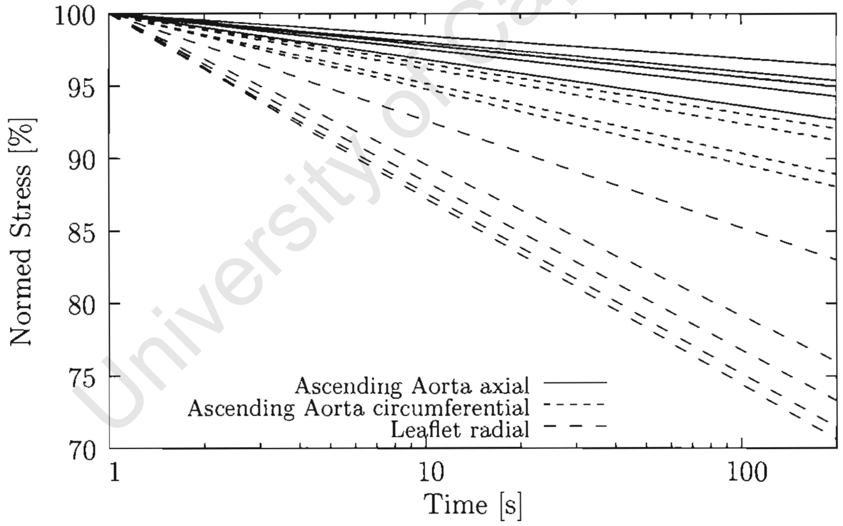

Figure 2.21: Linear fits to relaxation test data on logarithmic time scale of aortic and radial leaflet specimens. Stress is normed to peak stress.

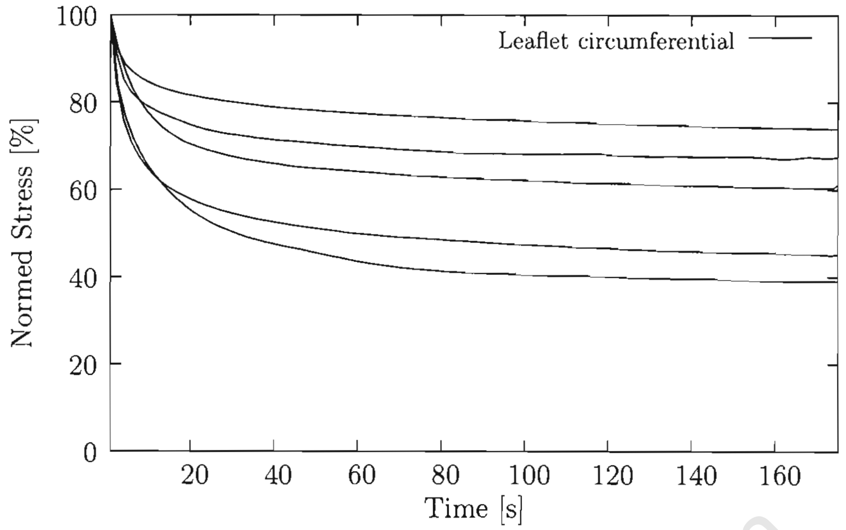

Figure 2.22: Stress relaxation test results of leaflet strips in circumferential direction on linear scales. Stress is normed to peak stress.

The former shows linear fits to the stresses normed to the peak values observed at the completion of stretching on a logarithmic time scale. The latter represents the normed stresses on a linear time scale for the circumferential leaflet strips. For these, the quality of the fits with an intercept of 100% on the stress fraction axis was not sufficient. The best fits are obtained for the aortic strips. Judging from the figures, it appears that relaxation plays an increasing prominent role from the axial aortic to the circumferential leaflet strips via the circumferential aortic and radial leaflet specimens in that order. Additionally, the relaxation tests indicate some anisotropy in the samples of the aortic walls.

2.2.5 Discussion

The results of the uniaxial tension tests of porcine aortic valve tissue presented in the previous section largely confirm what is reported in the literature. The main features are the exponential shape of the stress-strain curves, the pronounced anisotropy in the leaflets and the increasingly stiff response from the aortic wall to the radial and then the circumferential leaflets. The greatest discrepancy was found in the results of varying strain rate. There is hardly a difference in results in Figure 2.18 despite a strain rate increase of a factor 10 with a maximum of 25 %/s. A slight variation with strain rate was found in another study, where a tenfold increase in strain rate up to a strain rate of 800 %/s roughly doubled stress [127]. However, a different group reported a significant difference with an increase in strain rate from 28 %/s to 233 %/s, i.e. a very clear shift of the stress-strain curve to the left [95]. Unfortunately, although the heads of the test rig used are capable of higher speeds, inertia of the clamps at the turning points seem to affect results at these higher strain rates. Results of strain rates of a few 100 %/s could therefore not be obtained. The two studies mentioned tested at room temperature keeping the tissue moist manually, which might affect results in that way.

The stress relaxation tests in Figure 2.21 and Figure 2.22 are in agreement with [127, 117], particularly that relaxation plays an increasing role from the aortic walls to the radial and circumferential leaflet strips. Absolute values of relaxed stress fraction, especially in the circumferential specimens, tend to be higher in other studies [127, 117, 151]. Stress relaxation is reported to be very strain rate dependent [149], which might be a reason for that.

The stress-strain curves for aortic and sinus wall tissue in Figure 2.20 are in good agreement with published data [127, 117, 106]. Anisotropy does not play as important a role in sinus and ascending aorta tissue as it does in the valve leaflets. Here, the only indication of anisotropy is in the relaxation results of the wall strips. In the stress-strain curves, anisotropy would establish itself only for higher strains in the post-transition phase [157]. Results from biaxial tests are more clear on the issue of anisotropy, since both directions can be tested on the same specimen. These results suggest that there is some anisotropy also in the pre-transition phase [106], but not nearly to the extent as it is present in the valve leaflets.

The dramatically stiffer stress response of circumferential over radial leaflet strips clearly stands out in Figure 2.19. Although results from other researchers agree well in order of magnitude of both stresses and strains with the values in that figure (taking into account the different stress and strain measures used), this drastic degree of anisotropy does not always manifest itself as clearly. Apart from differences in experimental techniques like the presence of fluid baths with temperature control to keep tissue moist and warm, and uniaxial and planar biaxial test setups, the major reason for that discrepancy is probably the difficulty in defining the undeformed gauge length of radial leaflet specimens. One method for finding this length is to strain the specimen to the maximal strain or the maximal load desired and return to the point where the load returns to zero [127, 117, 95]. The 500 N load cell used for the tests here was unfortunately found to be not accurate enough to find a zero load. In fact, the force reading oscillated slightly around zero with a clamped undeformed radial specimen, and there seemed to be no difference in oscillation upon slight extension. It was therefore not possible to uniquely define a reference length by a zero load state. Instead, the crosshead distance was adjusted after mounting of the jaws until the clamped specimen neither buckled nor was stretched as determined visually. This method is not ideal as a shift in reference length causes a shift of the stress-strain curve, to the left for too much initial stretch or to the right for an initially buckled specimen. The resulting uncertainty probably explains the increased scatter of the radial curves in Figure 2.19 as compared to their circumferential counterparts. (This phenomenon can also be seen in [140, 97, 38].) The curves are however still close enough together to demonstrate reproducibility. Viewing the results in Figure 2.19 in the light of other published data, makes them seem to lie in the middle. Data from circumferential strips more often is in agreement [127, 117, 97, 22, 95, 110, 26, 5, 121] than not [140, 151, 38]. In the latter case the reported results are more compliant. The increased scatter in radial data is reflected in literature, with some reporting stiffer radial response [127, 117, 95] and others even more compliant response [140, 97, 22, 38, 26]. Some of the latter [97, 22, 26] are reports on planar biaxial tests where the undeformed state of the tissue can be established more reliably. Particularly good agreement in both directions can be found with the uniaxial study [110] and recent biaxial test series [5]. The uniaxial stress-strain results of porcine leaflet tissue can thus confidently be used as input data for the constitutive models used in the valve models presented in Chapter 4.

Chapter 3

Governing Equations and Finite Element Approximations

It is in the framework of continuum mechanics that the models of the aortic valve will be developed. A brief review of relevant theory will therefore be given in this chapter. More detailed accounts can be found in many textbooks on the subject, e.g. [83, 64, 107]. Having discussed the underlying theory, the chapter proceeds with an overview of constitutive models for aortic valve tissue. An outline of the finite element method used to discretize the differential equations concludes the chapter.

3.1 Theoretical Framework of Continuum Mechanics

3.1.1 Setting the Scene: Cauchy's Equations of Motion

The objective of stress analysis is to find the reaction of one or more (interacting) bodies to a given load, a set of prescribed conditions or a mix thereof. This can be achieved within the framework of continuum mechanics, where bodies are assumed to be formed of a continuum, irrespective of their molecular constituents. A body in this context can be thought of as some region in Euclidean space $\mathbb{R}^3$, as shown in Figure 3.1. Continuum mechanics is a classical theory, so that bodies have to obey Newton's laws of motion, particularly

$$\mathbf{f}_{res} = \frac{D\mathbf{p}}{Dt}. \tag{3.1}$$

where $\frac{D}{Dt}$ denotes the material time derivative, $\mathbf{f}_{res}$ is the resultant force acting on the body and $\mathbf{p}$ its linear momentum. The resultant force is the sum of all forces acting on the body, e.g. gravity acting as a body force throughout its volume, surface tractions on the outer surface of the body. In a continuum the sum is replaced by an integral, so that

$$\mathbf{f}_{res} = \int\limits_{\partial B} \mathbf{t}\, dA + \int\limits_{B} \mathbf{b}\, dV. \tag{3.2}$$

where ∂B denotes the boundary surface and B the volume of the body. $\mathbf{b}$ is the body force per unit volume and $\mathbf{t}$ a surface traction, i.e. a force acting on an infinitesimal area element on the boundary of the body. Under Cauchy's stress principle the surface traction is proportional to the unit outward normal of the surface or surface element $\mathbf{n}$ and the Cauchy or true stress tensor $\boldsymbol{\sigma}$ can be defined as

$$\mathbf{t}\, dA = \boldsymbol{\sigma} \cdot \mathbf{n}\, dA. \tag{3.3}$$

Using the above definition, equation (3.1) now reads

$$\int\limits_{\partial B} \boldsymbol{\sigma} \cdot \mathbf{n}\, dA + \int\limits_{B} \mathbf{b}\, dV = \frac{D\mathbf{p}}{Dt}. \tag{3.4}$$

The linear momentum $\mathbf{p}$ in a continuum is the integral of the product of mass density ρ and velocity $\mathbf{v}$,

$$\mathbf{p} = \int\limits_{B} \rho\, \mathbf{v}\, dV. \tag{3.5}$$

Applying Reynold's transport theorem to the material time derivative of the previous equation, it follows that

$$\frac{D\mathbf{p}}{Dt} = \int\limits_{B} \left(\frac{D}{Dt}(\rho\, \mathbf{v}) + \operatorname{div}(\mathbf{v})\rho\, \mathbf{v} \right) dV = \int\limits_{B} \left[\rho \frac{D\mathbf{v}}{Dt} + \mathbf{v} \left(\frac{D\rho}{Dt} + \rho \operatorname{div} \mathbf{v} \right) \right] dV. \tag{3.6}$$

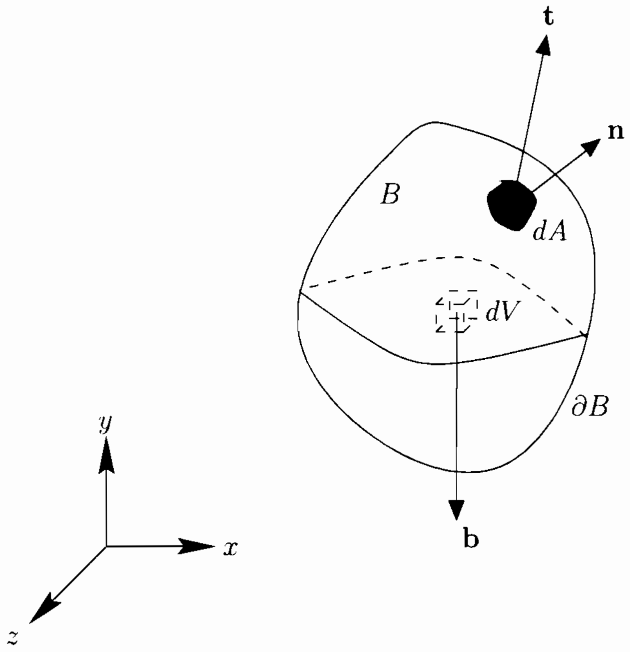

Figure 3.1: Body force per unit volume **b** act on body B, surface traction **t** on the boundary $\partial\mathbf{B}$ of B. Traction is proportional to unit outward normal **n**.

where the second equality follows after application of the product rule and rearrangement of terms. Since conservation of mass m dictates, that

$$\frac{Dm}{Dt} = 0 = \frac{D}{Dt}\int_B \rho\, dV = \int_B \left(\frac{D\rho}{Dt} + \rho\,\mathrm{div}\,\mathbf{v}\right) dV, \tag{3.7}$$

where again Reynold's transport theorem has been applied. Since the integration is over arbitrary volumes, the integrand of the last integral has to vanish, i.e.

$$\frac{D\rho}{Dt} + \rho\,\mathrm{div}\,\mathbf{v} = 0, \tag{3.8}$$

and using this result in equation (3.6) and substituting in equation (3.4), it follows that

$$\int_{\partial B} \boldsymbol{\sigma}\cdot\mathbf{n}\, dA + \int_B \mathbf{b}\, dV = \int_B \rho\,\frac{D\mathbf{v}}{Dt}\, dV. \tag{3.9}$$

Applying Gauss's theorem to the first integral in the equation above and again realizing that integration is over arbitrary volumes, it finally follows that

$$\operatorname{div} \boldsymbol{\sigma} + \mathbf{b} = \rho \frac{D\mathbf{v}}{Dt}, \tag{3.10}$$

which is Cauchy's equation of motion.

In a static problem the time derivative of momentum vanishes and the acceleration terms in Cauchy's equations equation (3.10) vanish, so that equilibrium is governed by

$$\operatorname{div} \boldsymbol{\sigma} + \mathbf{b} = \mathbf{0}. \tag{3.11}$$

Rotational equilibrium is achieved, if the total moment acting on the body vanishes. Integration over all moments about the origin thus yields

$$\frac{D}{Dt} \int\limits_{B} \mathbf{r} \times \rho \mathbf{v} \, dV = \int\limits_{\partial B} (\mathbf{r} \times \mathbf{t}) \, dA + \int\limits_{B} (\mathbf{r} \times \mathbf{b}) \, dV, \tag{3.12}$$

where $\mathbf{r}$ is the position vector from the origin. Using Gauss's theorem it can be shown, that rotational equilibrium requires, that the stress tensor $\boldsymbol{\sigma}$ is symmetric,

$$\boldsymbol{\sigma} = \boldsymbol{\sigma}^{T}. \tag{3.13}$$

The forces acting on a body cause some form of deformation, so that a kinematic description is necessary to find a solution to equation (3.11).

3.1.2 Deformation of a Continuum

Any body subject to stationary external forces will respond in such a way to satisfy equation (3.11). This response is a combination of translational motion, rotation and deformation. In what follows the discussion will be restricted to elastic deformation, i.e. the body in question will return to its original shape once the deforming forces vanish.

In a physical body, deformation is the result of the change of distances between individual particles that form the body. In principle it would be possible to assign a number to each particle and track the motion and hence the deformation would be known. Considering the number of particles that make up a body, this approach is attached to some logistical problems, one of the arguments for the continuum approach.

Within the framework of continuum mechanics, as discussed earlier, a body is thought of the subspace of $\mathbb{R}^3$ it occupies. Since $\mathbb{R}^3$ is complete, i.e. in each neighbourhood of a point $\mathbf{x} \in \mathbb{R}^3$ there are infinitely many other points in $\mathbb{R}^3$, every such subspace is uncountably infinite and therefore a numbering of particles is not possible. However, a material point in a continuum (i.e. a point in $\mathbb{R}^3$) can be identified by the location it was occupying at some reference time t_0. This so-called Lagrangian description of a continuum is particularly useful for the analysis of structures.

The spatial aspect of a continuous body is therefore characterized by the reference location $\mathbf{X} \in \mathbb{R}^3$ of all its material points. The deformation of a continuous body is completely defined if the relation between the current location of a material point $\mathbf{x} \in \mathbb{R}^3$ and the reference location $\mathbf{X}$ is known at all times t, i.e.

$$\mathbf{x}(t) = \mathbf{x}(\mathbf{X}, t) \qquad \text{with } \mathbf{x}(t_0) = \mathbf{X}. \tag{3.14}$$

Of particular interest in the solution of equation (3.11) is the local deformation, i.e. the change $d\mathbf{x}$ of the neighbourhood $d\mathbf{X}$ of $\mathbf{X}$. This change is given by the deformation gradient $\mathbf{F}$, such that

$$d\mathbf{x} = \mathbf{F} \cdot d\mathbf{X}. \tag{3.15}$$

The deformation gradient $\mathbf{F}$ is a second order tensor defined by

$$\mathbf{F} = \frac{\partial \mathbf{x}}{\partial \mathbf{X}}. \tag{3.16}$$

Thus, $\mathbf{F}$ maps $d\mathbf{X}$ of the reference configuration onto $d\mathbf{x}$ of the current configuration which is shown in Figure 3.2.

$d\mathbf{x}$ will be a shortened or lengthened, and rotated $d\mathbf{X}$. This is the essence of the polar decomposition theorem: The deformation gradient $\mathbf{F}$ can be decomposed into a rotation followed by stretching or vice versa. i.e.

$$\mathbf{F} = \mathbf{R} \cdot \mathbf{U} = \mathbf{V} \cdot \mathbf{R}, \tag{3.17}$$

where $\mathbf{R}$ is an orthogonal second order tensor describing the rotation and $\mathbf{U}$ and $\mathbf{V}$ are the right and left stretch tensors respectively.

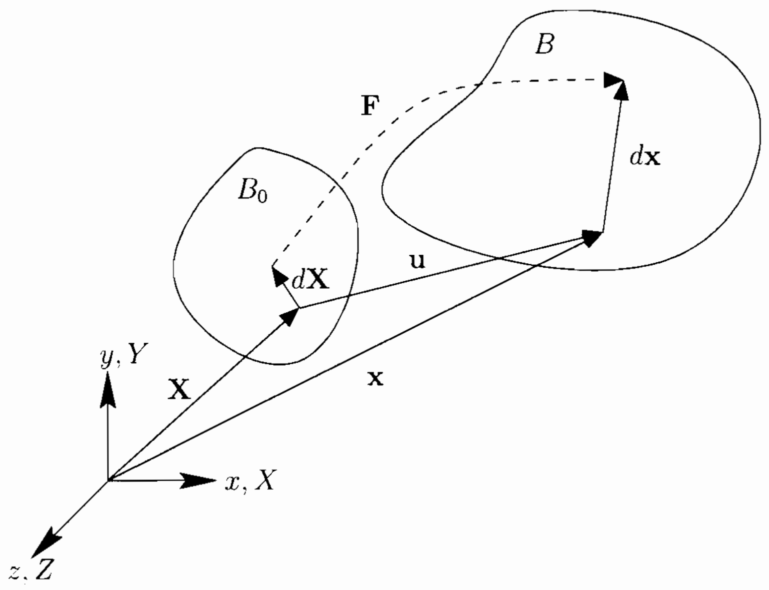

Figure 3.2: An infinitesimal line element $d\mathbf{X}$ of a body's reference configuration B_0 transforms into a lengthened and rotated line element $d\mathbf{x}$ of the current configuration B under the action of the deformation gradient $\mathbf{F}$. $\mathbf{X}$ is a position vector of the reference configuration undergoing a displacement $\mathbf{u}$ resulting in the new position vector $\mathbf{x}$ of the same point in the current configuration.

Both $\mathbf{U}$ and $\mathbf{V}$ are symmetric tensors so that there exist three mutually perpendicular directions in which eigenvectors of $\mathbf{U}$ or $\mathbf{V}$ lie. The eigenvectors of $\mathbf{V}$ differ from the eigenvectors of $\mathbf{U}$ only by the rigid body rotation $\mathbf{R}$. The corresponding eigenvalues however are the same for both. They are the principal stretches λ_i, with stretch defined as the ratio of current length dL of $d\mathbf{x}$ to original length dL_0 of $d\mathbf{X}$:

$$\lambda = \frac{dL}{dL_0}. \tag{3.18}$$

Computationally interesting are the right and left Cauchy-Green deformation tensors since they can be directly calculated from the deformation gradient. The right Cauchy-Green tensor is defined as

$$\mathbf{C} = \mathbf{U}^2, \tag{3.19}$$

and can be computed via

$$\mathbf{C} = \mathbf{F}^T \cdot \mathbf{F}, \tag{3.20}$$

whereas the left Cauchy-Green deformation tensor is defined as

$$\mathbf{B} = \mathbf{V}^2, \tag{3.21}$$

that is calculated according to

$$\mathbf{B} = \mathbf{F} \cdot \mathbf{F}^T. \tag{3.22}$$

It follows that the eigenvalues of these tensors are λ_i^2, the squares of the principal stretches, which equally describe the deformation of the body in question.

3.1.3 Strain as a Measure of Deformation

Instead of measuring the *amount* of deformation in terms of stretches as in the previous section, it is common practice to use one of various forms of strain for that purpose. In contrast to stretch which is $\lambda = 1$ (in the one–dimensional case) if no deformation occurs, strain is a function of stretch that vanishes in that case, i.e. strain $\epsilon = 0$ for no deformation.

There are several strain measures, such as nominal strain

$$\epsilon_n = \lambda - 1, \tag{3.23}$$

which is often used experimentally, logarithmic or true strain

$$\epsilon_t = \int_0^\lambda \frac{d\lambda'}{\lambda'} = \ln \lambda, \tag{3.24}$$

or Green's strain

$$\epsilon_G = \frac{1}{2}(\lambda^2 - 1), \tag{3.25}$$

to name but a few.

All strain measures are approximately equal in the small strain limit but differ substantially with increasing strain. It is therefore important to specify strain measures in finite strain analyses.

The generalization of the definition of strain to three dimensions utilizes the left and right stretch tensors, since their eigenvalues are powers of the principal stretches λ_i as discussed in the previous section. Relevant to the work discussed here are the logarithmic strain tensor

$$\boldsymbol{\epsilon} = \ln \mathbf{V}, \tag{3.26}$$

and the Green strain tensor

$$\mathbf{E} = \frac{1}{2}(\mathbf{U}^2 - \mathbf{I}) = \frac{1}{2}(\mathbf{C} - \mathbf{I}), \tag{3.27}$$

where equation (3.19) has been used.

3.1.4 Stress Measures Conjugate in Power

Evoking conservation of energy, the rate of work generated by body forces and surface traction on B is

$$\frac{D}{Dt}\int\limits_B \left(\rho U + \frac{1}{2}\rho\, \mathbf{v}\cdot\mathbf{v}\right) dV = \int\limits_B \mathbf{v}\cdot\mathbf{b}\, dV + \int\limits_{\partial B} \mathbf{v}\cdot\mathbf{t}\, dA, \tag{3.28}$$

where U is the internal energy per unit volume, and $\mathbf{v}$ the velocity field. Using Reynold's theorem on the left integral of the above equation leads to

$$\int\limits_B \left(\rho\frac{DU}{Dt} + \frac{1}{2}\rho\frac{D(\mathbf{v}\cdot\mathbf{v})}{Dt}\right) dV = \int\limits_B \left(\rho\frac{DU}{Dt} + \rho\,\mathbf{v}\cdot\frac{D\mathbf{v}}{Dt}\right) dV. \tag{3.29}$$

Using the definition of the Cauchy stress tensor equation (3.3) together with Gauss's theorem, the last integral in equation (3.28) can be written as

$$\int\limits_{\partial B} \mathbf{v}\cdot\mathbf{t}\, dA = \int\limits_{\partial B} \mathbf{v}\cdot(\boldsymbol{\sigma}\cdot\mathbf{n})\, dA = \int\limits_B \left(\mathbf{v}\cdot \operatorname{div}\boldsymbol{\sigma} + \boldsymbol{\sigma} : (\frac{\partial\mathbf{v}}{\partial\mathbf{x}})\right) dV. \tag{3.30}$$

Substituting equation (3.29) and equation (3.30) in equation (3.28) and rearranging terms, gives

$$\int\limits_B \left(\rho\frac{DU}{Dt} - \boldsymbol{\sigma} : (\frac{\partial\mathbf{v}}{\partial\mathbf{x}}) + \mathbf{v}\cdot\left(\rho\frac{D\mathbf{v}}{Dt} - \operatorname{div}\boldsymbol{\sigma} - \mathbf{b}\right)\right) dV = 0. \tag{3.31}$$

The last term in the integral above vanishes because of Cauchy's equation of motion in equation (3.10), and we obtain

$$\int\limits_B \rho \frac{DU}{Dt}\, dV = \int\limits_B \boldsymbol{\sigma} : (\frac{\partial \mathbf{v}}{\partial \mathbf{x}})\, dV. \tag{3.32}$$

Splitting the velocity gradient into symmetric and antisymmetric parts

$$\mathbf{L} = \frac{\partial \mathbf{v}}{\partial \mathbf{x}} = \mathrm{sym}(\mathbf{L}) + \mathrm{skew}(\mathbf{L}) = \mathbf{D} + \mathbf{W}, \tag{3.33}$$

we finally arrive at

$$\rho \frac{DU}{Dt} = \boldsymbol{\sigma} : \mathbf{D}, \tag{3.34}$$

since the contraction of a symmetric with an antisymmetric tensor vanishes.

Thus, the contraction of the Cauchy stress tensor with the rate of deformation tensor $\mathbf{D}$ gives the rate of internal work and the pair is conjugate in work rate or power.

In the above derivation, all quantities have been defined and evaluated in the current configuration. This description is however not always convenient and the original configuration is rather used. The rate of work per undeformed volume is then

$$\rho_0 \frac{dU_0}{dt} = J\rho \frac{DU}{Dt}, \tag{3.35}$$

since conservation of mass states $\rho_0 = J\rho$. It then follows from equation (3.34) that

$$\begin{aligned} J\mathbf{D} : \boldsymbol{\sigma} &= J\mathbf{L} : \boldsymbol{\sigma} = J(\dot{\mathbf{F}} \cdot \mathbf{F}^{-1}) : \boldsymbol{\sigma} = J\dot{\mathbf{F}} : (\boldsymbol{\sigma} \cdot \mathbf{F}^{-T}) \\ &= J(\mathbf{F}^{-T} \cdot \mathbf{F}^{T} \cdot \dot{\mathbf{F}}) : (\boldsymbol{\sigma} \cdot \mathbf{F}^{-T}) = J(\mathbf{F}^{T} \cdot \dot{\mathbf{F}}) : (\mathbf{F}^{-1} \cdot \boldsymbol{\sigma} \cdot \mathbf{F}^{-T}), \end{aligned} \tag{3.36}$$

where $(\mathbf{A} \cdot \mathbf{B}) : \mathbf{C} = \mathbf{B} : (\mathbf{A}^T \cdot \mathbf{C}) = \mathbf{A} : (\mathbf{C} \cdot \mathbf{B}^T)$, the symmetry of $\boldsymbol{\sigma}$ and $\dot{\mathbf{F}} = \mathbf{LF}$ have been used.

Defining the second Piola-Kirchhoff stress $\mathbf{S}$ as a measure of stress in the original configuration as

$$\mathbf{S} \cdot \mathbf{n}_0\, dA_0 = \mathbf{F}^{-1} \cdot \mathbf{t}_0\, dA_0, \tag{3.37}$$

it can be shown that this stress and Cauchy stress transform as

$$\boldsymbol{\sigma} = J^{-1}\mathbf{F} \cdot \mathbf{S} \cdot \mathbf{F}^T \tag{3.38}$$

$$\mathbf{S} = J\,\mathbf{F}^{-1} \cdot \boldsymbol{\sigma} \cdot \mathbf{F}^{-T}. \tag{3.39}$$

With the time derivative of the Green strain tensor $\dot{\mathbf{E}} = \mathrm{sym}(\mathbf{F}^T \cdot \dot{\mathbf{F}})$ and the symmetry of the second Piola-Kirchhoff stress tensor equation (3.36) reads

$$\rho_0 \frac{dU_0}{dt} = \mathbf{S} : \dot{\mathbf{E}}, \tag{3.40}$$

hence the rate of Green strain and second Piola-Kirchhoff stress is another pair conjugate in power.

The conjugate pairs discussed above are not all possible combinations; on the contrary, as there are many possibilities to define strain measures there are as many conjugate stress measures. The pairs discussed above are sufficient for the work discussed here.

3.1.5 Characterizing Mechanical Behaviour of Materials: Constitutive Equations

The formulations presented in the previous sections are applicable to all materials as long as the continuum approach is justified. The internal stresses in equilibrium equation (3.11) are a result of the material history and in general depend on loading and deformation history, temperature, etc. The constitutive equations of a material express the link of the stresses in the material to its history, in particular to its state of deformation.

We restrict the discussion here to Cauchy elastic materials, for which the principles of material objectivity and local action hold. In this case the state of stress does not depend on the path of deformation (whereas the work done in general does) and the Cauchy stress tensor can be determined from a response function of the deformation gradient,

$$\boldsymbol{\sigma} = f(\mathbf{F}). \tag{3.41}$$

Material objectivity imposes restrictions on this response function, in that the dependence on the rotation $\mathbf{R}$ can only take the form

$$\boldsymbol{\sigma} = \mathbf{R} \cdot f(\mathbf{U}) \cdot \mathbf{R}^T. \tag{3.42}$$

The finite element approximations discussed later in Section 3.3 require the rate of Cauchy stress to be calculated from the constitutive equations. The constitutive models considered here belong to a class that can be described using a hypoelastic material law that relates the rate of Cauchy stress to the rate of deformation according to

$$\dot{\boldsymbol{\sigma}} = \mathfrak{C} : \mathbf{D}. \tag{3.43}$$

The rate of deformation is thus linearly mapped to the rate of Cauchy stress by the fourth-order tensor of elastic moduli $\mathfrak{C}$. For the non-linear constitutive equations of soft tissue discussed in Section 3.2.1 this tensor depends on the current state of stress, whereas for a linear elastic material it is constant.

In three dimensions, $\mathfrak{C}$ has 81 components, but symmetry considerations drastically reduce the number of independent entries, that ultimately have to be determined experimentally to characterize a given elastic material. The simplest case constitutes an isotropic linear elastic material, where the material is fully described by only two constants, Young's modulus E and Poisson's ratio ν. In the models of the aortic valve presented later, a state of plane stress is further assumed, so that the stress through the thickness of the material, $\sigma_{33} = 0$ vanishes. The constitutive equations can then be written as

$$\begin{bmatrix} \dot{\sigma}_{11} \\ \dot{\sigma}_{22} \\ \dot{\sigma}_{12} \end{bmatrix} = \frac{E}{1-\nu^2} \begin{bmatrix} 1 & \nu & 0 \\ \nu & 1 & 0 \\ 0 & 0 & (1-\nu)/2 \end{bmatrix} \begin{bmatrix} D_{11} \\ D_{22} \\ 2D_{12} \end{bmatrix}. \tag{3.44}$$

3.1.6 The Objective of Stress Analysis

Equilibrium stress analysis is a boundary value problem. Given the domain B_0, a suitable constitutive model, e.g. as in equation (3.43), and prescribed conditions on the boundary of B_0, ∂B_0, the objective is to find the deformed configuration B that gives rise to internal stresses that satisfy equation (3.11).

Boundary conditions can be specified as Dirichlet boundary conditions, i.e. prescribed displacements $\bar{\mathbf{u}}$, or Neumann boundary conditions, i.e. prescribed tractions $\bar{\mathbf{t}}$. Dirichlet and Neumann boundaries (denoted by ∂B_u and ∂B_t respectively) have to be disjoint and their union must be the whole boundary ∂B_0 of B_0.

To summarize:

$$
\begin{aligned}
\operatorname{div}\boldsymbol{\sigma} + \mathbf{b} &= \mathbf{0} \ \text{ in } B, && (3.45)\\
\boldsymbol{\sigma} &= \mathbf{f}(\mathbf{F}), && (3.46)\\
\boldsymbol{\sigma}\cdot\mathbf{n} &= \bar{\mathbf{t}} \ \text{ on } \partial B_{\mathrm{t}}, && (3.47)\\
\mathbf{u} &= \bar{\mathbf{u}} \ \text{ on } \partial B_{\mathrm{u}}, && (3.48)\\
\partial B_{\mathrm{t}} \cap \partial B_{\mathrm{u}} &= \emptyset, && (3.49)\\
\partial B_{\mathrm{t}} \cup \partial B_{\mathrm{u}} &= \partial B_0. && (3.50)
\end{aligned}
$$

3.2 Constitutive Models for Aortic Valve Leaflets

3.2.1 Overview of constitutive models for soft biological tissues

It was discussed in Section 2.2.1 that aortic valve leaflets exhibit typical soft tissue mechanical behaviour. The challenge remains to capture this behaviour in mathematical form within the framework of a continuum constitutive model. Under a number of simplifications, a hyperelastic constitutive model can be formulated that describes the most prominent aspects of soft tissue mechanics.

As it was experimentally established that the stress response in soft tissues is relatively strain rate-independent and the mode of physiological operation for the tissues under consideration is cyclic loading and unloading, viscoelastic effects can be neglected. This is especially true under the further assumption that the tissue is in a pre-conditioned state. Then, to account for hysteresis, the tissue can be regarded as two hyperelastic bodies with different properties in loading and unloading. This is what Fung coined pseudo-elastic [52]. We neglect hysteresis as loading and unloading curves of pre-conditioned leaflets were relatively close (see Section 2.2.4), and treat aortic valve leaflets as a hyperelastic material.

Two main approaches exist in the formulation of a constitutive theory for soft tissues. Soft tissues are mainly composed of elastic fibres, e.g. elastin and collagen, embedded in a mucopolysaccharide matrix. The mechanical response of the tissue is the sum of the individual response of the constituents and hence the microstructural approach tries to formulate a model based on their properties. Since elastic fibres dominate the mechanical response, non-linear tissue behaviour is explained with the morphology of linear elastic fibres, e.g. through fibre waviness [33] or fibres with normally distributed lengths [43]. More complicated models include the interaction between undulated collagen fibres with pre-stretched elastin fibres which models the tissue non-linearity, while variations in angular distribution of fibres lead to anisotropy [84, 85]. These models have recently been successfully adopted for aortic valve leaflets, with the adjustment that only effective fibre stress with exponential stress-strain characteristics entered the formulation [5, 6]. The microstructural approach is appealing since the properties entering such a model can usually be interpreted physically, e.g. elastic properties of fibres, their angular distribution etc. On the other hand, due to the complexity of soft tissue composition, microstructural models are difficult to establish both theoretically and experimentally.

The other main approach is phenomenological in nature, relating gross measurable quantities, i.e. stress and strain, mathematically under the assumption of homogeneity. The functional form is chosen under theoretical constraints to fit experimental data. In the case of a soft tissue that is to be treated as a hyperelastic material, experiments suggest an exponential strain energy function

$$U = \frac{C}{2}\left(e^{Q} - 1\right), \tag{3.51}$$

where Q is a quadratic function of Green's strain [53, 52]. C is a constant and more material constants enter Q, which also govern anisotropy. These constants have no direct physical meaning but are readily determined from relatively simple experiments, e.g. uniaxial or biaxial tension tests on excised tissue strips.

Alternatively, and that is the route taken here, a compromise between microstructural and phenomenological models would be a structurally motivated phenomenological approach. The fibre-reinforced matrix structure of soft tissues can be translated into a hyperelastic constitutive model consisting of an isotropic (matrix) part augmented by contributions of one or more fibre families [74, 75, 72, 73], within the framework of finite elasticity of fibre-reinforced composites [134, 90]. Fibre families are introduced as vector fields in the material. The functional form of the strain energy functions is then again chosen to fit data from suitable tension test protocols, where the fit parameters are the material constants of the model. Detailed interactions between fibres and matrix and structural details like waviness, angular distributions are hidden in the form of the strain energy function modelling their averaged effects. In a related context, such a constitutive model has successfully been established for mitral valve tissue [96]. A more detailed account of this constitutive theory is presented in the following three sections.

3.2.2 Isotropic Hyperelastic Material Models

A hyperelastic or Green elastic material is a Cauchy elastic material for which the work done by deforming the material is path independent. In that case there exists a scalar potential function U from which the stresses can be derived. e.g. using the work conjugate pair of second Piola-Kirchhoff stress and Green's strain,

$$\mathbf{S} = \frac{\partial U(\mathbf{E})}{\partial \mathbf{E}}. \tag{3.52}$$

The work done on the material by elastic deformation is then

$$\int_{\mathbf{E}_1}^{\mathbf{E}_2} \mathbf{S} : d\mathbf{E} = \int_{\mathbf{E}_1}^{\mathbf{E}_2} \frac{\partial U(\mathbf{E})}{\partial \mathbf{E}} : d\mathbf{E} = U(\mathbf{E}_2) - U(\mathbf{E}_1). \tag{3.53}$$

and hence path independent.

Alternatively, with the use of equation (3.27), the strain energy potential U can be formulated directly in terms of the right Cauchy-Green deformation tensor which has advantages for what follows,

$$\mathbf{S} = 2\frac{\partial U(\mathbf{C})}{\partial \mathbf{C}}. \tag{3.54}$$

Since the strain energy potential U is a function of the right Cauchy-Green deformation tensor $\mathbf{C}$, the principle of material objectivity is satisfied. Any material symmetries impose further restrictions on the form of the strain energy potential. An isotropic material for instance possesses arbitrary symmetry in an undeformed configuration. If the strain energy potential in equation (3.54) is not a function of

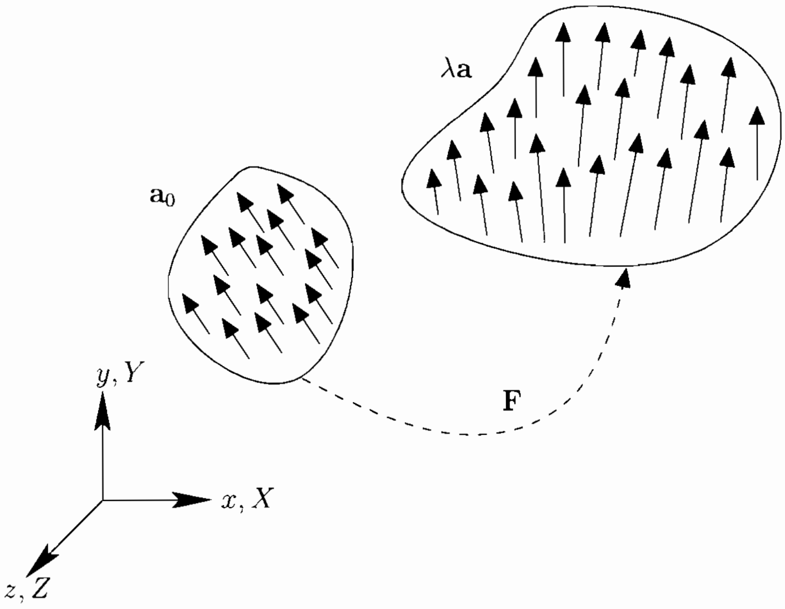

Figure 3.3: The unit vector field $\mathbf{a}_0$ embedded in the body B_0 deforms under the action of the deformation gradient $\mathbf{F}$ and is mapped on the vector field $\lambda\,\mathbf{a}$ in the deformed configuration B.

the components of $\mathbf{C}$, but is instead expressed as $U = U(I_1, I_2, I_3)$, i.e. in terms of the tensor invariants

$$I_1(\mathbf{C}) = \operatorname{tr}\mathbf{C}, \tag{3.55}$$

$$I_2(\mathbf{C}) = \frac{1}{2}\left[(\operatorname{tr}\mathbf{C})^2 - \operatorname{tr}\mathbf{C}^2\right], \tag{3.56}$$

$$I_3(\mathbf{C}) = \det\mathbf{C}, \tag{3.57}$$

then the material it describes is an isotropic material.

3.2.3 Extension to Transversely Isotropic Hyperelasticity

The restriction to isotropy in the formulation of hyperelasticity in Section 3.2.2 can be overcome by introducing a unit vector field $\mathbf{a}_0 = \mathbf{a}_0(\mathbf{X})$ in the material [134, 159, 158]. The material should be symmetric with respect to rotation about these vectors and the strain energy potential still has to retain its material objectivity.

If the material deforms under the action of the deformation gradient $\mathbf{F}$, so does the unit vector field, that can now be described with the unit vector field $\mathbf{a} = \mathbf{a}(\mathbf{x}(\mathbf{X}, t))$ as

$$\lambda \mathbf{a} = \mathbf{F} \cdot \mathbf{a}_0, \tag{3.58}$$

where λ is the fibre stretch. This is schematically shown in Figure 3.3. Since $\mathbf{a}$ is a unit vector, this fibre stretch can be determined by

$$\lambda^2 = \lambda^2 \mathbf{a} \cdot \mathbf{a} = \mathbf{F} \cdot \mathbf{a}_0 \cdot \mathbf{F} \cdot \mathbf{a}_0 = \mathbf{a}_0 \cdot \mathbf{F}^T \cdot \mathbf{F} \cdot \mathbf{a}_0 = \mathbf{a}_0 \cdot \mathbf{C} \cdot \mathbf{a}_0. \tag{3.59}$$

A material with one designated direction is a transversely isotropic material and in order to describe its mechanical behaviour, the strain energy potential equation (3.54) has to be extended to reflect the dependency on the direction $\mathbf{a}_0$. This can be achieved by introducing terms of the tensor product $\mathbf{a}_0 \otimes \mathbf{a}_0$, like

$$\begin{gathered} \mathbf{a}_0 \otimes \mathbf{a}_0, \;\; (\mathbf{a}_0 \otimes \mathbf{a}_0)^2, \;\; (\mathbf{a}_0 \otimes \mathbf{a}_0)^3, \;\; \ldots, \\ \mathbf{C} \cdot (\mathbf{a}_0 \otimes \mathbf{a}_0), \;\; \mathbf{C} \cdot (\mathbf{a}_0 \otimes \mathbf{a}_0)^2, \;\; \mathbf{C}^2 \cdot (\mathbf{a}_0 \otimes \mathbf{a}_0), \ldots, \end{gathered} \tag{3.60}$$

which is consistent with material objectivity.

Expressing the strain energy in terms of invariants of the above tensors then satisfies the material symmetries of transverse isotropy. Since $\mathbf{a}_0$ is a unit vector field

$$\mathbf{a}_0 \otimes \mathbf{a}_0 = (\mathbf{a}_0 \otimes \mathbf{a}_0)^2 = (\mathbf{a}_0 \otimes \mathbf{a}_0)^3 = \ldots, \tag{3.61}$$

and the first invariants are the traces of the remaining tensors in equation (3.60),

$$\operatorname{tr}(\mathbf{a}_0 \otimes \mathbf{a}_0) = 1, \tag{3.62}$$

$$I_4(\mathbf{C}, \mathbf{a}_0) = \operatorname{tr}(\mathbf{C} \cdot (\mathbf{a}_0 \otimes \mathbf{a}_0)) = \mathbf{a}_0 \cdot \mathbf{C} \cdot \mathbf{a}_0, \tag{3.63}$$

$$I_5(\mathbf{C}, \mathbf{a}_0) = \operatorname{tr}(\mathbf{C}^2 \cdot (\mathbf{a}_0 \otimes \mathbf{a}_0)) = \mathbf{a}_0 \cdot \mathbf{C}^2 \cdot \mathbf{a}_0 \ldots \tag{3.64}$$

Since the second and third invariants of equation (3.60) vanish, the above are the only new invariants in addition to the isotropic invariants equation (3.55). A transversely isotropic material can then be described by a strain energy function of the invariants $U = U(I_1, I_2, I_3, I_4, I_5)$.

In that case, the second Piola-Kirchhoff stress is evaluated from

$$\mathbf{S} = 2\frac{\partial U(I_1, I_2, I_3, I_4, I_5)}{\partial \mathbf{C}} = 2\left(\frac{\partial U}{\partial I_i}\frac{\partial I_i}{\partial \mathbf{C}}\right), \tag{3.65}$$

where summation over $i = 1 \ldots 5$ is implied.

Using the results

$$\begin{aligned}
\frac{\partial I_1}{\partial \mathbf{C}} &= \mathbb{I} && (3.66)\\
\frac{\partial I_2}{\partial \mathbf{C}} &= I_1\mathbb{I} - \mathbf{C} && (3.67)\\
\frac{\partial I_3}{\partial \mathbf{C}} &= I_2\mathbb{I} - I_1\mathbf{C} + \mathbf{C}^2 = I_3\mathbf{C}^{-1} && (3.68)\\
\frac{\partial I_4}{\partial \mathbf{C}} &= \mathbf{a}_0 \otimes \mathbf{a}_0 && (3.69)\\
\frac{\partial I_5}{\partial \mathbf{C}} &= \mathbf{a}_0 \otimes \mathbf{C}\cdot\mathbf{a}_0 + \mathbf{a}_0\cdot\mathbf{C}\otimes\mathbf{a}_0, && (3.70)
\end{aligned}$$

where the identity tensor $\mathbb{I}$ has been introduced, the second Piola-Kirchhoff stress is [159, 158]

$$\begin{aligned}
\mathbf{S} = 2\bigg\{ &\left(\frac{\partial U}{\partial I_1} + I_1\frac{\partial U}{\partial I_2} + I_2\frac{\partial U}{\partial I_3}\right)\mathbb{I} - \left(\frac{\partial U}{\partial I_2} + I_1\frac{\partial U}{\partial I_3}\right)\mathbf{C} + \frac{\partial U}{\partial I_3}\mathbf{C}^2\\
&+\frac{\partial U}{\partial I_4}\mathbf{a}_0\otimes\mathbf{a}_0 + \frac{\partial U}{\partial I_5}\left(\mathbf{a}_0\otimes\mathbf{C}\cdot\mathbf{a}_0 + \mathbf{a}_0\cdot\mathbf{C}\otimes\mathbf{a}_0\right)\bigg\}. \qquad (3.71)
\end{aligned}$$

The Cauchy stress is obtained from a push forward of the second Piola-Kirchhoff stress according to equation (3.38).

3.2.4 The Choice of a Strain Energy Potential for Aortic Leaflet Tissue

The functional form of the strain energy potential has to be chosen to comply with experimental observations of the material. The first step towards a choice for a strain energy potential for aortic valve leaflets is therfore the restriction to incompressible materials. The principle of conservation of mass then dictates that

$$I_3 = \det\mathbf{C} = \det\mathbf{F} = 1. \qquad (3.72)$$

Additionally, we seek the simplest form that can reproduce material behaviour, thus restricting the functional dependence of U on I_1 and I_4, thus $U = U(I_1, I_4)$. It then follows from equation (3.71) that

$$\mathbf{S} = 2\left\{\frac{\partial U}{\partial I_1}\mathbb{I} + \frac{\partial U}{\partial I_4}\mathbf{a}_0\otimes\mathbf{a}_0\right\} + p\,\mathbf{C}^{-1}, \qquad (3.73)$$

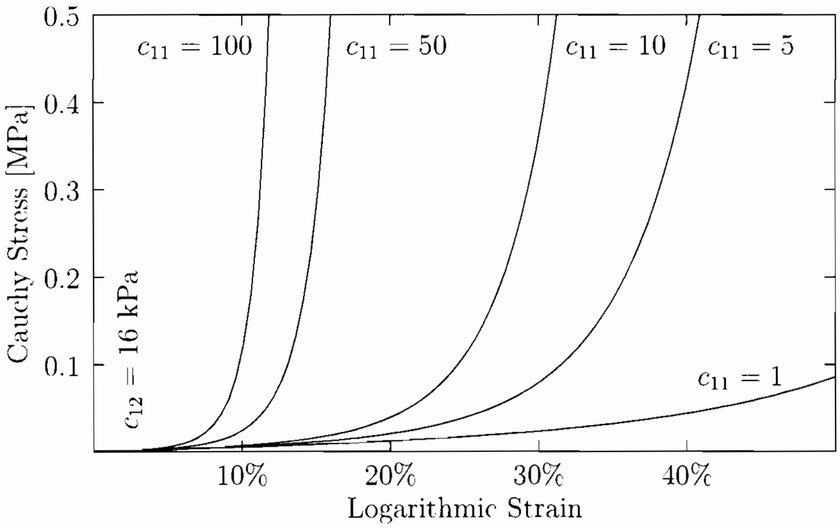

Figure 3.4: Stress-strain plots on the basis of strain energy potential U_1 at constant $c_{12} = 16$ kPa. The varying parameter c_{11} governs the transition behaviour from the initial compliant towards the stiff phase of the stress response.

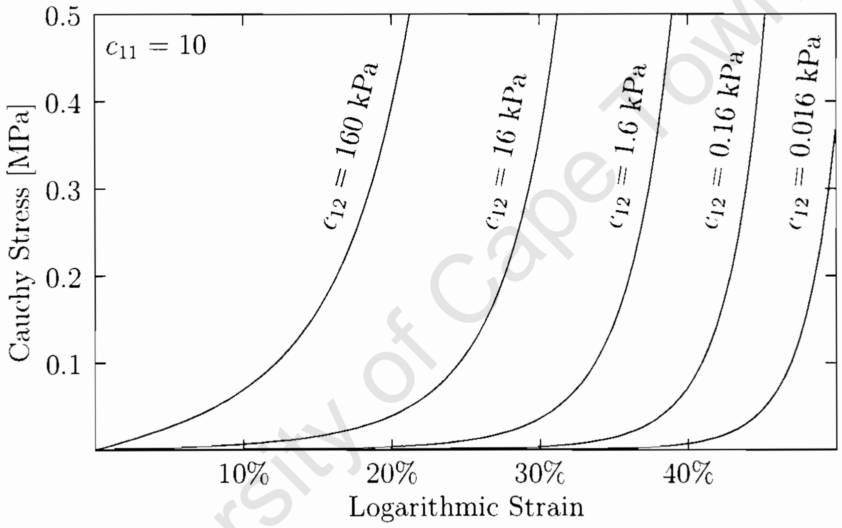

Figure 3.5: Stress-strain plots on the basis of strain energy potential U_1 at constant $c_{11} = 10$. The varying parameter c_{12} defines the stress scale and as a result, the plots shift to the left for increasing c_{12}.

and the Cauchy stresses are

$$\boldsymbol{\sigma} = \mathbf{F} \cdot \mathbf{S} \cdot \mathbf{F}^T = 2\left\{ \frac{\partial U}{\partial I_1} \mathbf{B} + I_4 \frac{\partial U}{\partial I_4} \mathbf{a} \otimes \mathbf{a} \right\} - p\mathbb{I}. \tag{3.74}$$

Note that instead of terms involving I_3 and its derivatives, an unknown hydrostatic pressure p enters equations (3.73) and (3.74).

A further restriction on the desired strain energy potential is a decoupling of an isotropic matrix reinforced with one fibre family, so that

$$U = U(I_1, I_4) = U_1(I_1) + U_4(I_4). \tag{3.75}$$

That is to say that aortic valve leaflets are here idealized as a family of dense non-interacting fibres governed by U_4, embedded in a homogeneous isotropic matrix U_1 [74], an assumption shared with many structural models, e.g. [84, 85, 131].

For the isotropic part U_1 we use a form that has been proposed as a specialization to incompressibility [44] of a strain energy potential proposed for skin [146], and has been used in the context of heart valves before [27], viz.

$$U_1 = \frac{c_{12}}{2c_{11}} (e^{c_{11}(I_1-3)} - 1) \; . \tag{3.76}$$

The proposed U_1 has the special property, that the first term of a power series expansion reduces to the strain energy function proposed for vulcanized rubber [100].

Equation (3.76) introduces two constants that have to be determined from experiments, where c_{12} in units of stress defines the scale and c_{12} influences the transition behaviour from the compliant to the stiff phase of the exponential. The role of the parameter c_{11} is illustrated in Figure 3.4 and of c_{12} in Figure 3.5 for uniaxial tension.

If no deformation occurs, i.e. $I_1 = 3$, the strain energy vanishes as required, the first derivative however, that enters the stresses, does not. The hydrostatic pressure term in equation (3.73) and equation (3.74) has then to take care of the requirement that the stress should vanish in that case.

A similar form to equation (3.76) is employed for the fibre reinforcement U_4. Because of the non-vanishing first derivative in an initial configuration, some modifications are necessary. The first derivative of this part does not enter equation (3.73) and equation (3.74) volumetrically, but is governed by the direction $\mathbf{a}$ and therfore must vanish if no deformation occurs, i.e. $I_4 = 1$. Because of the nature of the collagen fibres U_4 is supposed to model, it is further assumed that U_4 only contributes in tension. The collagen fibres thus do not take up compressive stresses, again in agreement with structural models [84, 85, 131]. Taking into account these considerations, a possible functional form for U_4 is then

$$U_4 = \begin{cases} 0, \quad I_4 < 0 \\ \frac{c_{42}}{2c_{41}}\left(e^{c_{41}(I_4-1)^2} - 1\right), \quad I_4 \geq 0. \end{cases} \tag{3.77}$$

Again, the two constants c_{41} and c_{42} have to be determined from mechanical tests and their role is similar to the constants in U_1.

The resulting strain energy function is similar to the one proposed in [74]. Through the introduction of a fibre family in an isotropic matrix it is structurally motivated. Details of fibre waviness, interaction of undulated collagen fibres with elastin fibres etc., are however absorbed in an exponential stress response of the fibres. Variations in angular distribution of fibres leading to contributions to stresses in direction other than in the direction of the fibres are incorporated in the exponential form of the isotropic matrix part.

3.3 The Finite Element Method

In the concluding sections of this chapter an outline of the finite element method will be presented, especially of those aspects relevant to ABAQUS, the finite element package used for the work herein [68]. The features of ABAQUS used here amount to an updated Lagrangian displacement-based Galerkin finite element method. This approach is Eulerian in the sense that integrals are evaluated in the current configuration, but Lagrangian since the mesh is moving with the material. The test and trial functions used to discretize the weak form are based on nodal coordinates. For further reference, many detailed accounts on the finite element method can be found in the literature, e.g. [35, 36, 4].

3.3.1 Weak Form of Cauchy's Equation of Motion

As with any numerical technique, the governing partial differential equations of the previous sections have to be discretized to obtain algebraic expressions that can be solved on a computer. The first step towards this goal is to state the equation of motion equation (3.10) in an equivalent integral form using a variational principle, e.g. the principle of virtual power. To this end we define virtual velocities as test functions belonging to the space

$$\mathcal{V}_0 = \{\delta\mathbf{v} | \delta v_i \in \mathcal{H},\ \delta\mathbf{v} = \mathbf{0} \text{ on } \partial B_{\mathrm{v}}\}, \tag{3.78}$$

where $\mathcal{H}$ is a function space (e.g. a Sobolev space) that is chosen appropriately.

Similarly, the kinematically admissible trial velocities belong to the space

$$\mathcal{V} = \{\mathbf{v} | v_i \in \mathcal{H},\ \mathbf{v} = \bar{\mathbf{v}} \text{ on } \partial B_{\mathrm{v}}\}. \tag{3.79}$$

Now taking the product of virtual velocities and equation (3.10) and integrating over the current configuration, we obtain

$$\int_B \delta\mathbf{v} \cdot \left(\operatorname{div} \boldsymbol{\sigma} + \mathbf{b} - \rho \frac{D\mathbf{v}}{Dt} \right) dV = 0. \tag{3.80}$$

The arbitrariness of the virtual velocities in this vanishing integral implies the equation of motion as in equation (3.11).

Expansion of the first term in equation (3.80) leads to

$$\int_B \delta\mathbf{v} \cdot \operatorname{div} \boldsymbol{\sigma}\, dV = \int_B \left[\frac{\partial}{\partial \mathbf{x}} (\delta\mathbf{v} \cdot \boldsymbol{\sigma}) - \frac{\partial(\delta\mathbf{v})}{\partial \mathbf{x}} : \boldsymbol{\sigma} \right] dV. \tag{3.81}$$

The first term in the above integral can be expressed as an integral over the prescribed Neumann boundaries using Gauss's theorem and recalling that the test functions vanish on the complement of these boundaries. This gives

$$\int_B \frac{\partial}{\partial \mathbf{x}} (\delta\mathbf{v} \cdot \boldsymbol{\sigma})\, dV = \int_{\partial B} \boldsymbol{\sigma} \cdot \mathbf{n} \cdot \delta\mathbf{v}\, dA = \int_{\partial B_{\mathrm{t}}} \delta\mathbf{v} \cdot \bar{\mathbf{t}}\, dA. \tag{3.82}$$

Collecting terms, we finally arrive at an alternative statement for equilibrium, in the form

$$\int_B \delta\mathbf{D} : \boldsymbol{\sigma}\, dV = \int_{\partial B_{\mathrm{t}}} \delta\mathbf{v} \cdot \bar{\mathbf{t}}\, dA + \int_B \delta\mathbf{v} \cdot \mathbf{b}\, dV - \int_B \delta\mathbf{v} \cdot \rho \frac{D\mathbf{v}}{Dt}\, dV, \tag{3.83}$$

where equation (3.33) has been used on the left hand side. This is a weak form of Cauchy's equation of motion in equation (3.10), since derivatives of the stresses have been eliminated and hence continuity requirements on the stresses are relaxed.

3.3.2 Spatial Discretization

The essence of the finite element method is now to split the domain of integration in equation (3.83) into subdomains, the elements, of simple shapes like triangles or quadrilaterals in such a way that the union of all elements approximates the original domain. Depending on the shapes of the elements the subdivision is only approximate since curved boundaries might be replaced by straight edges. Moreover it is required that the elements do not overlap, do not leave gaps and that corners are coincident. Then the integral over the domain B is replaced by a sum of integrals over the elements B_e; that is,

$$\int_B (\cdot)\, dV \approx \sum_e \int_{B_e} (\cdot)\, dV_e. \tag{3.84}$$

Since the shapes of the elements are simple, the coordinates of any point $\mathbf{x}$ of B in the finite element approximation can be written as an interpolation using a finite set of nodal values, e.g. at the corners of elements.

$$\mathbf{x}(\mathbf{X}, t) = \mathbf{x}_I(t) N_I(\mathbf{X}), \tag{3.85}$$

where the index I is over the number of nodes and summation of repeated indices is implied. The shape functions N_I have the interpolation property

$$N_I(\mathbf{X}_J) = \delta_{IJ}, \tag{3.86}$$

where δ_{IJ} is the Kronecker delta. Consequently, a node $\mathbf{x}_I$ always corresponds to the same material point $\mathbf{X}_I$ and a Lagrangian mesh that moves with the material is obtained.

The displacement field is derived from equation (3.85) as

$$\mathbf{u}(\mathbf{X}, t) = \mathbf{x} - \mathbf{X} = \mathbf{u}_I(t) N_I(\mathbf{X}). \tag{3.87}$$

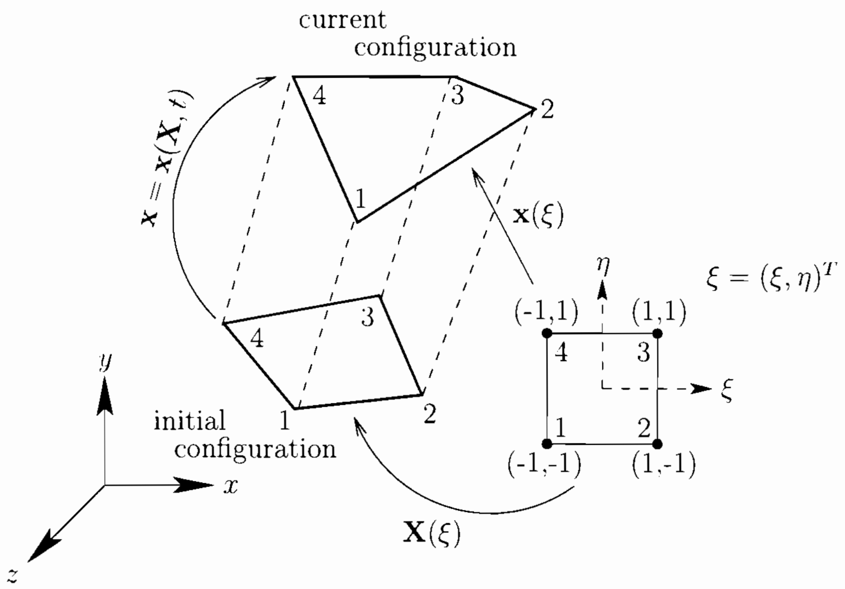

Figure 3.6: A parent element is mapped onto an element in the initial or current configuration for the numerical quadrature.

and the velocity field as

$$\mathbf{v}(\mathbf{X}, t) = \frac{\partial \mathbf{u}(\mathbf{X}, t)}{\partial t} = \dot{\mathbf{u}}_I(t) N_I(\mathbf{X}) = \mathbf{v}_I(t) N_I(\mathbf{X}). \tag{3.88}$$

It then follows that the velocity gradient is given by

$$\mathbf{L} = \frac{\partial \mathbf{v}}{\partial \mathbf{x}} = \mathbf{v}_I \otimes \frac{\partial N_I}{\partial \mathbf{x}}, \tag{3.89}$$

from which the rate of deformation tensor is obtained as the symmetric part.

In the Galerkin method the test functions are interpolated by nodal values in the same way the trial functions are, so the virtual velocities are then written as

$$\delta\mathbf{v}(\mathbf{X}) = \delta\mathbf{v}_I N_I(\mathbf{X}). \tag{3.90}$$

Substituting these interpolations in the weak form integrals equation (3.83) and using the fact that the spatial dependency of the interpolated fields lies entirely in the shape function, we get

$$\delta\mathbf{v}_I \cdot \int_B \boldsymbol{\sigma} \cdot \frac{\partial N_I}{\partial \mathbf{x}} \, dV - \delta\mathbf{v}_I \cdot \int_{B_t} N_I \bar{\mathbf{t}} \, dA - \delta\mathbf{v}_I \cdot \int_B N_I \mathbf{b} \, dV + \delta\mathbf{v}_I \cdot \int_B N_I \rho \frac{D\mathbf{v}}{Dt} \, dV = 0. \tag{3.91}$$

Inertial or kinetic nodal forces can be defined as

$$\mathbf{f}_I^{kin} = \int_B N_I \rho \frac{D\mathbf{v}}{Dt} \, dV, \tag{3.92}$$

where the material time derivative of velocities in this case are, similar to equation (3.88), given by

$$\frac{\partial \mathbf{v}(\mathbf{X}, t)}{\partial t} = \dot{\mathbf{v}}_I(t) N_I(\mathbf{X}). \tag{3.93}$$

Using this last result in equation (3.92), and defining the mass matrix by

$$\mathbf{M}_{IJ} = \int_B \rho N_I N_J \, dV, \tag{3.94}$$

the inertial nodal forces can be written as

$$\mathbf{f}_I^{kin} = \mathbf{M}_{IJ} \dot{\mathbf{v}}_J = \mathbf{M}_{IJ} \mathbf{a}_J. \tag{3.95}$$

Defining furthermore internal and external nodal forces respectively by

$$\mathbf{f}_I^{int} = \int_B \boldsymbol{\sigma} \cdot \frac{\partial N_I}{\partial \mathbf{x}} \, dV \quad \text{and} \tag{3.96}$$

$$\mathbf{f}_I^{ext} = \int_{B_t} N_I \bar{\mathbf{t}} \, dA + \int_B N_I \mathbf{b} \, dV, \tag{3.97}$$

and invoking the arbitrariness of $\delta\mathbf{v}$ for all free nodes, equation (3.91) can be written in matrix form as

$$\mathbf{f}^{int} - \mathbf{f}^{ext} + \mathbf{M}\mathbf{a} = \mathbf{0}, \tag{3.98}$$

the semi-discrete finite element equations.

In practice, the integrals in equation (3.95), (3.96) and (3.97) for the nodal forces are evaluated by numerical integration, e.g. Gauss quadrature. To this end, a parent element is mapped one-to-one onto the element in the desired physical configuration as illustrated in Figure 3.6. The integrals over the element are then related to integrals over the parent element by the Jacobian of the map and computed by weighted sums of a finite set of integration points.

3.3.3 Solution of Non-linear Systems of Equations

The semi-discrete finite element equations (3.98) are ordinary differential equations in time for all unrestricted degrees of freedom in the model. Together with the prescribed degrees of freedom they can be solved by discretizing the time. In an equilibrium problem, the accelerations vanish and if additionally the material constitutive model equation (3.43) is rate independent, as in our context, time here merely becomes a parameter that can be used for load control. The resulting equations are non linear algebraic equations in the displacements and the Newton-Raphson method is used for solving them.

3.3.4 Finite Element Implementation of Transversely Isotropic Hyperelasticity

The constitutive model presented in Section 3.2 has to be implemented in the finite element context. In the general three-dimensional case, incompressibility introduces a challenge because of the unknown hydrostatic pressure entering the stress calculation. The solution then can be tackled by multiplicatively splitting the deformation gradient and thus decoupling the deviatoric and dilational responses. A mixed finite element method is then employed for discretization [158].

In the present context however, the models of the aortic valve will make use of shell elements under Reisner-Mindlin assumptions, i.e. fibres initially straight and normal to the shell will remain straight after deformation. Incompressibility will be enforced by a thickness change. Furthermore the material is assumed to be in a state of plane stress. This assumption then determines the hydrostatic pressure [69]. If σ_{33} denotes the stress in the normal (thickness) direction of the shell, we obtain from equation (3.74).

$$\sigma_{33} = 2\frac{\partial U}{\partial I_1} B_{33} + p = 0 \Leftrightarrow p = -2\frac{\partial U}{\partial I_1} B_{33}, \qquad (3.99)$$

where the transversely isotropic terms vanish if **a** remains in-plane as will be the case here.

The finite element equations need to be linearized for the Newton-Raphson solution procedure. For this purpose the stresses entering the internal nodal forces are required in rate form, from equation (3.54); that is,

$$\dot{\mathbf{S}} = \frac{\partial \mathbf{S}}{\partial \mathbf{E}} : \dot{\mathbf{E}} = \frac{\partial^2 U}{\partial \mathbf{E} \partial \mathbf{E}} : \dot{\mathbf{E}} = 4 \frac{\partial^2 U}{\partial \mathbf{C} \partial \mathbf{C}} : \frac{\dot{\mathbf{C}}}{2}. \tag{3.100}$$

From the above, the second elasticity tensor or the tangent moduli are defined as

$$\mathfrak{C}^{SE} = 4 \frac{\partial^2 U}{\partial \mathbf{C} \partial \mathbf{C}}. \tag{3.101}$$

The tangent moduli for the hypoelastic constitutive equation in the current configuration equation (3.43) are then obtained by the push forward of the above, in component form, to give

$$\mathfrak{C}_{ijkl} = \frac{1}{J} F_{im} F_{jn} F_{ko} F_{lp} \mathfrak{C}^{SE}_{mnop}. \tag{3.102}$$

where it has to be kept in mind that these moduli are merely the material contribution, and further modifications are in order, depending on which objective rate of Cauchy stress is used.

The isotropic part of the *incompressible* elasticity tensor equation (3.101), i.e. the part corresponding to U_1, taking into account the plane stress constraint, can be obtained in terms of principal stretches and rotated accordingly [69]. The moduli then depend on second derivatives of the strain energy potential U_1. Any isotropic strain energy potential can be implemented in ABAQUS by a user supplied subroutine UHYPER, the only requirement being the coding of the strain energy potential and its derivatives. Further details of this implementation can be found in Appendix B.

The transverse direction is introduced in the elements by defining reinforcement in elements, termed REBAR in ABAQUS. The material behaviour of the REBAR-fibres is governed by the transversely isotropic extension of the strain energy potential, U_4. This part is implemented in ABAQUS by means of a user supplied subroutine UMAT. This subroutine has to handle the stress calculations and computation of the tangent moduli. In the case of a user material for REBARS, ABAQUS handles the modifications required to obtain a objective tangent moduli, and only the material part has to be considered. These are then obtained from equation (3.101) with U_4 [158],

$$\mathfrak{C}_f^{SE} = \frac{\partial^2 U_4}{\partial I_4^2} \mathbf{a}_0 \otimes \mathbf{a}_0 \otimes \mathbf{a}_0 \otimes \mathbf{a}_0, \tag{3.103}$$

and in the current configuration

$$\mathfrak{C}_f = \frac{\partial^2 U_4}{\partial I_4^2} I_4^2 \, \mathbf{a} \otimes \mathbf{a} \otimes \mathbf{a} \otimes \mathbf{a}. \tag{3.104}$$

Further details of the implementation of U_4 in ABAQUS can be found in Appendix C.

Chapter 4

Non–linear Finite Element Analyses of the Aortic Valve

In this chapter the finite element models of the aortic valve are presented and the results of the simulations are discussed.

4.1 Model Properties

4.1.1 Geometry

It was discussed in Section 2.1.3 that the aortic valve is an asymmetric structure that also changes during its lifetime. It is thus only possible to geometrically model the valve in a representative way. Here, this was done by neglecting asymmetry and assuming a smooth well-defined geometry of the valve. For the sake of simplicity, only uniform thickness was assigned to the aortic root and the leaflets. The dimensions used are in accordance with what was discussed in Section 2.1.4.

The starting point of modelling the geometry is then an aortic valve reduced to three identical sinus–leaflet constructs rotated 120° each around the direction of blood flow. Furthermore each sinus leaflet construct has a symmetry plane at the centre. Under these assumptions it is sufficient to model one sixth of the aortic valve with the appropriate symmetry boundary conditions.

The basis for the constructed valve is then formed by a cylindrical tube. The

Author	r_a	r_v	r_s	h_l	h_s
this study	12.5	12.5	18.25	17.75	22.0
Cacciola et al. [11]	12.0	12.0	16.0	(16.0)–17.0	20.0
De Hart et al. [41]	12.0	12.0	17.75	(16.8)–10.5	21.0
Gnyaneshwar et al. [55]	12.0	12.0	17.52	(16.8)–17.0	21.12
Grande et al. [58]		12.5			
Beck et al. [2]	13.0	13.0		18.0	

Table 4.1: Dimensions of the aortic valve model in mm used here and in other studies.

leaflets are cut out of this tube by an orthogonal intersection of a cylindrical extrusion of the planar projection of a leaflet in the open position. The curves of this intersection form a three-pointed coronet, the lines of leaflet attachment. In a similar way the open space between the sinotubular junction and the free edge of the leaflet is constructed. Lastly, the line of leaflet attachment and the sinotubular junction together form the closed line on the original tube where the bulges of the sinuses of Valsalva originate. As the projected outline of the aortic root as seen against the direction of blood flow resembles an epitrochoid, the line of greatest depth of the sinus was assumed to form part of a circle about halfway between the bottom of the line of leaflet attachment and the top of the sinotubular junction. For symmetry reasons the sinus depth reaches its maximum on the symmetry plane of a sinus–leaflet construct. The line of greatest depth in this plane was constructed by fitting a NURBS (Nonuniform rational B–Splines) line through the lowest point of the line of leaflet attachment, the point of greatest sinus depth and the highest point of the sinotubular junction. The sinus was then constructed by a NURBS surface containing all these lines. The geometry was modelled using GiD [76] with dimensions as listed in Table 4.1 and Table 4.2 in the context of previously published valve models, and subsequently imported into ABAQUS CAE [68] for the creation of the finite element mesh. Both geometry and mesh, consisting of 3 triangular and 1544 quadrilateral elements for the sinus and 600 quadrilateral elements for the leaflet are shown in Figure 4.1.

Author	t_l	t_s	Source of geometrical data
this study	0.2	1.0	derived from [139]
Cacciola et al. [11]	0.2	0.4	derived from prosthesis prototype
De Hart et al. [41]	0.2	1.0	derived from prosthesis prototype
Gnyaneshwar et al. [55]	0.25–1.33		derived from [141]
Grande et al. [58]	0.18–2.75	0.6–3.78	literature (leaflet) and measurements (root)
Beck et al. [2]	0.5	1.3	derived from [139]

Table 4.2: Thickness in mm of the aortic valve model as used in this study and by other researchers.

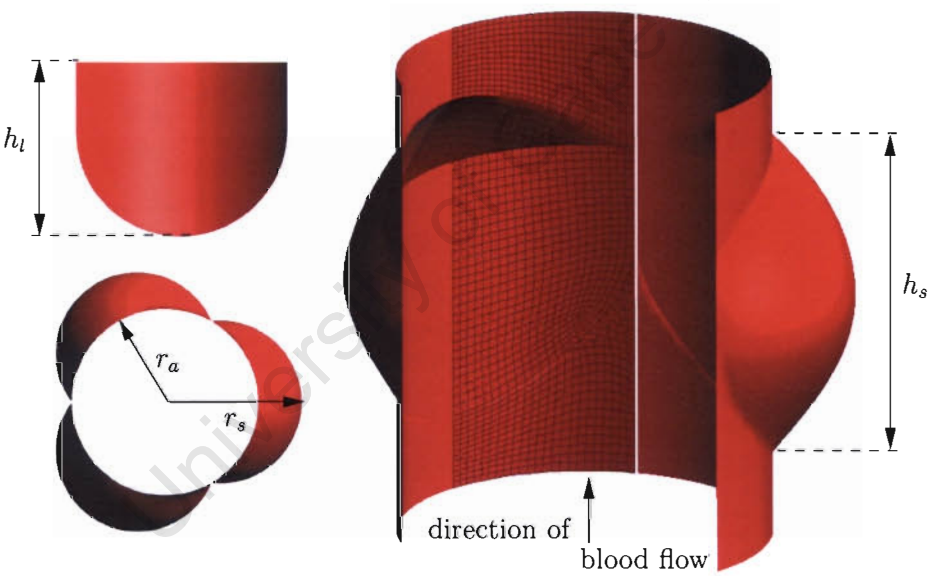

Figure 4.1: Model valve geometry in the undeformed configuration and finite element mesh.

4.1.2 Boundary Conditions

To take care of the model symmetry as discussed in the previous section, appropriate boundary conditions are applied to the nodes on the lines in the symmetry planes, the vertical lines in Figure 4.1: Only radial displacement and rotation about the horizontal tangent at these nodes is allowed. Additionally, the nodes on the circular lines of the bottom and top of the valve are confined to the plane of their original configuration.

4.1.3 Loading Conditions

As was discussed in Section 2.1.5, the dynamics of the aortic valve during the heart cycle is complex and a result of interaction of blood flow with the compliant tissue structure. In the simulations discussed here this is modelled only in a most simplified fashion by the application of uniform pressure on the ventricular and aortic surfaces of the valve. Neglecting inertial and viscoelastic effects, the time scale of the heart cycle to be modelled is irrelevant, so that the loading cycle is as follows: Starting from the undeformed configuration in Figure 4.1 at $p = 0\,\text{mmHg}$, pressure is ramped up uniformly on all inside surfaces, first to the diastolic pressure value of $p = 80\,\text{mmHg}$, followed by the systolic pressure of $p = 120\,\text{mmHg}$ and back to the diastolic pressure of $p = 80\,\text{mmHg}$. That completes the systolic loading phase that was used for compliance adjustment detailed in Section 4.1.4. It is also the starting point for diastolic loading, where the pressure on the ventricular surfaces, i.e. in Figure 4.1 the visible face of the leaflet and the surface of the aortic root below the lines of leaflet attachment, drops to $p = 0\,\text{mmHg}$.

As a result of the pressure drop on the ventricular side, the leaflet will close, moving towards the centre of the valve. In order to simulate contact with the other leaflets and hence the closure of the valve, a contact surface is introduced in the model. That surface is formed by a rigid plane through the centre of the valve and a point outside of the sinus–leaflet construct, on the right side of the mesh in Figure 4.1. Contact of nodes is established using an exponential pressure-overclosure relationship with a diastolic pressure value at zero overclosure [68], i.e. in contact diastolic pressure is acting on both sides and an exponentially rising pressure with increasing overclosure is preventing leaflet penetration. Once in contact, nodes can slide in a frictionless manner on the contact plane.

4.1.4 Constitutive Model for the Aortic Root

The use and comparison of different material models for the leaflet is at the heart of the modelling efforts presented here. To provide a physiologically relevant environment for the leaflet, it should operate with a compliant aortic root. To this end an isotropic linear elastic material is assigned to the root wall. In a first run, Young's modulus of the material is set to $E_{s1} = 1.3$ MPa. From the systolic phase of the loading cycle, aortic root compliance is then calculated by

$$C_D = \frac{\Delta D}{D_{es} \cdot \Delta P} \times 10^4, \tag{4.1}$$

where ΔD is the difference in peak systolic and end systolic diameter, D_{es} the end systolic diameter and ΔP pulse pressure, i.e. the difference between systolic and diastolic pressures in mmHg. The diameters are measured at the top node of the aortic root lying in the symmetry plane of the sinus leaflet construct. In subsequent runs Young's modulus of the root is adjusted until the simulated root compliance yields $C_D = 26.4 \frac{\%}{100\,\mathrm{mmHg}}$, a value measured in vivo in humans [135].

4.1.5 Constitutive Models for Aortic Valve Leaflets

To study the impact of the use of various constitutive models for the aortic valve leaflets on the stress results, four models are considered here, two linear and two hyperelastic with an isotropic and a transversely isotropic case respectively. For all linear elastic models, including the aortic root, Poisson's ratio is set to 0.4999 to account for incompressibility of soft tissues as discussed in Section 2.2.1. Young's moduli for the linear elastic (LE) models are 6.885 MPa [58, 2] for the isotropic (ILE) and the circumferential leaflet direction of the transversely isotropic model (TILE), and a modulus of 1.624 MPa in other directions in the latter.

The parameters for the hyperelastic (HYP) models presented in Section 3.2.4 are obtained from fits to typical results of uniaxial tension tests of fresh porcine aortic valve leaflets discussed in Section 2.2.4. Details of the fitting procedure can be found in Appendix A. For the isotropic hyperelastic (IHYP) model the strain energy function equation (3.76) is used to fit the tension results of the circumferential strip. The strain energy parameters thus obtained are $c_{11} = 137.959$ and $c_{12} = 14.3993$ kPa. The transversely isotropic hyperelastic (TIHYP) model uses the same strain energy function, but fitted to the results of the radial strip with parameters $c_{11} = 4.74826$ and $c_{12} = 27.3732$ kPa. To account for the anisotropy in this model, hyperelastic fibre reinforcement is introduced in the circumferential direction and equation (3.77) is used as a basis for a fit to the circumferential test data. The parameters obtained are $c_{41} = 80.4291$ and $c_{42} = 11.9752$ kPa. Both strain energy parts in equation (3.76) and equation (3.77) contribute to the stresses in the circumferential direction, but since these are so dramatically higher than in the radial direction, the portion due to equation (3.76) has been neglected in the fit.

The material models used in this study are summarized graphically in Figure 4.2. The dashed lines show the linear elastic models in uniaxial tension while the solid curve depicts the hyperelastic models in radial and circumferential directions. The latter show good agreement with uniaxial tension tests data of the porcine leaflets.

To verify the implementation of equations (3.76) and (3.77) via the subroutines presented in Appendix B and Appendix C, single–element uniaxial tension test simulations with the relevant strain energy parameters have been set up. The stress output shown in Figure 4.2 as a control is in excellent agreement with the analytical solution.

4.2 Results

4.2.1 Compliance Adjustment

Compliance adjustment slightly depends on the leaflet material used, i.e. the leaflet constitutive model has an impact on aortic root dilation. The parameters for Young's modulus for the various models are listed in Table 4.3. As mentioned earlier in Section 4.1.4 this value is based on the top node of the aortic root in peak systolic and end systolic configuration, except for the IHYP model. Due

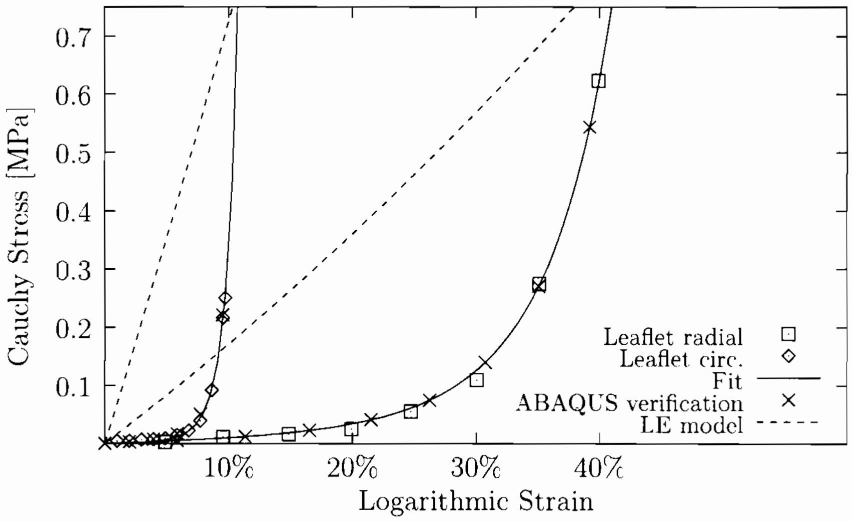

Figure 4.2: Uniaxial tension test results of fresh porcine aortic valve leaflets together with fits of the proposed constitutive models and ABAQUS UMAT verification. The dashed line shows the linear elastic model for comparison

to an excessive need of increments to complete the loading cycle in that case, it was not feasible to decrease loading from peak systolic back to end systolic pressure. Instead, the configuration at beginning of systolic loading, which is at the same pressure, was used, both to establish compliance and as a starting point for diastolic loading. This required the restarting of the analysis at beginning systolic loading and an intermediate switch to Riks' arc length method [114, 34] to obtain an equilibrium solution.

Table 4.3 also lists the simulated compliance of the initial analysis with a value of $E_{s1} = 1.3\,\mathrm{MPa}$ for Young's modulus of the aortic root. The greatest increase in compliance was in the ILE model. But despite this increase in compliance by 11 % the impact on the stress and strain fields of the leaflet were unspectacular. The greatest deviation of the compliance adjusted from the initial results was 2.6 % in the minimum principal stress on the aortic side of the leaflet. The TIHYP model showed the least increase in compliance, but due to the non–linearity of its leaflet material, the highest variation was 8% in minimum principal strain on the aortic leaflet side. Most other peak values in the ILE, TILE and TIHYP models varied

Leaflet Model	C_D [%/(100 mmHg)]	E_{s2} [MPa]
ILE	23.8	1.22155
IHYP	24.8	1.24901
TILE	26.0	1.28982
TIHYP	26.3	1.29758

Table 4.3: Initial compliance C_D with $E_{s1} = 1.3$ MPa and Young's modulus of the aortic root E_{s2} after compliance adjustment for the various leaflet models.

Node	Undeformed	Peak Systole	End Systole	Diastole
T	12.50 mm±0%	15.59 mm±0%	14.09 mm±0%	14.01 mm±1%
STJ	12.50 mm±0%	15.76 mm±0%	14.25 mm±0%	14.17 mm±1%
C	12.50 mm±0%	15.98 mm±2%	15.23 mm±2%	13.41 mm±4%
SC	18.25 mm±0%	19.90 mm±0%	19.17 mm±0%	18.99 mm±0%
LA	12.50 mm±0%	14.76 mm±2%	13.84 mm±2%	12.78 mm±4%
B	12.50 mm±0%	14.91 mm±1%	13.90 mm±1%	12.78 mm±3%

Table 4.4: Radii from the valve axis to nodes at different heights on the central symmetry line of the aortic root and the top of the commissural heights (Mean values of the four models ± relative error). Top (T), Sinotubular Junction (STJ), Commissures (C), Sinus Centre (SC), Leaflet Attachment (LA), Bottom (B).

by less than 1%. In the IHYP model however, the 6% increase in compliance had a profound impact on the peak values of principal stress on the aortic side, with a maximum change of 78% in the lower bound of the minimum principal stress. Other stress peak values changed only by a maximum of 25%. This is a consequence of the highly nonlinear stress–strain relationship in this case, since most principal strain results lie within 2% of each other. In view of the above, it is considered sufficient to discuss only the compliance adjusted results in what follows.

4.2.2 The Aortic Root

The aortic root dilates as a reaction to internal blood pressure during the cardiac cycle. Various radii measured from the valve axis at different load states of the valve are listed in Table 4.4, i.e. mean values of the four models. The relative errors are small, less than 0% for the central nodes above leaflet attachment during systole and a maximum of only 4% in the vicinity of leaflet attachment and the top of the commissural heights during diastole. Top and sinotubular junction dilate by 11% from diastole to peak systole, the commissures by 19%, the sinus centre by 5%, leaflet attachment by 15% and the bottom node by 17%. From peak systole to end systole, radii above the sinotubular junction reduce by 10%, at the commissures by 5%, the sinus centre by 4%, and below the leaflet attachment between 6% and 7%. From end systolic to diastolic configuration, central nodal radii above leaflet attachment reduce only by 1%, and by 8% below. Commissural radius decreases by 12%.

The nature of the stress and strain fields during peak systole is depicted in the vector plots of principal strain in Figure 4.3. There is no qualitative difference between the four valve models. Since the aortic root material used in the simulations is isotropic, stress and strain fields are collinear. Maximum principal stress and strain are grossly aligned circumferentially. From top to bottom, this alignment first transforms to follow roughly the curvature of the sinotubular junction, to realign again circumferentially towards the centre of the sinus. From here moving towards the bottom, the maximum principal direction increasingly follows the line of leaflet attachment and after transversing this area, again realigns with the circumferential direction. Minimum principal stresses and strains are orthogonal to the maximum principal direction. The apparent jump (e.g. on the outside view on the very left in Figure 4.3) in maximum principal strain at the line of leaflet attachment near the commissural heights might be misleading as these plots are planar projections of the aortic root. When looking at the figure, it must be kept in mind that at the location of the jump the structure extends into the paper, so that there is also a change in direction.

A look at the contour plots of maximum principal logarithmic strain in Figure 4.4 reveals a similar distribution both on the inside and outside of the aortic root and between the four valve models. Relatively low strains between 5%–10% are seen in the central part of the sinus, increasing towards the sinotubular junction as well as the leaflet attachment region, so that most of the root is strained above 15% with a maximum at the top of the sinotubular junction exceeding 30%. Minimum principal strains are largely negative except for the vicinity of the commissural heights on the outside and the central sinus-region on the inside of the root, illustrated in Figure 4.5. Minimum principal strains around the sinotubular junction indicate bending dominated deformation with strains of about -10% above and below the sinotubular junction on the outside and ∼ -19.5% at the sinotubular junction on the inside.

Stress contour plots of the aortic root in peak systole are presented in Figure 4.6 for maximum principals and in Figure 4.7 for minimum principals. Again, the distribution is consistent across the four models. On both sides, low maximum principal stresses are found in the sinuses, increasing towards the sinotubular junction and leaflet attachment site. There is a very localized stress concentration found both in minimum and maximum principal stress at the transition from leaflet attachment to sinotubular junction, where the peak values can be found. The bending region around the sinotubular junction is also reflected in the minimum principal stress distribution, with compressive stresses ∼ -40 kPa on the inside.

As the dilation of the aortic root decreases from peak to end systole, so do the values of stress and strain. The quality of the fields however does not change. As the pressure on the ventricular sides of the valve drop in diastole and it closes, the stress and strain fields change, predominantly in the lower half of the aortic root, especially below leaflet attachment. This is also where the first clear differences between the valve models manifest themselves, which can be observed in the vector plots in Figure 4.8. In the lower half of the aortic root the maximum principal direction looses its predominantly circumferential alignment and it does so in an inconsistent manner across the various valve models. Differences between the valve models are also evident in the contour plots of principal stress (Figure 4.11 and Figure 4.12) and strain (Figure 4.9 and Figure 4.10), where the roots of the two transversely isotropic models TILE and TIHYP show greater similarity than their isotropic counterparts.

Compared to the peak systolic results, their diastolic counterparts appear similar in quality, especially in the upper part of the aortic root. In case of minimum principals, this similarity mostly extends to the lower parts also. The values of maximum principals further reduce from the sinus region downwards in diastole. While the values of both stress and strain tend to be reduced in diastole as compared to peak systole in most regions of the aortic root, the ranges are increased in all instances. That means that peak values, that occur in the vicinity of the line of leaflet attachment, especially very localized at the top of the commissural heights, are increased in diastole. Therefore the diastolic root is exposed to increased gradients of stress and strain.

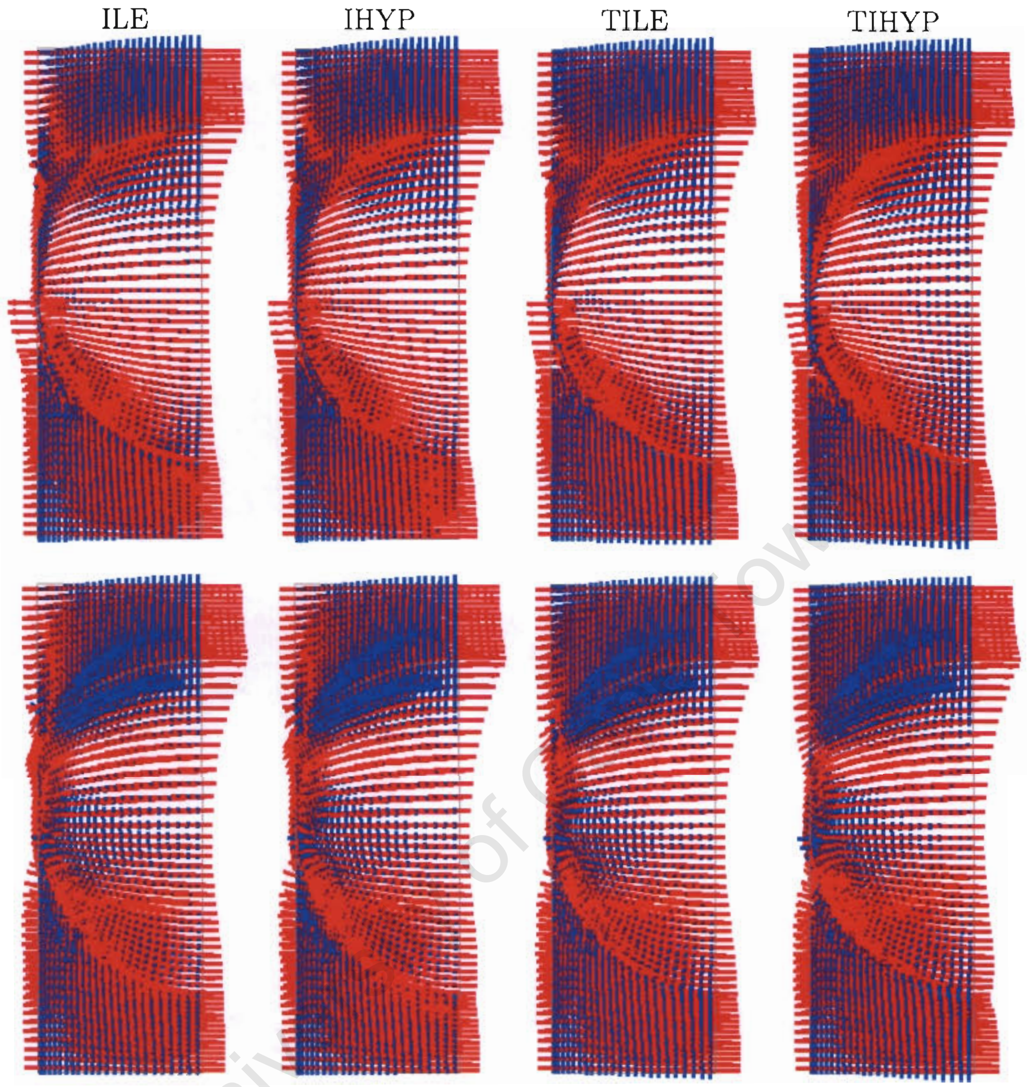

Figure 4.3: Vector plots of principal logarithmic strains in the aortic root (outside on top, inside on bottom) at peak systolic loading. Maximum principal strain is plotted in red, minimum principal in blue. As a result of the isotropy and linearity of the material model used for the root, vector plots of principal stresses are similar to the above.

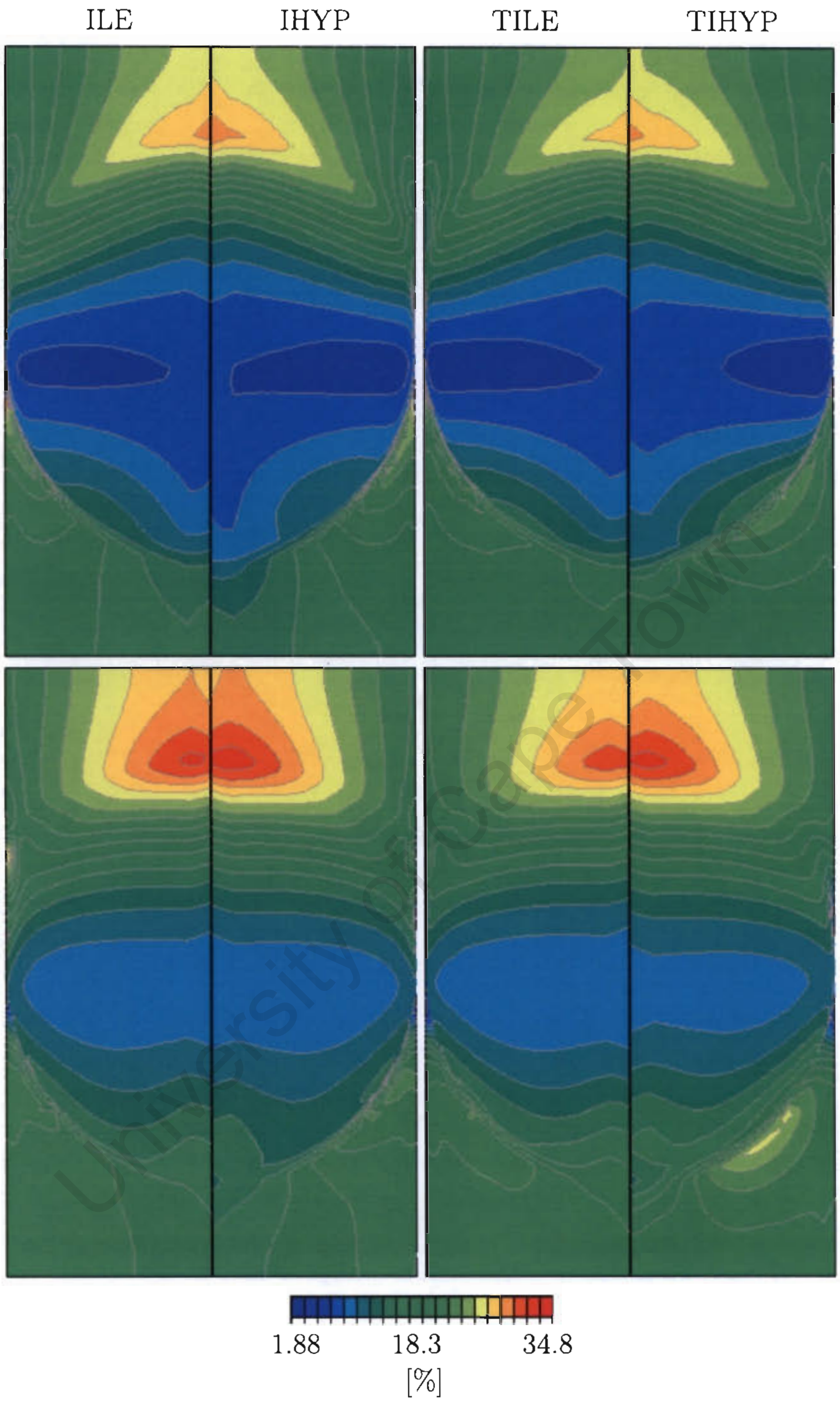

Figure 4.4: Maximum principal logarithmic strain in the aortic root (outside on top, inside on bottom) at peak systolic loading.

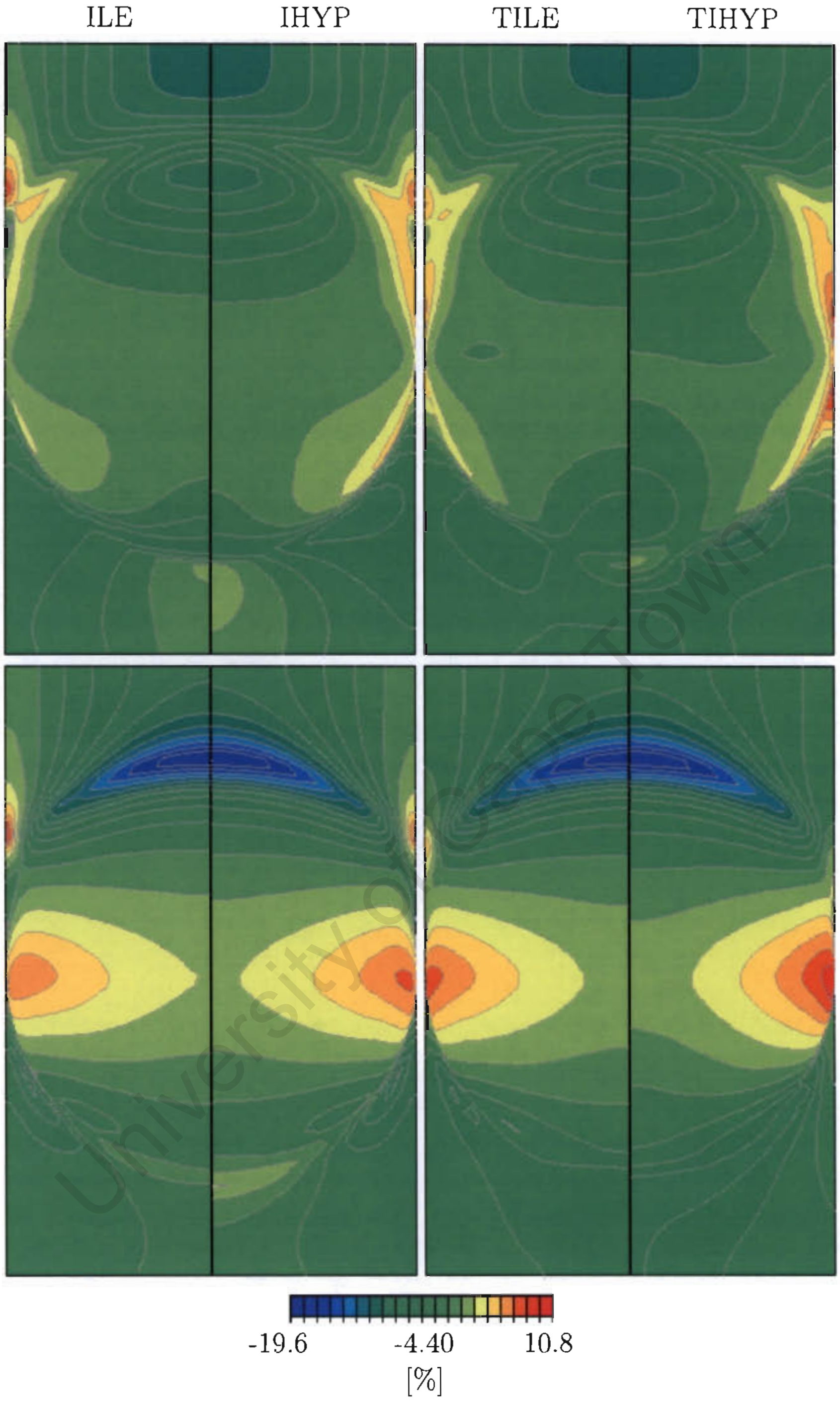

Figure 4.5: Minimum principal logarithmic strain in the aortic root (outside on top, inside on bottom) at peak systolic loading.

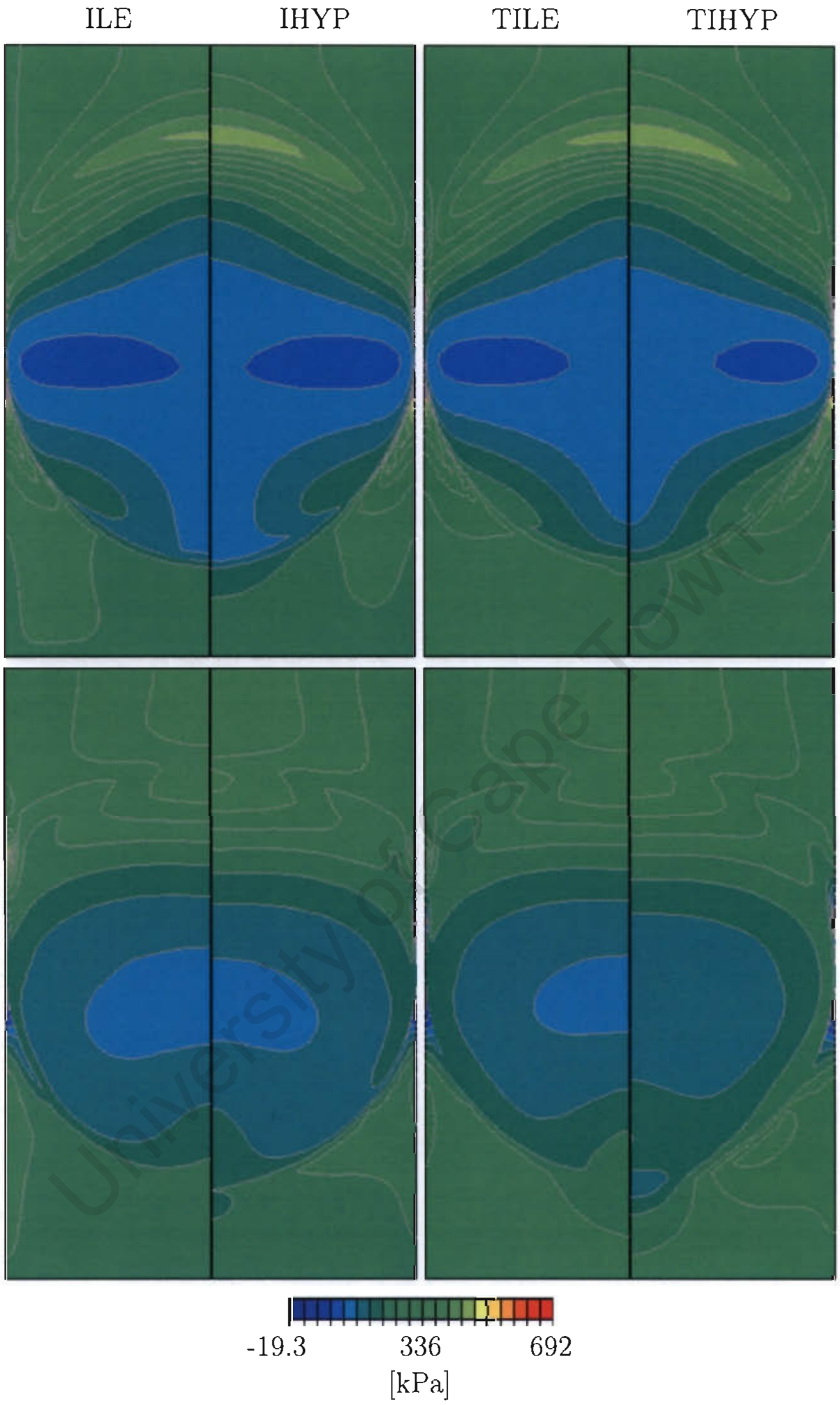

Figure 4.6: Maximum principal stress in the aortic root (outside on top, inside on bottom) at peak systolic loading.

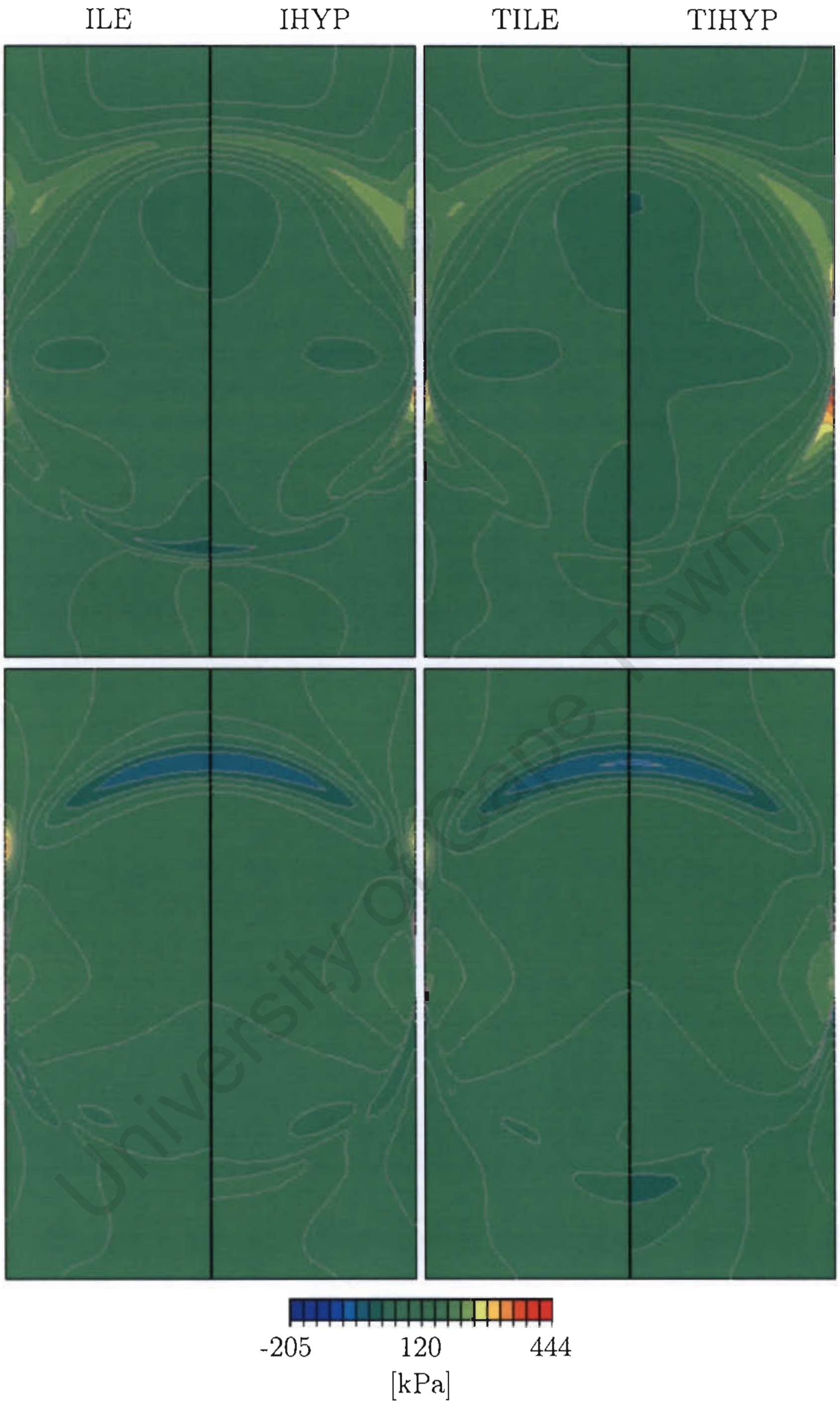

Figure 4.7: Minimum principal stress in the aortic root (outside on top, inside on bottom) at peak systolic loading.

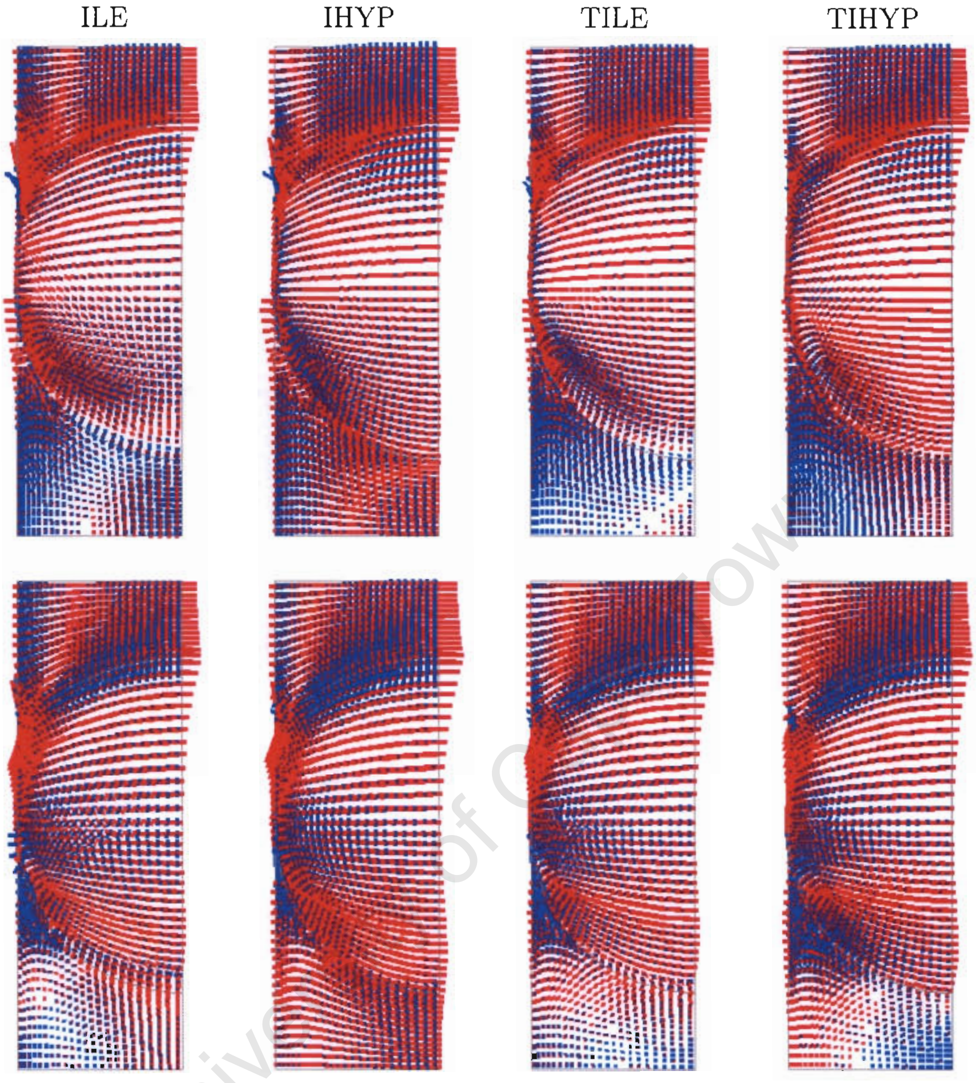

Figure 4.8: Vector plots of principal logarithmic strains in the aortic root (outside on top, inside on bottom) at diastolic loading. Maximum principal strain is plotted in red, minimum principal in blue. As a result of the isotropy and linearity of the material model used for the root, vector plots of principal stresses are similar to the above.

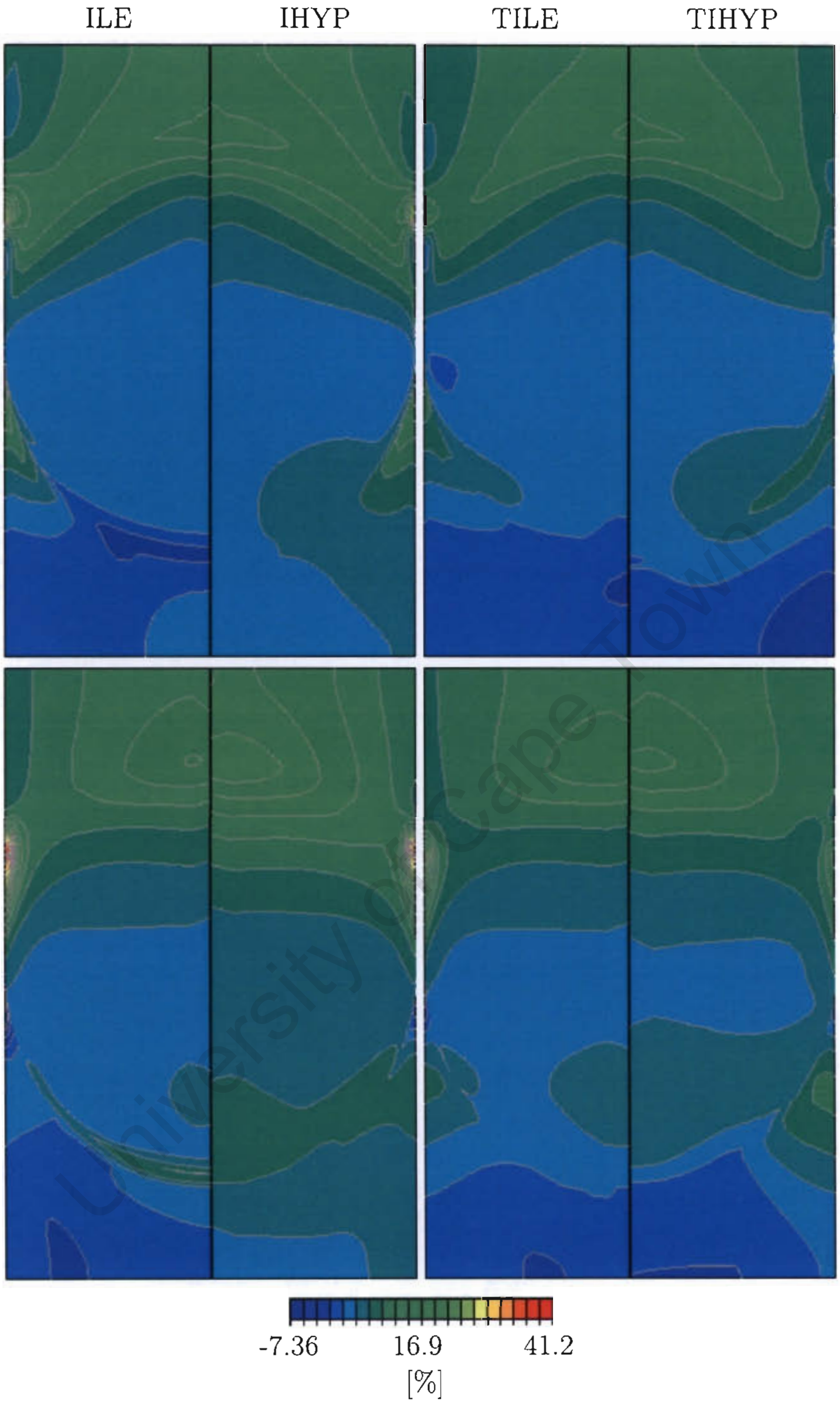

Figure 4.9: Maximum principal logarithmic strain in the aortic root (outside on top, inside on bottom) at diastolic loading.

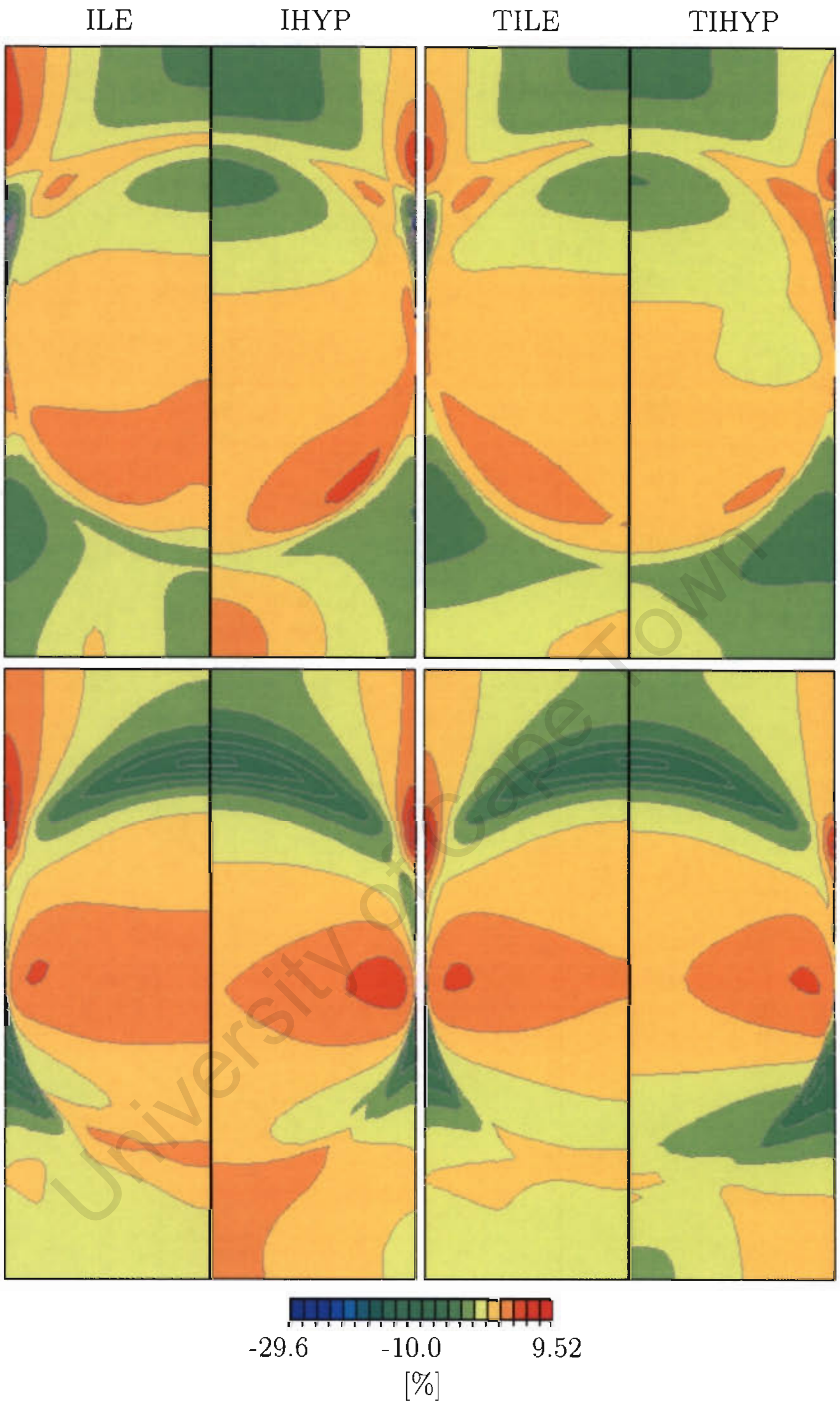

Figure 4.10: Minimum principal logarithmic strain in the aortic root (outside on top, inside on bottom) at diastolic loading.

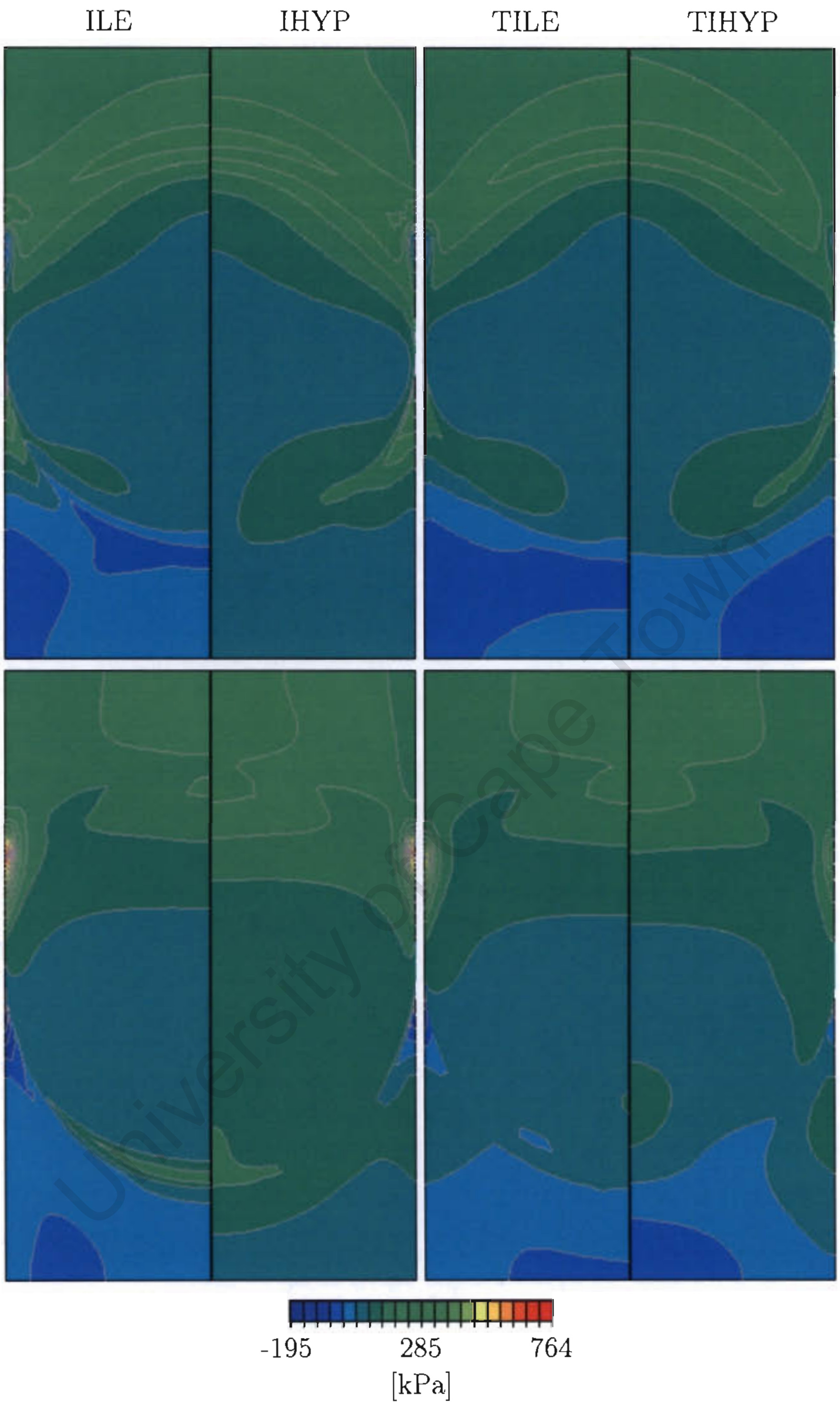

Figure 4.11: Maximum principal stress in the aortic root (outside on top, inside on bottom) at diastolic loading.

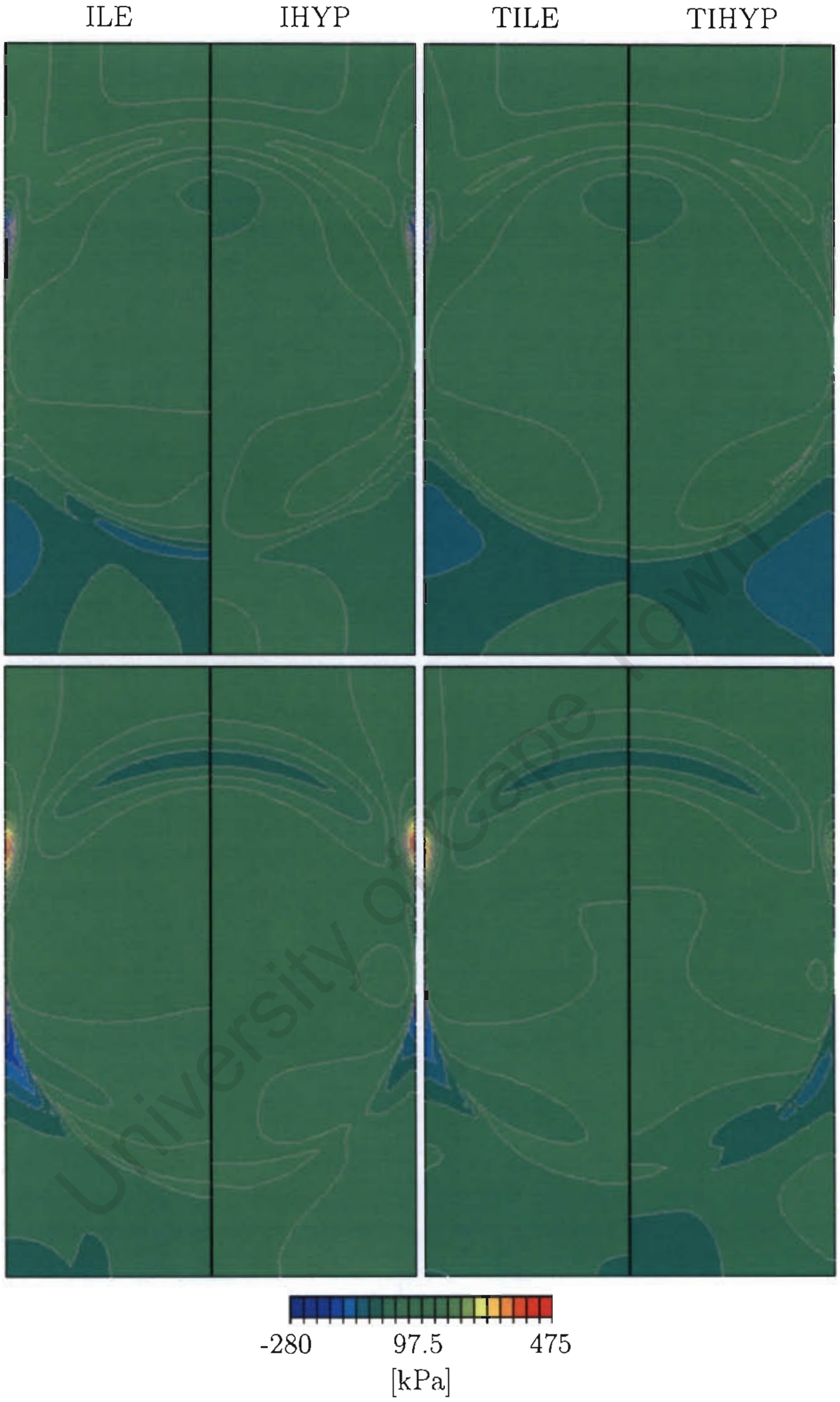

Figure 4.12: Minimum principal stress in the aortic root (outside on top, inside on bottom) at diastolic loading.

4.2.3 Isotropic Linear Elastic Valve

The isotropic linear elastic (ILE) valve in the peak systolic configuration at 120 mmHg internal pressure is shown in Figure 4.13. As the aortic root dilates as a result of this pressure, the attached leaflets become stretched circumferentially, forming a triangular orifice.

This deformation is reflected in the stress and strain fields of the leaflet. Maximum principal strains on both the aortic side and the ventricular side in Figure 4.21 away from the line of leaflet attachment are circumferentially aligned tensile strains. Approaching the commissural heights they become angled downwardly (i.e. as seen from left to right, the strain direction points downwards), and slightly upwardly on the lower parts of leaflet attachment on the aortic side. On the ventricular side there are large negative minimum principal strains along the line of leaflet attachment. The systolic ILE leaflets are therefore largely stretched circumferentially with a bending dominated area in the vicinity of the line of leaflet attachment.

Contour plots of maximum principal strain are shown in Figure 4.23 for the aortic and in Figure 4.27 for the ventricular leaflet side. The central top part of the leaflet, near the free edge, are hardly deformed with strains below 1% on both sides. On the aortic side strains increase towards leaflet attachment to strains of 15%–18% with a localized strain concentration of $\sim$ 33% at the top of the commissures. On the ventricular side strains increase along the free edge to reach a maximum of $\sim$ 17% near the commissures. They increase radially down up to $\sim$ 15% at the bottom of leaflet attachment. Along the commissural heights below the top, strains decrease down to a few per cent.

Minimum principal contours are depicted in Figure 4.24 and Figure 4.28 for the aortic and ventricular sides respectively. Apart from the site of leaflet attachment on the aortic side, they are all negative. Starting from the central free part of the leaflet, minimum principal strains are greater than -2%. On the ventricular side they decrease towards leaflet attachment down to -18%. On the aortic side they decrease along the free edge down to -11% at the commissures. From here, they increase along the annulus up to 6% at the bottom.

Since the ILE leaflet is isotropic the principal stress field (Figure 4.22) is

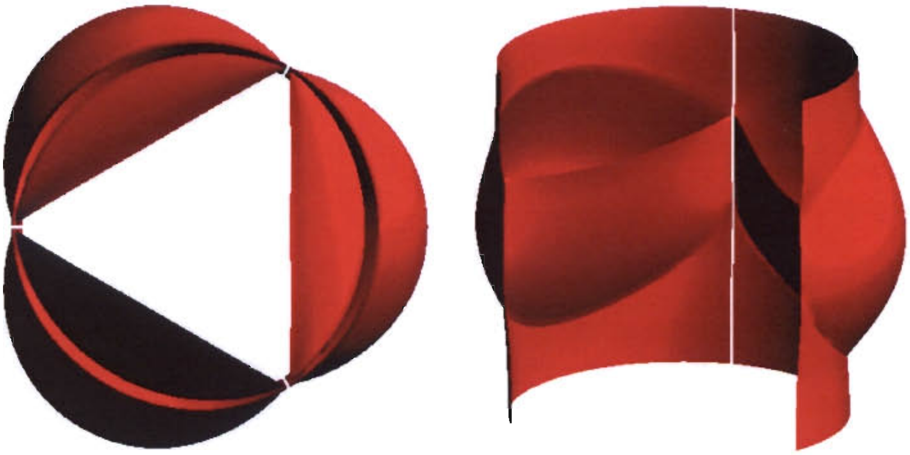

Figure 4.13: Valve with isotropic linear elastic leaflet in the systolic configuration, view from top on the left, side view on the right.

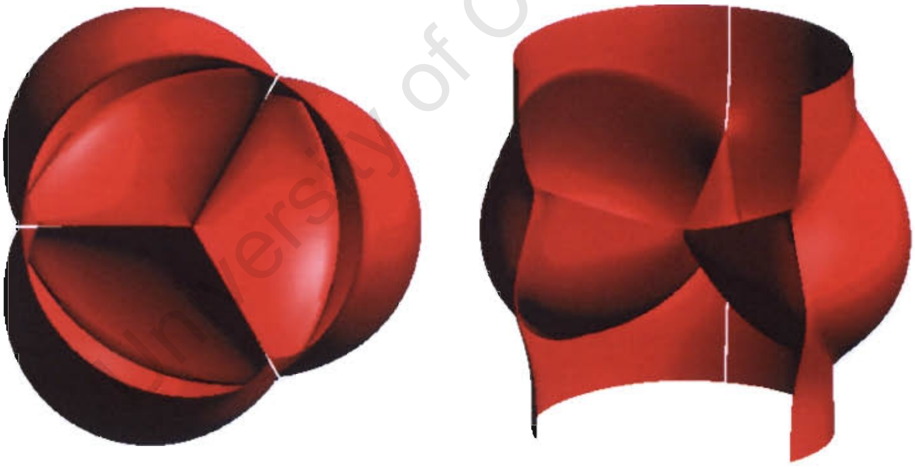

Figure 4.14: Valve with isotropic linear elastic leaflet in the diastolic configuration, view from top on the left, side view on the right.

collinear with the strain field. Contours of aortic maximum principal stresses are presented in Figure 4.25. The lowest, slightly negative stresses, occur at the top central part of the leaflet. They increase towards leaflet attachment in excess of 1.5 MPa with a stress concentration of 2.9 MPa at the top of the commissures. Ventricular maximum principal stresses are plotted in Figure 4.29. The top centre is stressed at $\sim$ 80 kPa. Stress increases radially down to reach a maximum of about 1.3 MPa in the lower leaflet belly, dropping again towards the attachment site. Along the free edge stress increases up to $\sim$ 1.2 MPa near the commissures and the drastically drops down to -220 kPa along the commissural heights.

Minimum principal stresses in the free part of the leaflet are similar on the aortic (Figure 4.26) and ventricular (Figure 4.30) side with stresses mostly below 100 kPa. Along the attachment site drastic differences between the two sides emerge, as the ventricular side is compressed down to -1.3 MPa at the top of the commissures, whereas the aortic side exhibits tensile stresses up to 1.3 MPa at the lower attachment.

As the internal pressure drops to 80 mmHg to mark end systolic loading, the stress and strain fields in the ILE leaflet only change quantitatively. Maximum principal strains drop by 40% on both leaflet sides, and maximum principal stresses drop by 33% on the ventricular, by 41% on the aortic side.

With the pressure on the ventricular sides of the valve model dropping to zero, the valve closes by deforming the leaflets towards the central axis of the valve and the region of the leaflets in contact with adjacent leaflets form the coaptation surface in diastole. The deformed diastolic ILE valve is depicted in Figure 4.14. The coaptation surface in this case is 24%, i.e. the ratio of undeformed leaflet area in contact under diastolic loading to total undeformed leaflet area, graphically represented in Figure 4.33. The closed ILE leaflets form a free edge angle of 23.2°, which is the angle formed by the tangent to the free edge from the top of the commissural heights and the horizontal plane through that point.

The diastolic stress and strain fields as shown in Figure 4.35 and Figure 4.34 divide the leaflet into four main areas: The line of leaflet attachment, the coaptation surface, the belly, and a transition area between the two latter. Perpendicular to the line of leaflet attachment, the deformation is bending dominated, where the highest stresses and strains occur, compressive in nature on the ventricular side, tensile on the aortic side. Maximum principal stresses and strains in the coaptation surface run diagonally, making a transition towards the circumferential leaflet direction in the area where the coaptation surface becomes the load-bearing belly of the leaflet. The deformation in these areas is membrane dominated and tensile in nature, although maximum principal stresses and strains are higher on the ventricular side. Minimum principal stresses are tensile on both side in the belly and compressive for most parts of both sides in the coaptation area. In the transition area minimum principal stresses on the aortic side are compressive accounting for bending that has to occur in that area.

Maximum principal stresses and strains of the aortic ILE leaflet in diastole can be found in Figure 4.38 and Figure 4.36. The free part of the leaflet is exposed to strains less than 10% with a rapid gradient towards leaflet attachment with strains ∼ 20% and a localized maximum at the top of the commissures of 51.5%. Similarly, the lowest stresses down to -786 kPa occur in the leaflet centre around the free edge, increasing in the rest of the free leaflet to no more than 500 kPa. From here, stresses are increasing towards the leaflet attachment site ranging from 1.8 MPa at the bottom to a maximum of 4.4 MPa at the top of the commissural heights.

On the ventricular side maximum principal strains in Figure 4.40 in the free part are less than 10%. Highest values up to 26.5% are found towards the top of the commissures, but they quickly drop along the attachment line down to -3% where it starts to curve. Large parts of the ventricular leaflet have maximum principal stresses below 800 kPa, shown in Figure 4.42. Along the line of attachment they decrease below -1.0 MPa except in the neighbourhood of the commissural heights, where both positive values up to 2.0 MPa and negative values ∼ -1.0 MPa can be found.

Minimum principal strains on the aortic side decrease from ∼ 1% in the belly to ∼ -20% around the central free edge and to a minimum of -26.8% at the top of the commissures, revealed by a look at Figure 4.37. On the ventricular side (Figure 4.41) they reach values up to 3.4% in the belly, decreasing to ∼ -5% in the rest of the free part, and rapidly dropping towards leaflet attachment down to a minimum of -38% around the commissures.

Minimum principal stresses in the leaflet belly are $\sim$ 250 kPa on the aortic (Figure 4.39) and $\sim$ 500 kPa on the ventricular side (Figure 4.43). On the aortic side they have their minimum in the central free edge region of -1.7 MPa, and reach values up to 1.9 MPa along the attachment. In this bending region they drop down to -2.8 MPa on the ventricular side.

4.2.4 Isotropic Hyperelastic Valve

Under peak systolic loading, the isotropic hyperelastic (IHYP) leaflets attached to the dilated root stretch to form a triangular orifice as illustrated in Figure 4.15. The collinear stress and strain fields in Figure 4.21 and Figure 4.22 on both leaflet sides show predominantly circumferentially aligned maximum principals. At the annulus however they emanate pointing downward as seen from left to right. It is also at this site on the ventricular leaflet side, that minimum principal stresses and strains are very pronounced with negative values, indicating bending behaviour.

The largest maximum principal strains on the aortic leaflet side occur along the line of leaflet attachment with values slightly in excess of 10% strain and a maximum of 3.8 MPa stress, presented in the contour plots in Figure 4.23 and Figure 4.25. From the leaflet attachment strain is slowly decreasing to $\sim$ 5% towards the top central part near the free edge of the leaflet. Similarly, but more rapidly, the stresses drop to less than 200 kPa. Maximum principal stresses and strains on the ventricular side are similar, except for lower values in the vicinity of the commissural heights and a lower peak stress value of 2.3 MPa, as can be seen in Figure 4.27 for the strains and Figure 4.29 for the stresses.

On the ventricular side, minimum principal stresses (Figure 4.30) and strains (Figure 4.28) have their maxima in the lower leaflet belly along the symmetry line, around -1% strain and 470 kPa. From there values decrease towards the leaflet annulus, down to -8.5% strain at the commissural heights and down to a band of compressive stresses with minimum of -320 kPa. Minimum principal strains in the aortic leaflet belly are $\sim$ -2%, decreasing towards the free edge to -6% near the commissures, but increase towards the lower parts of the attachment line up to 0.5%. Corresponding stresses are below 100 kPa in most part of the aortic leaflet

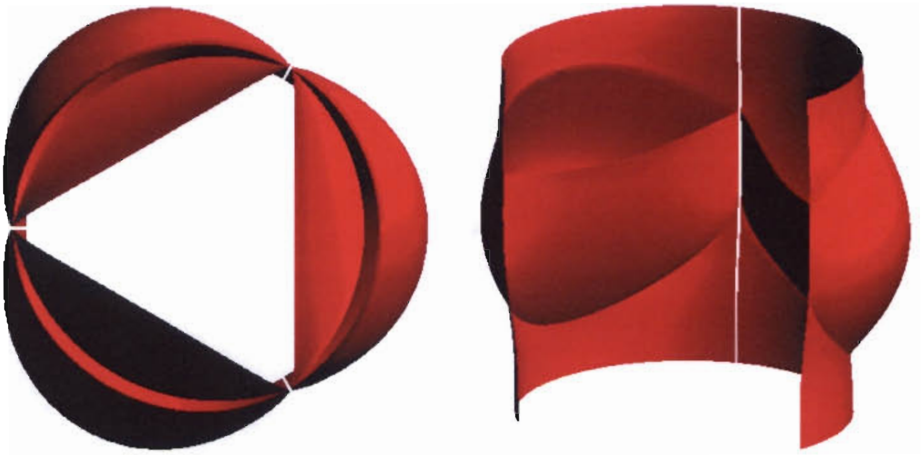

Figure 4.15: Valve with isotropic hyperelastic leaflet in the systolic configuration, view from top on the left, side view on the right.

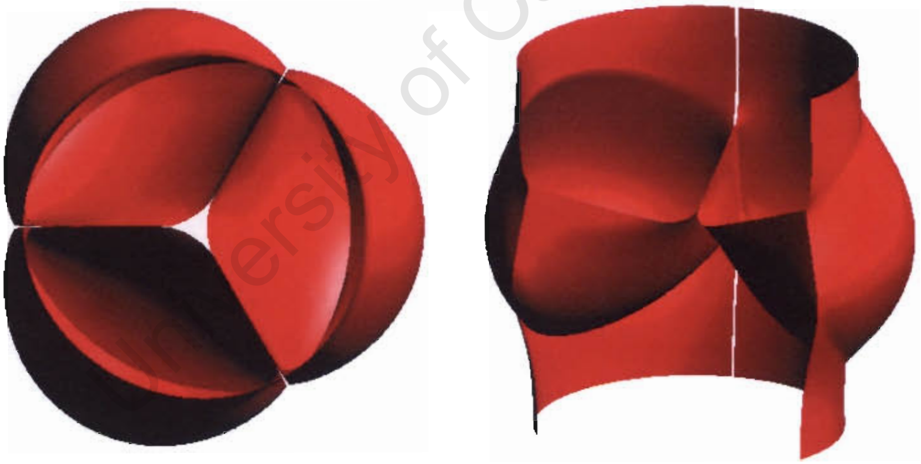

Figure 4.16: Valve with isotropic hyperelastic leaflet in the diastolic configuration, view from top on the left, side view on the right.

side, increasing towards the line of attachment with a maximum of 1.4 MPa in the lower part. Aortic minimum principals are presented in the contour plots of Figure 4.26 and Figure 4.24.

It was mentioned earlier that it was not feasible to simulate the pressure drop from peak to end systolic loading in the IHYP case. Instead the state of deformation at 80 mmHg internal pressure, that was part of the peak systolic solution, was used as a starting point for diastolic loading. In terms of orientations of principal stresses and strains and the relative distribution of values, there is little difference between 120 mmHg and 80 mmHg internal pressure. Peak values in maximum principal stress are reduced by 37% on both sides, corresponding strains decrease by 28% on the aortic and by 39% on the ventricular side.

The closed IHYP valve under diastolic loading is shown in Figure 4.16. In this case the coaptation surface only forms 15% of the undeformed leaflet area (Figure 4.33) and the free edge angle is 20.6°.

The diastolic maximum principals in Figure 4.34 and Figure 4.35 predominantly align with the circumferential leaflet direction except in the coaptation area, where they run diagonally. On both leaflet sides they are entirely tensile. Maximum bending, evident in the minimum principals, occurs in two areas: Along the commissural lines the ventricular side is compressed while the aortic side is in tension; and in the coaptation area extended along the free edge the reverse is true.

Maximum principal strains in the IHYP leaflet range between 6% and 8% in the central region of the aortic side, depicted in Figure 4.36. They are increasing towards the line of leaflet attachment approaching 12.6% in the commissural heights. On the ventricular side (Figure 4.40) the highest values up to 11.6% occur in the central transition region and at the top of the commissures, decreasing to a minimum of 5.4% in the lower attachment area.

Corresponding maximum principal stresses are below 300 kPa in the large central part of the aortic leaflet side, rising towards the leaflet annulus between 1.1 MPa up to 5.9 MPa at the top, as illustrated in Figure 4.38. On the ventricular side in Figure 4.42 highest stresses up to 2.0 MPa are found in the belly. Apart from a high stress concentration at the top of the commissural heights, the leaflet attachment region is exposed to stresses below 400 kPa, decreasing down to 29 kPa in the lower parts.

Minimum principal strains on the diastolic aortic leaflet side (Figure 4.37) are negative down to -7.7% in the coaptation surface, and increase up to 5.9% in lower leaflet parts. Consequently, there are compressive minimum principal stresses in the coaptive aortic parts with a minimum of -399 kPa at the free edge. These values increase towards lower leaflet parts up to 1.9 MPa, plotted in Figure 4.39.

On the ventricular side, minimum principal strains reach 3.6% in lower central parts, dropping to less than ~ -5% in coapting parts with a minimum of -11% just below the top of the commissures (Figure 4.41). Similarly, the minimum principal stresses decrease from 1.1 MPa in the belly down to -786 kPa below the top of the commissures (Figure 4.43).

4.2.5 Transversely Isotropic Linear Elastic Valve

The valve with transversely isotropic linear elastic (TILE) leaflet in peak systolic configuration with the leaflets forming a triangular outlet is pictured in Figure 4.17. Consequently, in the belly and central parts of the leaflet, maximum principal strains are circumferentially aligned as shown in Figure 4.21 for both the aortic and ventricular side. Towards the line of leaflet attachment they run diagonally down from left to right on both sides. On the aortic side they emanate close to normal to the attachment line. On the ventricular side there are pronounced negative minimum principal strains, indicating the presence of bending along the annulus. Due to anisotropy of the TILE leaflet principal stresses are no longer aligned with the principal strains. As a result of the higher stiffness in the circumferential direction, maximum principal stresses are predominantly oriented circumferentially, evident in Figure 4.22.

Contour plots of maximum principal strains are in Figure 4.23 for the aortic and in Figure 4.27 for the ventricular leaflet side. In both cases, minima are found in the top central region between 2%–4%. From there strains increase towards the leaflet attachment. On the aortic side there are strains of ~ 20% at that site with a maximum on top of the commissures of 30%. On the ventricular side strains increase to 16% at the top of the commissures and the lower parts of the annulus.

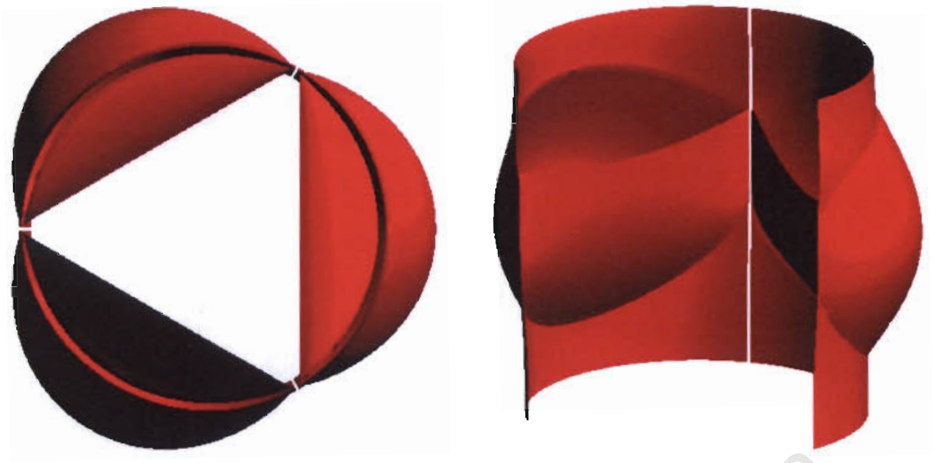

Figure 4.17: Valve with transversely isotropic linear elastic leaflet in the systolic configuration, view from top on the left, side view on the right.

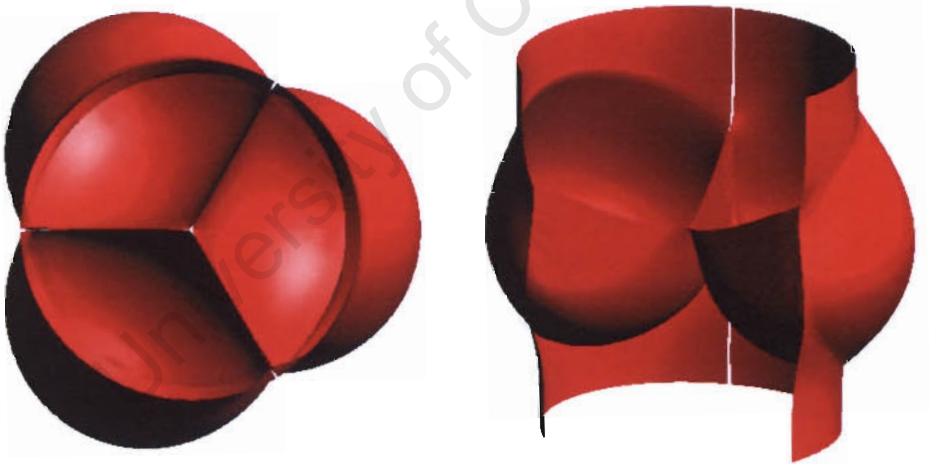

Figure 4.18: Valve with transversely isotropic linear elastic leaflet in the diastolic configuration, view from top on the left, side view on the right.

Between these two areas strain decreases along the line of attachment down to 6%. Minimum principal strains in Figure 4.24 and Figure 4.28 in the lower belly are between 1%–8% on the aortic side and between 8%–10% on the ventricular side. On the latter they decrease towards leaflet attachment down to -22% at the commissural heights. On the aortic side they increase to 15% in the lower parts of leaflet attachment and decrease to -15% at the top of the commissures.

The central part of the leaflet near the free edge is under tensile stress not in excess of 450 kPa, as can be seen in Figure 4.25 and Figure 4.29. This is the area of lowest maximum principal stress on the aortic side. From there these increase towards the leaflet attachment with a stress concentration at the top of the commissures at 1.9 MPa. On the ventricular side maximum principal stresses increase along the symmetry line to 1.2 MPa in the lower belly. From there they decrease along the line of leaflet attachment to a minimum of -50 kPa at the commissures. Minimum principal stresses in the upper central part of the leaflet are less than 65 kPa on the aortic side in Figure 4.26. From there they increase towards the annulus up to 460 kPa in the lower parts. In the belly minimum principal stresses on the ventricular side are $\sim$ 300 kPa in Figure 4.30, decreasing from there to a compressive band along the leaflet attachment with stresses as low as -800 kPa.

During end systolic loading, the quality of deformation is similar to what was discussed above. Values of stress and strain change, e.g. peak values of maximum principal stresses decrease by 35% on both side of the leaflet, maximum principal strains reduce by 34% on the ventricular side and by 41% on the aortic side.

The diastolic TILE leaflets close under a free edge angle of 25.4° and the coaptation surface is formed by 36% of undeformed leaflet area in Figure 4.33. A view of the deformed model is pictured in Figure 4.18.

The diastolic strain fields of the TILE leaflet in Figure 4.34 clearly show four main areas. There are large compressive strains along the line of leaflet attachment, especially on the ventricular side. Deformation in that area is bending dominated. In the coaptation area maximum principal strains run diagonally, on both sides in line with maximum principal stresses. It is the latter that in the transition area – line up with the circumferential leaflet direction in the belly, although produced by the minimum principal strains as a look at Figure 4.35 reveals and which is a result of anisotropy. The maximum principal strains in the leaflet belly align with the radial leaflet direction. Minimum principal stresses on the aortic side of the coaptation area are largely compressive accounting for bending in that area.

Maximum principal strains (Figure 4.36) in the leaflet belly on the aortic side are ~ 15% and between 13% and 21% in the coaptation surface. Minimum values of -1.7% can be found in the central free edge region, while the highest strains in excess of 20% are found along leaflet attachment with a localized maximum of 56.7% at the top of the commissural heights. Similarly, maximum principal strains on the ventricular side (Figure 4.40) are ~ 15% in the belly and up to 23% in the coaptation surface. The maximum value of 35% is located at the top of the commissures, but they decrease to a few per cent at the bottom of leaflet attachment.

Maximum principal stresses on the aortic side (Figure 4.38) are less than 500 kPa in belly and coaptation with a minimum of -55 kPa around the central free edge. Highest stresses occur along leaflet attachment from ~ 600 kPa up to 2.8 MPa at the top of commissural heights. They are mostly negative in that area on the ventricular side (Figure 4.42), with a minimum of -471 kPa just below the commissural heights, rising below 400 kPa at their top. The ventricular belly is stressed ~ 600 kPa and the maximum of 1.2 MPa can be found near the central free edge.

On the aortic side, minimum principal strains (Figure 4.37) range from negative values in the upper parts down to -18% with a localized minimum of -37% at the commissures up to 8.8% in the lower leaflet parts. On the ventricular side (Figure 4.41), they range from a minimum of -54.7% localized below the commissural heights, increasing in upper parts to -17%, up to 7.8% in the leaflet belly.

Minimum principal stresses on the aortic side (Figure 4.39) are between -150 kPa and 150 kPa in the upper leaflet with a minimum of -527 kPa at the centre of the free edge. They increase towards lower leaflet parts around 250 kPa up to 727 kPa in the attachment region. On the ventricular side (Figure 4.43), they reach 380 kPa in the belly, to decrease to become slightly negative in coaptive parts. The leaflet attachment area on that side is compressed down to -1.7 MPa at the commissural heights.

4.2.6 Transversely Isotropic Hyperelastic Valve

The triangular orifice formed by the transversely isotropic hyperelastic (TIHYP) leaflets of the valve under peak systolic pressure can be seen in Figure 4.19. The strain fields of the isotropic matrix are shown in Figure 4.21. On both sides the upper central part of the leaflets exhibit circumferentially aligned maximum principal strains. Towards the commissural height they are oriented pointing downward from left to right. Finally in the lower part of the leaflet, maximum and minimum principals switch roles, so that the maximum principals are now radially aligned. Of special note are the negative minimum principal strains along the commissural heights of the ventricular side, leading to bending along the leaflet attachment.

Contour plots of principal strains in the isotropic matrix are presented in Figure 4.23 and Figure 4.24 for the aortic and in Figure 4.27 and Figure 4.28 for the ventricular side. In the former maximum principal strains in the upper central leaflet region are ~ 9%. From there they increase towards the line of leaflet attachment up to ~ 30% at the commissural heights. In the lower leaflet belly minimum principal strains on the aortic side are around 10% increasing towards the lower leaflet attachment to 16%, decreasing down to -10% near the commissures at the free edge. Maximum principal strains in the lower leaflet belly on the ventricular side are in excess of 22%, but apart from a localized maximum near the commissures, drop to 10% in the central upper part, and as low as 4% at the commissural heights. The highest minimum principal strains on that side occur in the lower leaflet belly at 13%, decreasing from there to negative values, with a minimum of -25% below the commissural heights.

Principal stresses (Figure 4.22) presented in Figure 4.25 (max. aortic), Figure 4.26 (min. aortic), Figure 4.29 (max. ventricular) and Figure 4.30 (min. ventricular), are collinear with the strain fields described above, since these figures represent the stresses in the isotropic matrix. Reinforcement stresses and strains are reported separately below. Both maximum and minimum principal stresses in the aortic side are below 30 kPa away from the leaflet attachment, where both increase rapidly. The largest maximum principal stress of 350 kPa and largest minimum principal stress of 210 kPa occur in the lower part of the leaflet attachment. The largest maximum principal stress of 170 kPa and largest minimum principal stress

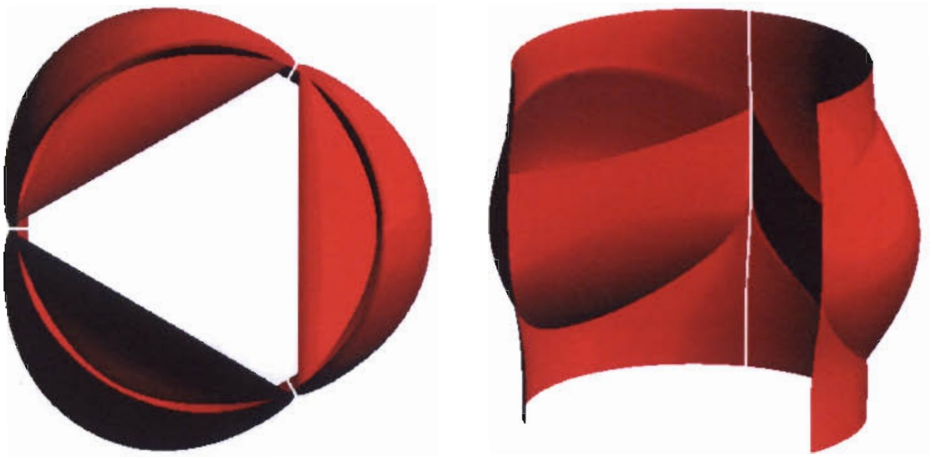

Figure 4.19: Valve with transversely isotropic hyperelastic leaflet in the systolic configuration, view from top on the left, side view on the right.

Figure 4.20: Valve with transversely isotropic hyperelastic leaflet in the diastolic configuration, view from top on the left, side view on the right.

of 120 kPa in the ventricular leaflet side are present in the lower leaflet belly. From there both drop, so that large parts of the leaflet are stressed below 40 kPa. Compressive stresses of down to -40 kPa are present along the commissural heights.

In addition to stress and strain fields of the isotropic matrix, the reinforcement stresses and strains of the TIHYP leaflet have to be considered, accounting for anisotropy. Both are aligned circumferentially during systolic loading as can be seen in Figure 4.31. Maximum fibre strain of ~ 12% occurs in the lower leaflet decreasing towards the top to ~ 9%, contour plotted in the same figure. Corresponding stresses range from 100 kPa to 2.2 MPa.

As a result of the pressure drop to the end systolic value maximum stresses and strains in the TIHYP leaflet decrease. Additionally, the stress and strain fields change in the lower leaflet part in that maximum principals are now also aligned circumferentially as in the other models. Stress and strain orientation now resembles the TILE scenario in Figure 4.21. While maximum principal stresses in the isotropic matrix decrease by 61% and 63% on the ventricular and aortic side respectively, associated strains are only reduced by 15% on the ventricular and by 36% on the aortic side. Peak values of stress and strain in the fibre reinforcement drop by 46%.

Under diastolic loading the TIHYP valve, represented in Figure 4.20, is closed with a coaptation surface of 45% of undeformed leaflet area (Figure 4.33). The free edge angle in this case is 23.5°.

The different regions of the leaflet and the role they play in the diastolic configuration are very prominently reflected in the matrix strain field of the TIHYP model as illustrated in Figure 4.34. Maximum principal strains and stresses of the matrix emanate oriented diagonally downward from the commissural heights and free edge to become increasingly aligned with the radial leaflet direction through the coaptation area. In the leaflet belly they run radially. They are of tensile nature throughout. The minimum principal stress and strain direction is positively angled from the positive horizontal throughout the commissural and coaptational areas where both leaflet sides are contracted. Minimum principals vanish through the transition area and become tensile in circumferential direction in the belly.

Large parts of the leaflet belly and coaptive region experience maximum principal strains between 25% and 30% on both the aortic (Figure 4.36) and ventricular (Figure 4.40) side. They decrease to 11% in the central free edge on the latter and have a minimum of 6.3% there on the former. While the aortic leaflet attachment is strained above 30% reaching 38.4% at the commissures, ventricular values range from 6% at the bottom to 22% at the top with a small localized region of negative strains to -4.2% below the commissural heights.

On the ventricular side (Figure 4.42), the highest maximum principal matrix stresses of 354 kPa are located in the belly, decreasing throughout the rest of the leaflet with a small region of compressive stress -152 kPa below the commissural heights. On the aortic side (Figure 4.38), they reach 280 kPa in the belly, decreasing to below 50 kPa in the rest of the leaflet, apart from the line of attachment, where they range from 300 kPa up to 1.1 MPa in the lower parts.

Minimum principal strains on the aortic side (Figure 4.37) start at -26.5% at the top of commissural heights, stay negative in the coaptation surface, but increase up to ~ 10% in the belly. Their stress counterparts (Figure 4.39) range from compressive values of -44 kPa in coaptation and commissural heights to ~ 150 kPa in the belly up to 445 kPa in the lower attachment.

Similarly, minimum principal strains on the ventricular side (Figure 4.41) are negative in attachment and coaptation regions with a minimum of -39.6% below the commissural heights and climb to 12.5% in the leaflet belly. Slight compressive minimum principal matrix stresses (Figure 4.43) of less then -50 kPa in the coaptation surface further drop in the annulus with a localized minimum of -261 kPa below the commissural heights. Highest values up to 220 kPa occur in the leaflet belly.

Again, stresses and strains of the reinforcement in Figure 4.32 are superimposed on the matrix discussed above. From the vector plot, a circumferential alignment is evident. Reinforcement strains range from 8.74% below the commissural heights to 11.7% in the lower leaflet attachment. Corresponding stresses start from ~ 100 kPa in the upper leaflet to reach a maximum of 2.16 MPa in the lower annulus.

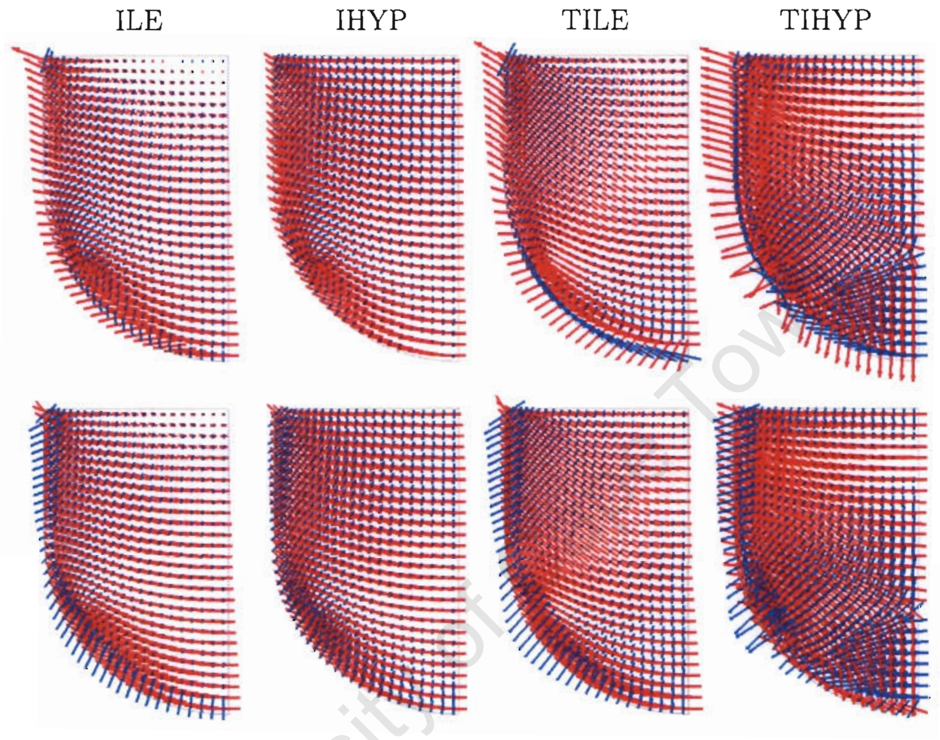

Figure 4.21: Vector plots of principal logarithmic strain in the leaflets at peak systolic loading. Maximum principal strains are plotted red, minimum principal strains blue. The aortic leaflet side is plotted on top, the ventricular on the bottom.

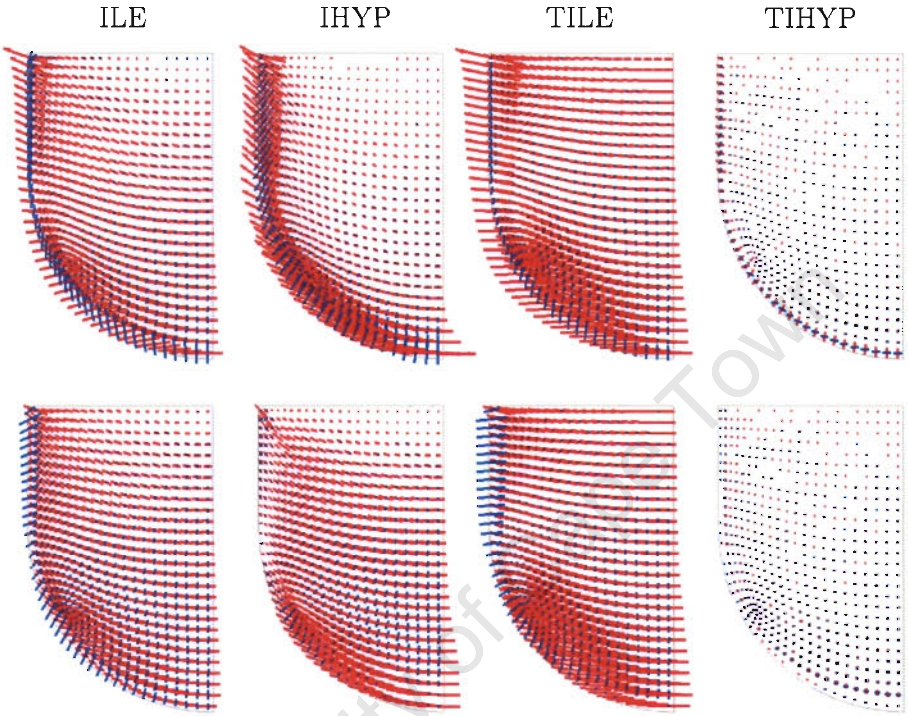

Figure 4.22: Vector plots of principal stresses in the leaflets at peak systolic loading. Maximum principals are plotted red, minimum principal stresses blue. The aortic leaflet side is plotted on top, the ventricular on the bottom.

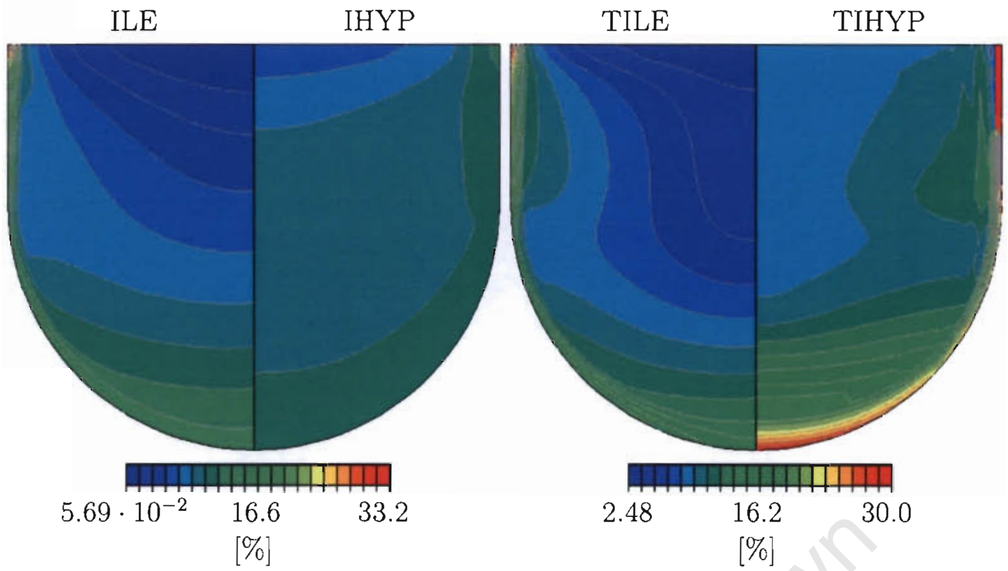

Figure 4.23: Maximum principal strain on the aortic sides of the leaflets at peak systolic loading.

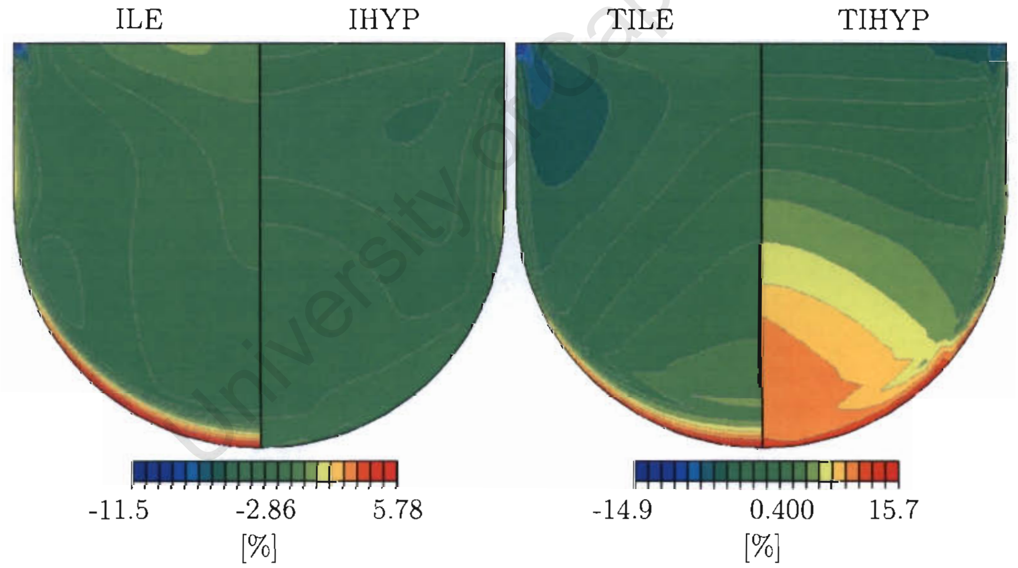

Figure 4.24: Minimum principal strain on the aortic sides of the leaflets at peak systolic loading.

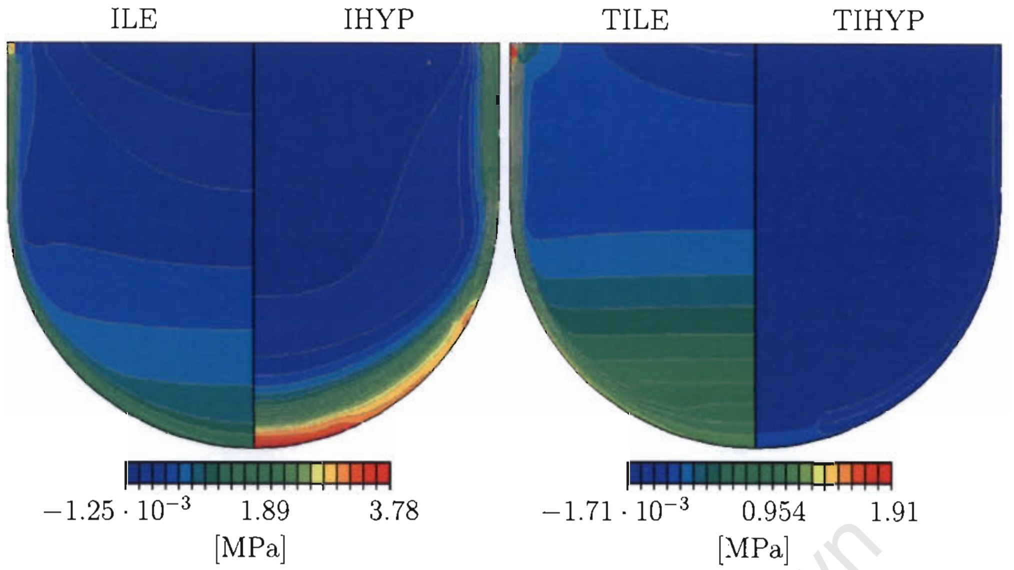

Figure 4.25: Maximum principal stress on the aortic sides of the leaflets at peak systolic loading.

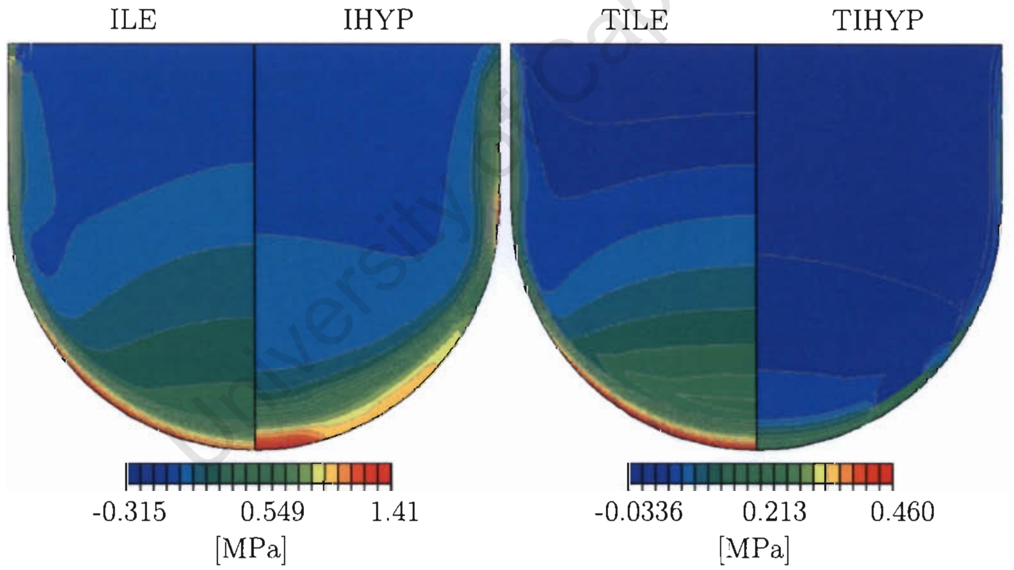

Figure 4.26: Minimum principal stress on the aortic sides of the leaflets at peak systolic loading.

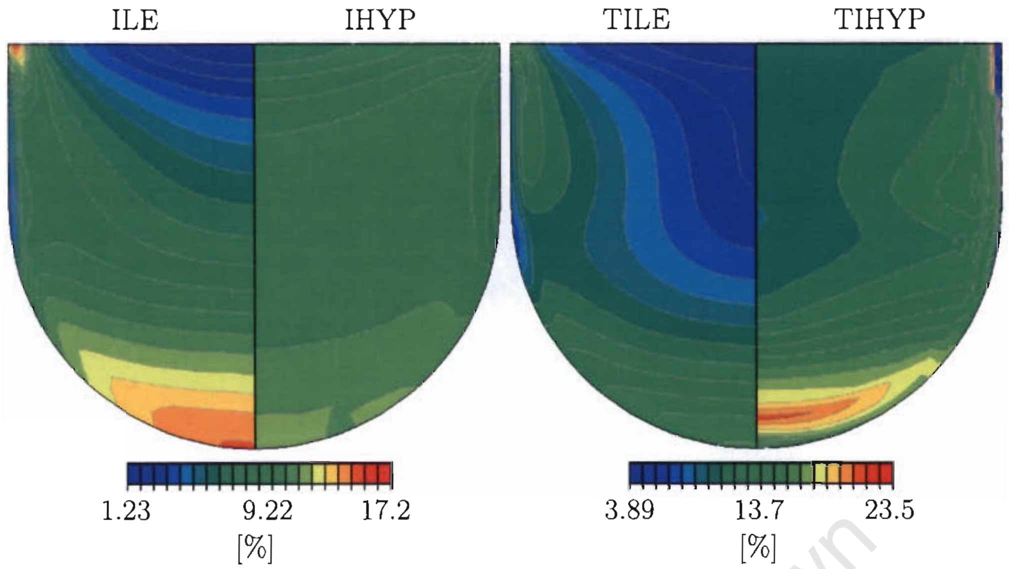

Figure 4.27: Maximum principal strain on the ventricular sides of the leaflets at peak systolic loading.

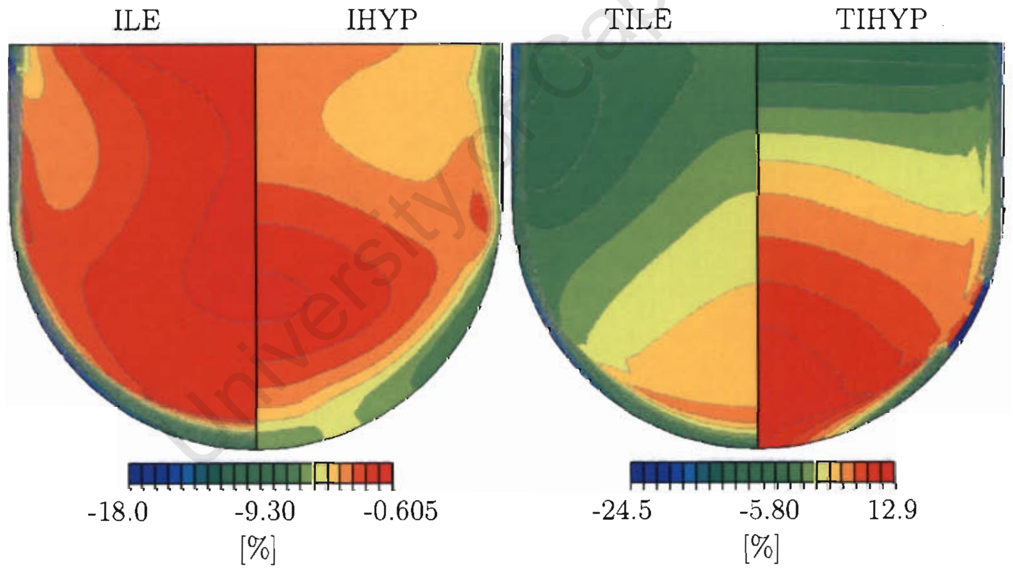

Figure 4.28: Minimum principal strain on the ventricular sides of the leaflets at peak systolic loading.

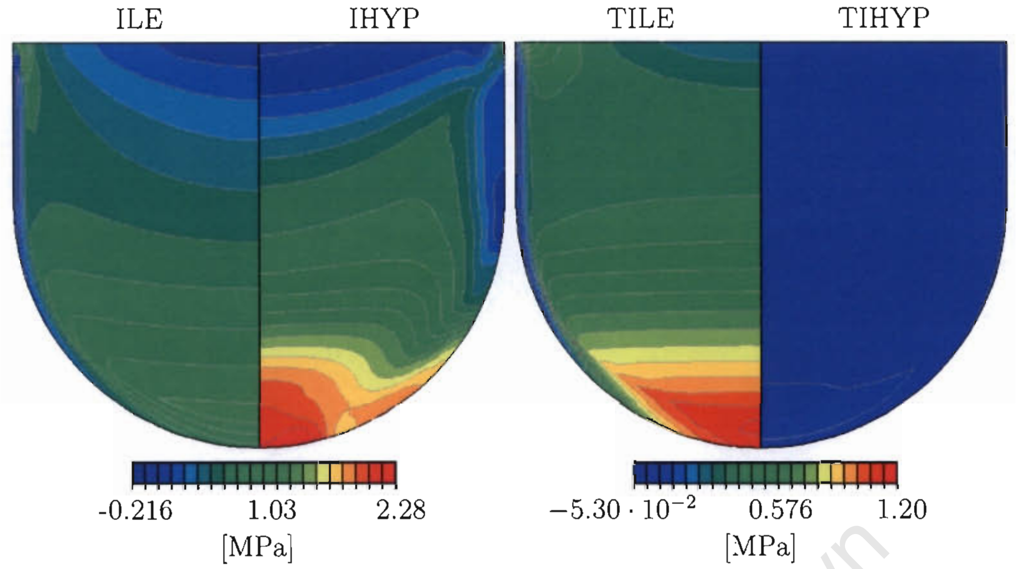

Figure 4.29: Maximum principal stress on the ventricular sides of the leaflets at peak systolic loading.

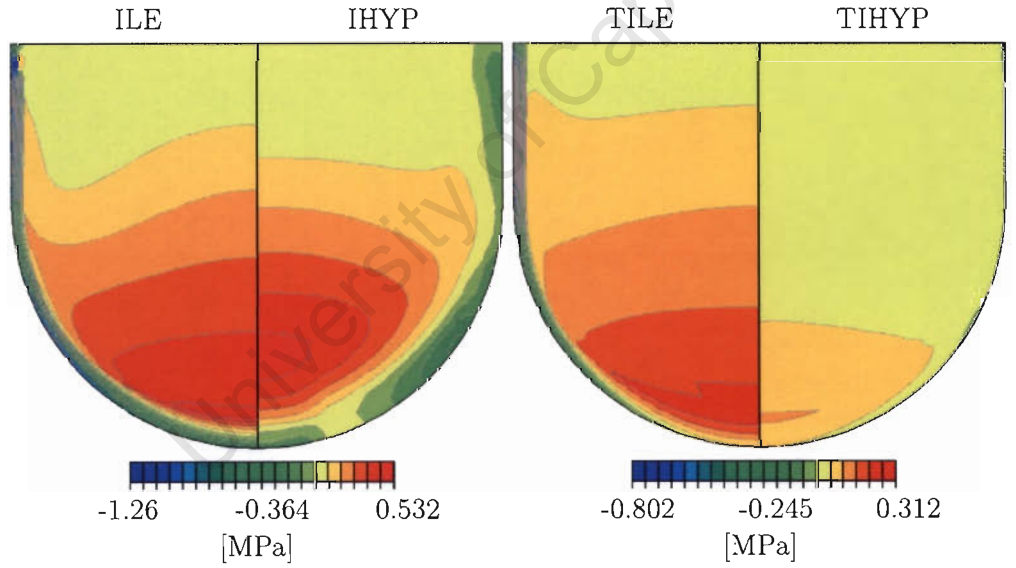

Figure 4.30: Minimum principal stress on the ventricular sides of the leaflets at peak systolic loading.

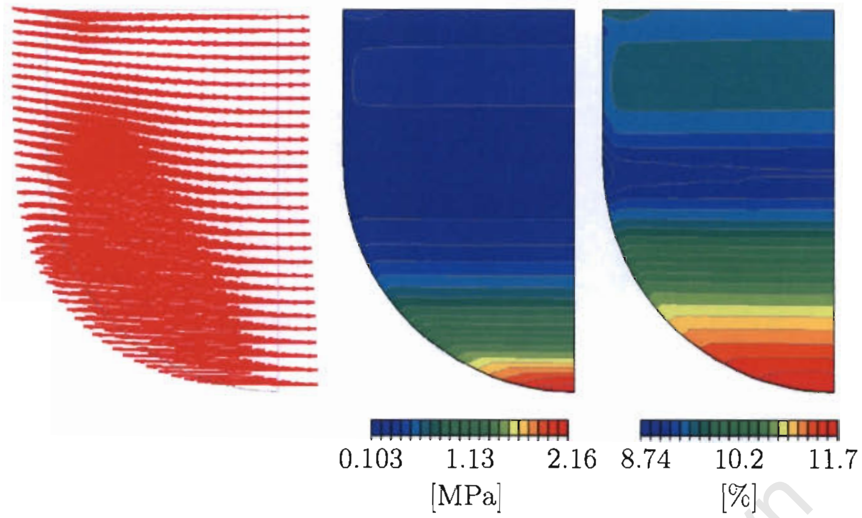

Figure 4.31: From left to right, vector plot of the deformed fibre direction **a**, fibre stress and logarithmic fibre strain of the TIHYP model at peak systolic loading.

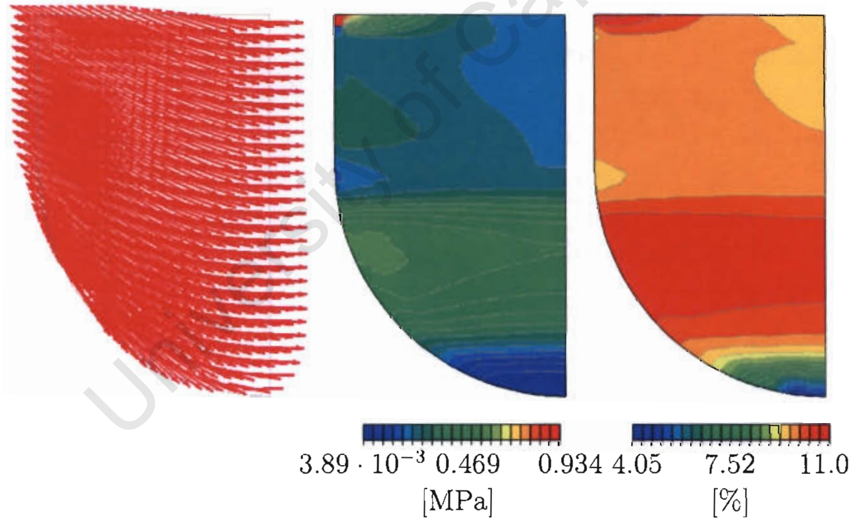

Figure 4.32: From left to right, vector plot of the deformed fibre direction **a**, fibre stress and logarithmic fibre strain of the TIHYP model at diastolic loading.

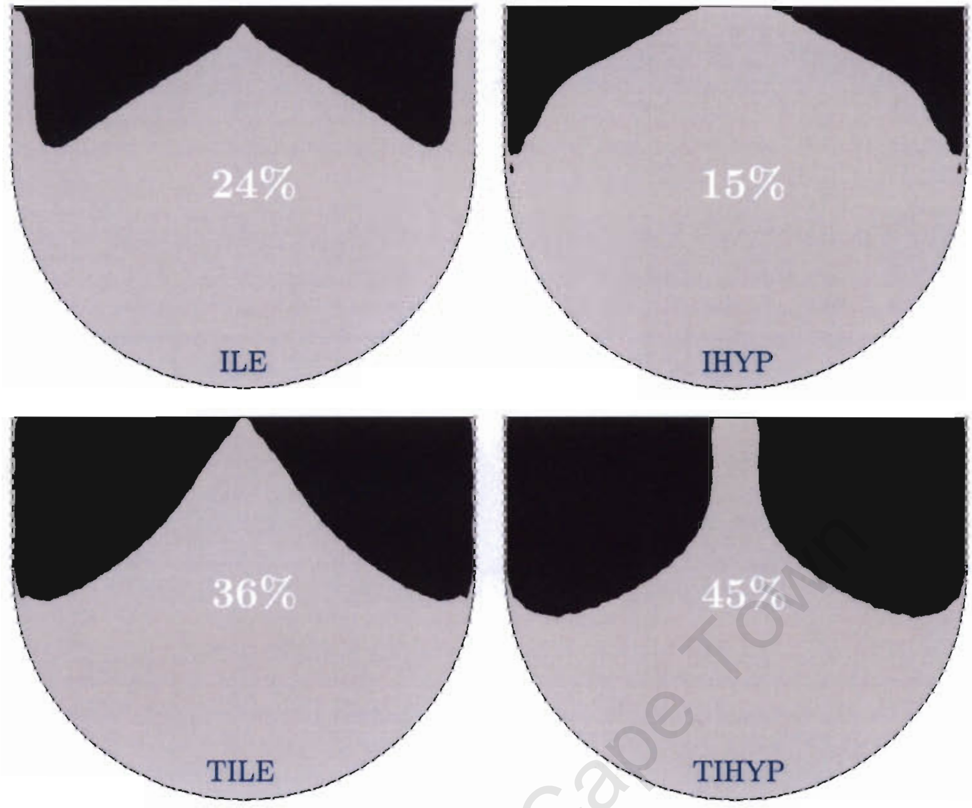

Figure 4.33: Coaptation surface (in black) of the diastolic leaflets on the undeformed leaflet shape, including the ratio of its area to total undeformed leaflet area.

4.2.7 Comparison

Away from the line of leaflet attachment, the nature of the strain field in Figure 4.21 during peak systole is, apart from the lower parts of the TIHYP leaflet, consistent across the leaflet models. The direction of maximum principal strain is predominantly coincident with the circumferential leaflet direction with a downwardly angled section near the commissural heights, particularly pronounced in the TI models. The bottom region of the peak systolic TIHYP leaflet is a special case, in that the role of maximum and minimum principal strain in the other models is interchanged. During end systole however, even the TIHYP model is consistent

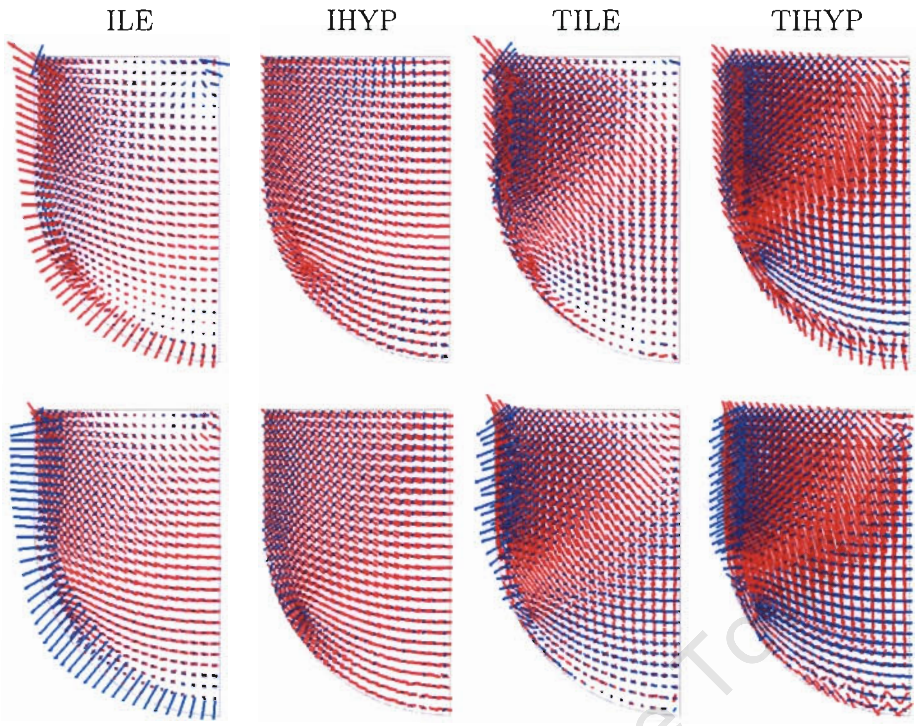

Figure 4.34: Vector plots of principal logarithmic strain in the leaflets during diastolic loading. Maximum principal are plotted red, minimum principal strains blue. The aortic leaflet side is plotted on top, the ventricular on the bottom.

with other models in this regard. Moreover, taking into account the stresses of the fibre reinforcement, the peak systolic stress field is qualitatively similar in all models. The largest discrepancies are found in the neighbourhood of the leaflet annulus.

Quantitatively, differences between the various model can be substantial, especially considering regional variance. The high non–linearity of the IHYP material leads to a more even distribution of strain with a smaller range than in other models, the maximum in peak systolic strain in ILE is 33%, in TIHYP 30%, but in IHYP only 12%. Apart from the localized maximum however, strain in IHYP is higher than in ILE. The distribution of maximum principal strain is very similar

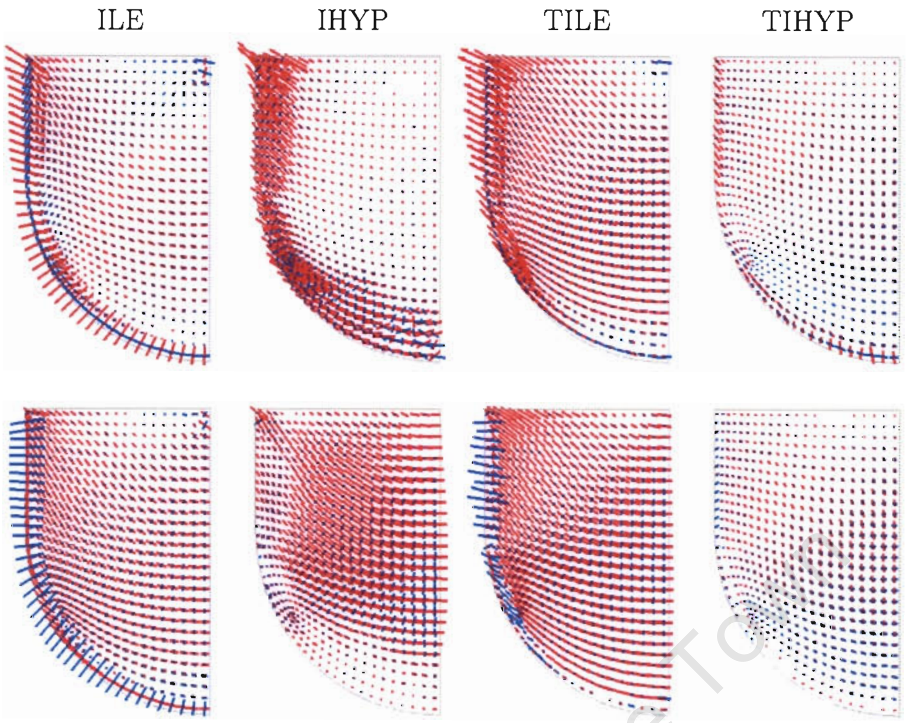

Figure 4.35: Vector plots of principal stresses in the leaflets during diastolic loading. Maximum principals are plotted red, minimum principal stresses blue. The aortic leaflet side is plotted on top, the ventricular on the bottom.

in ILE and TILE as this is governed by the circumferential leaflet direction and these models are similar in this regard. Again, the non-linear model TIHYP shows larger strains than the linear counterpart TILE. As a result of radial compliance in the TI leaflets, the range in the distribution of minimum principal strains, which are largely in that direction, is larger than in their isotropic partners. In particular, the extent to positive values in the TI models. The TIHYP model shows the largest range in that variable.

The isotropic models exhibit a similar distribution of maximum principal stress in peak systole, with higher values and a steeper gradient towards leaflet attachment in IHYP. The stresses in the TI leaflets are comparatively lower. The max-

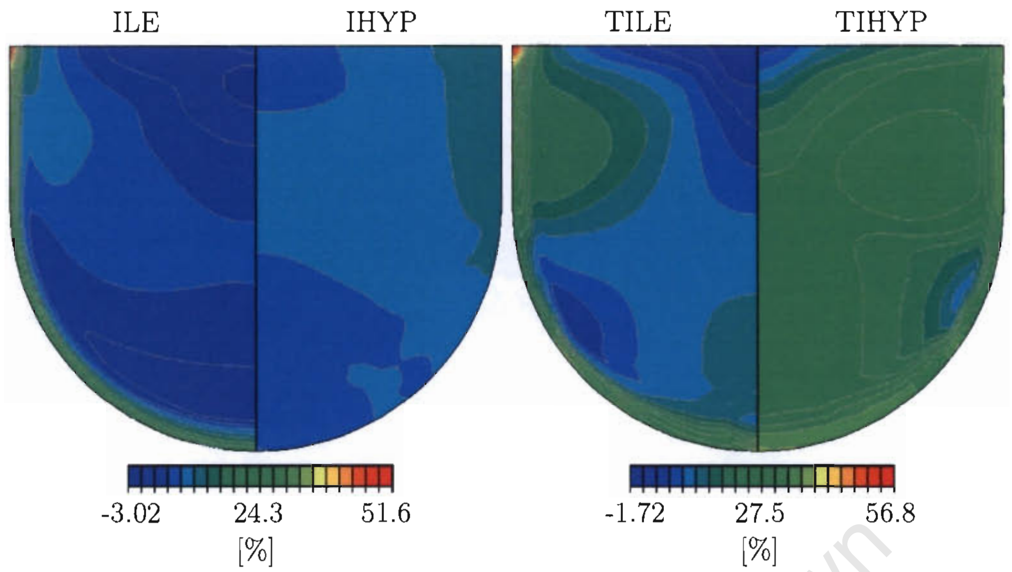

Figure 4.36: Maximum principal strain on the aortic sides of the leaflets at diastolic loading.

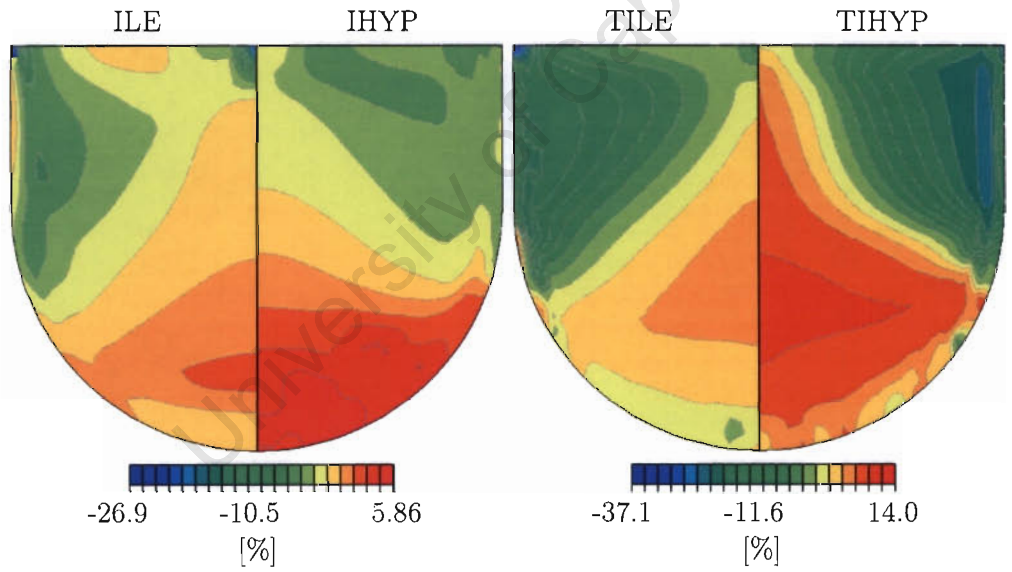

Figure 4.37: Minimum principal strain on the aortic sides of the leaflets at diastolic loading.

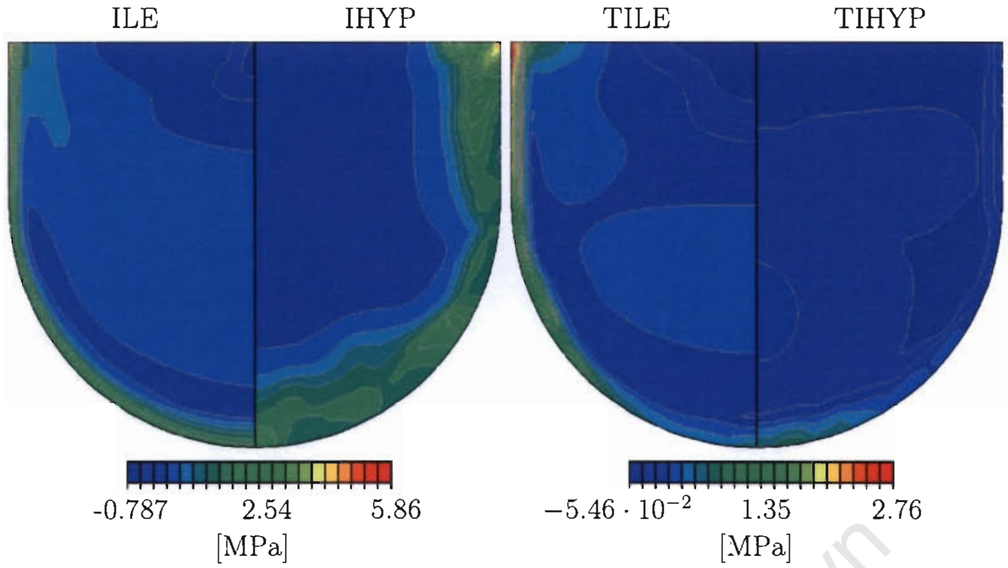

Figure 4.38: Maximum principal stress on the aortic sides of the leaflets at diastolic loading.

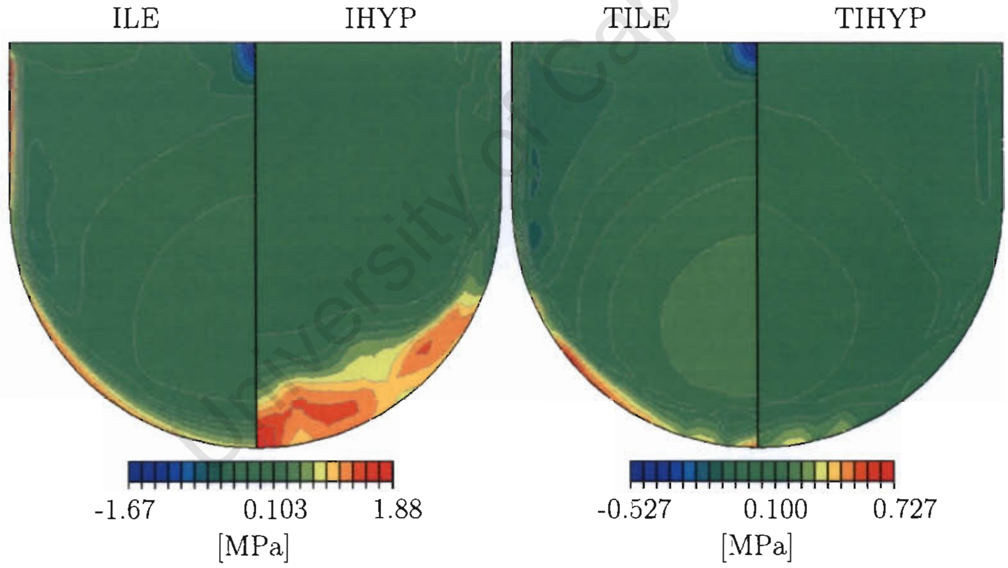

Figure 4.39: Minimum principal stress on the aortic sides of the leaflets at diastolic loading.

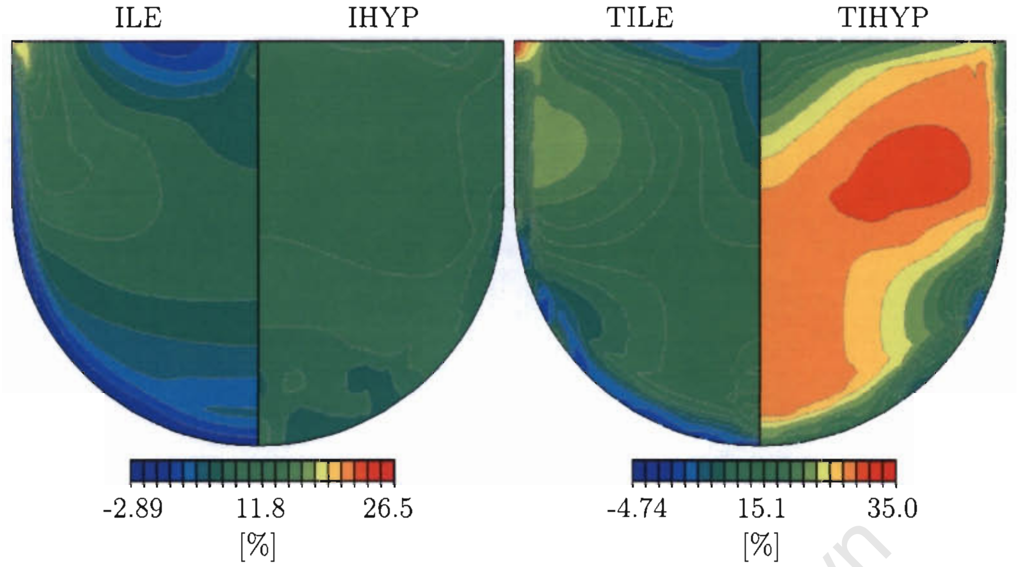

Figure 4.40: Maximum principal strain on the ventricular sides of the leaflets at diastolic loading.

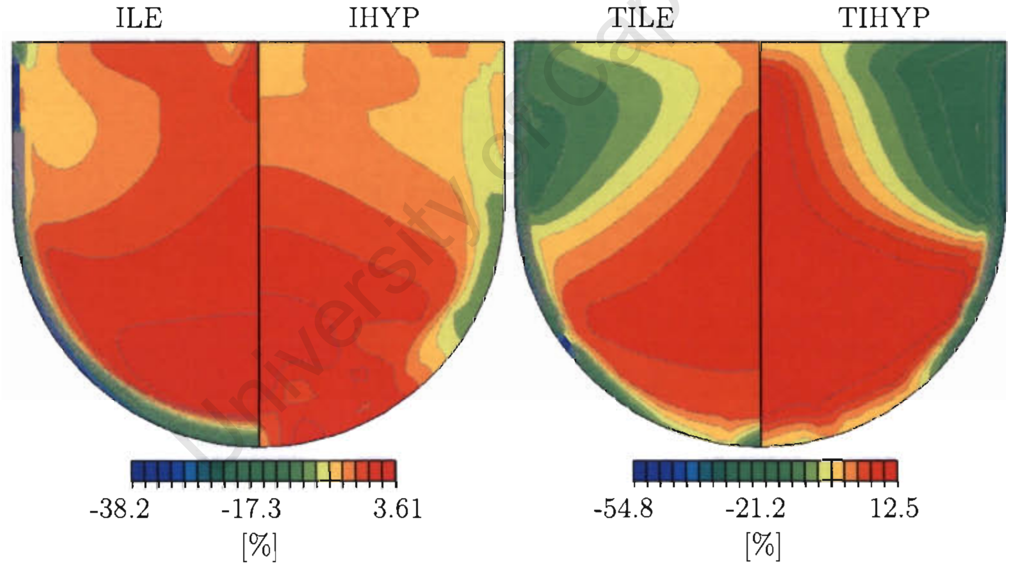

Figure 4.41: Minimum principal strain on the ventricular sides of the leaflets at diastolic loading.

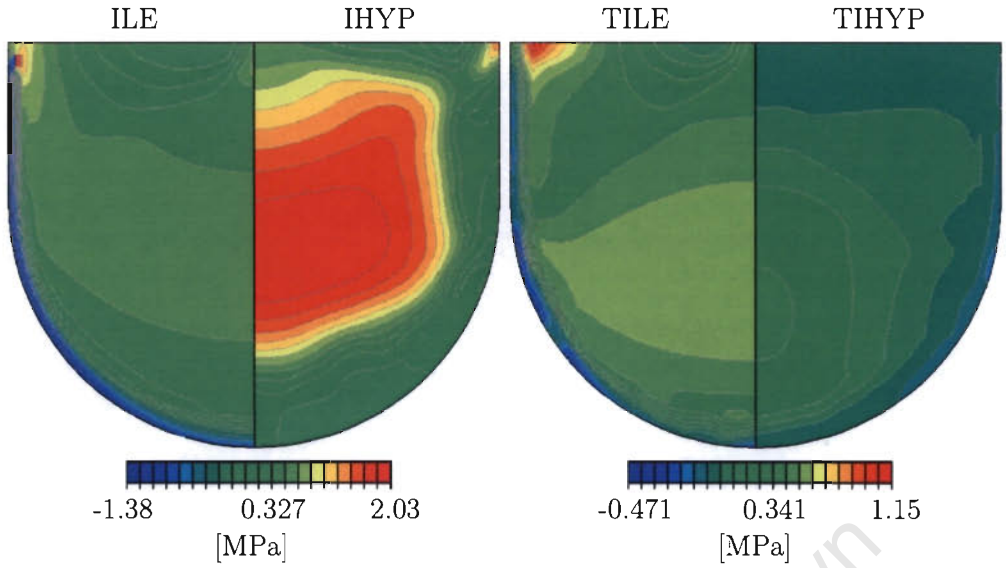

Figure 4.42: Maximum principal stress on the ventricular sides of the leaflets at diastolic loading.

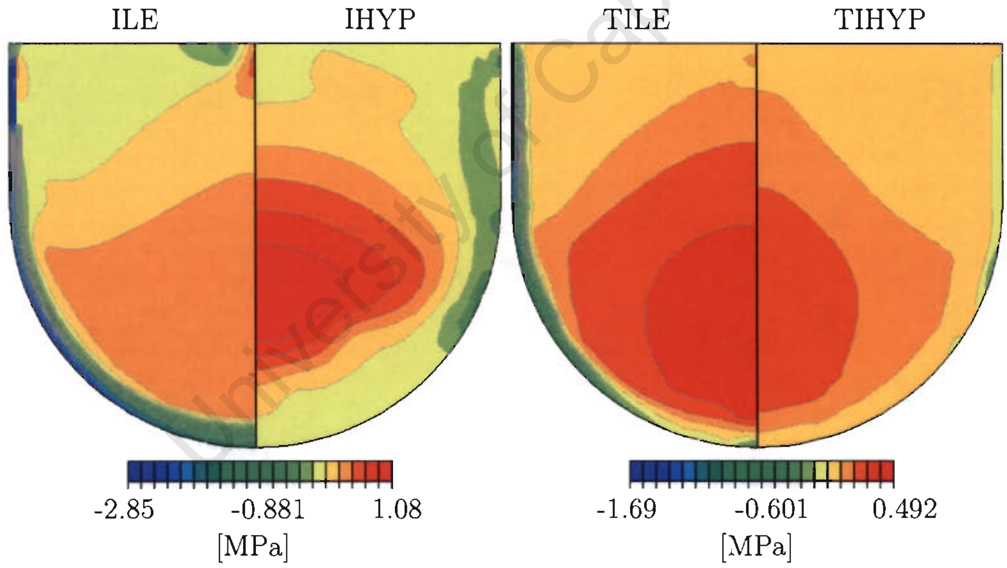

Figure 4.43: Minimum principal stress on the ventricular sides of the leaflets at diastolic loading.

imum peak systolic stress is 3.8 MPa in IHYP, but only 2.2 MPa fibre stress in TIHYP and 1.9 MPa in TILE. Considering minimum principal stresses ILE and IHYP have similar contours apart from large compressive stresses in ILE. These are substantially reduced by adding anisotropy and non–linearity, i.e. ILE has a minimum of -2.8 MPa, TILE -800 kPa, IHYP -320 kPa, and TIHYP only -40 kPa.

In diastole, the free edge angles of the leaflets differ by only a few degrees, with IHYP on the low end with 20.6°, followed by ILE with 23.2°, TIHYP with 23.5°, and finally TILE with 25.4°. Also, the qualitative behaviour in the circumferential direction of all models considered here is quite similar, in that maximum stresses and strains emanate at a downward angle to the horizontal from the commissural heights to increasingly align with the circumferential leaflet direction in the belly area, especially in the isotropic hyperelastic model and the collagen reinforcement in TIHYP. Apart from the site of leaflet attachment, linear and non–linear results do not seem dramatically different, in each of the isotropic and transversely isotropic cases.

Between them however, the most striking difference in results appears to be the amount of coaptation area produced. Only the ILE leaflet fully closes, IHYP shows the most severe central insufficiency. Considering the ratio of coaptation area to total leaflet area, the isotropic leaflets are on the lower end with 15% and 24% for IHYP and ILE respectively. Coaptation area is 36% of total leaflet area in TILE and finally 45% in the case of TIHYP. The increase in coaptation area from isotropic to transversely isotropic and from linear to non–linear materials is reflected in larger radial strains and a very pronounced transition region between leaflet belly and coaptation as seen in Figure 4.34, and quantitatively in Figure 4.36, Figure 4.37, Figure 4.40, Figure 4.41. As can be seen in these contour plots, the strains in the non linear models are higher than in their linear counterparts in most parts of the leaflet. The highest values occur in the linear models however, along the lines of leaflet attachment. Especially the ILE model is a unique case in that area. The principals are mostly perpendicular to that line only in this model with strains in excess of 21% up to a maximum of 51% on the aortic side and negative strains on the ventricular side ranging from −11% to −38.2%. The corresponding hyperelastic model has a maximum strain of 12.5%

and a minimum of −11.2% in the attachment area. The strain field in the hyperelastic leaflet is therefore more uniform and does not have as high gradients towards the attachment as the ILE leaflet displays. The situation is similar in the TI models. Strains are higher in the case of TIHYP everywhere except along the leaflet attachment, where the TILE model exhibits peak values of up to 56.7% strain on the aortic side and down to −54.7% on the ventricular side.

Whereas the strains are mostly higher in the non–linear models as compared to their linear counterparts, the corresponding stresses are higher in the latter in most leaflet areas. Maximum principal stresses are less than 0.5MPa everywhere apart from the attachment area in the ILE leaflet and even less than 0.2MPa in IHYP. They range from 0.2MPa to 0.7MPa in TILE and lie between 0.01MPa and 0.36MPa in the TIHYP leaflet where it has to be kept in mind that the stresses in the reinforcement are reported separately between 0.1MPa and 0.6MPa. Maximum values along the leaflet attachment are 4.4MPa and 4.8MPa for ILE and IHYP respectively, 2.8MPa in TILE and 1.1MPa and 0.9MPa in the TIHYP leaflet and the reinforcement layer respectively.

The hyperelastic models hardly give rise to compressive stresses in the leaflets, the minima being −0.79MPa in the IHYP, and −0.26MPa in the TIHYP leaflet. The linear models on the other hand produce negative stresses down to −1.7MPa in TILE and even down to −2.8MPa in the attachment area of the ventricular side of the ILE leaflet.

4.2.8 Discussion

Finite element models of the aortic root and valve have been presented. The geometry of the models was based on the assumption of symmetry, which is not strictly anatomical, especially since only two of the three sinuses have coronary ostia. These have been neglected in the models discussed here. Aortic valve asymmetry influences the results of the simulations and was shown by Grande–Allen et al. [58] who used magnetic resonance imaging to construct the geometry of their model. This degree of sophistication was beyond the scope of this study. A representative valve model could nevertheless be created, with dimensions in accordance with models by other researchers summarized in Table 4.1 and typical dimensions of the human aortic valve [139]. As discussed in Section 2.1.4, the thickness of both leaflets and aortic root varies greatly, which was another aspect of valve geometry that was considered dispensable here for the focus on leaflet material models.

The mesh size of a total of 2147 elements was, in a preliminary analysis, determined to be the maximum, that could reasonably be used with the computing facilities available. Further mesh refinement would probably improve the results, particularly near stress concentrations. It is however not expected, that new features would emerge in the resulting fields of stress and strain.

In their fluid–structure analysis, De Hart et al. [39] target the systolic phase of the cardiac cycle and assume an end–diastolic stress–free configuration of the valve at a pressure of 80 mmHg. In contrast to that, Grande–Allen et al. [58] and Beck et al. [2] use a stress–free configuration at zero pressure with a closed leaflet. Here, an open, unloaded configuration for the stress–free leaflet was assumed, in agreement with fresh explanted aortic valves and the model by Gnyaneshwar et al. [55]. It is however questionable, that the open leaflet fits perfectly cylindrically into the undeformed aortic root as seen in Figure 4.1 of the model geometry. It might be, that the collapsed leaflets are larger than to fit the undeformed annulus. In that case, the leaflet strains reported in the previous sections would be exaggerated. Lack of data however justifies this conservative approach.

The models discussed here emphasized the use of various constitutive models for the aortic leaflets. Linear elastic models have been compared to hyperelastic models, both isotropic and transversely isotropic. The parameters of the transversely isotropic linear model have previously been used by Grande–Allen et al. [58]. The transversely isotropic hyperelastic model is similar to the model of De Hart et al. [41, 39]. They used a Neo-Hookean matrix reinforced with two fibre layers in the leaflet, one in primarily circumferential the other in predominantly radial direction. Both fibre families have identical properties, which they showed produce a similar uniaxial stress–strain response as porcine aortic leaflets in circumferential direction. They however fell short of demonstrating the response of their composite leaflet in radial direction, and hence neglected to show the degree of anisotropy. Considering the markedly higher circumferential leaflet stresses utilized to determine their fibre properties, their resulting leaflet was likely to behave similar in both (the radial and the circumferential) directions. It was discussed in Section 3.2, that the path taken here was more phenomenological in that a non–linear matrix with exponential stress-strain characteristics was reinforced by only one fibre layer with properties resembling the circumferential leaflet behaviour. As has been shown in Figure 4.2, excellent agreement with uniaxial experimental data can be achieved with this approach. It should however be expected, that this constitutive model needs refinement if it is to capture more details of leaflet mechanics, e.g. biaxial tensile behaviour. Moreover, viscoelastic properties of the tissue have been completely ignored.

Like leaflet tissue, aortic root tissue also exhibits non–linear material behaviour and an appropriate constitutive model should be used for its simulation. As the results of the computations with a maximum strain in the root of 41.2% (see Section 4.2.2) together with the uniaxial tension results of root specimen in Section 2.2.4 suggest, the tissue should operate in a low–modulus or transition phase. Considering that this maximum only occurred very localized fortifies this finding. A material model with appropriate properties for the aortic root would however lead to excessive deformation and ultimately to failure of the simulation, as it was set up here. Implementing further details of thickness distribution and allowing longitudinal strains might solve this problem. To overcome these added complexities of the model, a linear material was assigned to the aortic root nonetheless. The emphasis on leaflet non–linearities should justify this shortcoming.

To obtain physiologically relevant deformations in both aortic root and leaflet, Young's modulus of the root has been adjusted to obtain diameter compliance at the top node of the model as measured in vivo in humans (Section 4.1.4). The values of around 1.3 MPa are roughly four times higher than the values used by Grande–Allen et al. [58]. They however have applied tension to the top nodes of their models and moreover used geometrically linear analysis, so that direct comparison is difficult. Gnyaneshwar et al. [55] on the other hand used a higher value of 2 MPa for the aortic root, and Beck et al. [2] even 6 MPa. Finally, the root moduli employed here agree well with parameters used by De Hart et al. [41, 39]. Values of this magnitude suggest that the root operates in the post–transition

Author	T	STJ	C	SC	LA
this study	11%	11%	19%	5%	15%
Brewer et al. [9]			16%		
Thubrikar et al. [141, 142]					22%
Lockie et al. [92]		11%			
Robicsek et al. [116]			9%		
Vesely et al. [148]			15%		
Lansac et al. [86]	11%	16%	26%	16%	11%

Table 4.5: Comparison of changes in aortic root radii from diastole to peak systole. Top (T), Sinotubular Junction (STJ), Commissures (C), Sinus Centre (SC), Leaflet Attachment (LA).

region.

A further limitation of the models treated here is the static setup, where the interaction of blood with valve tissue is reduced to the application of uniform pressure. This has repercussions on the dynamics, or dimensional changes in this case, of the aortic root. The simulated aortic root dilates as a function of increasing pressure to variable degrees at different heights, but synchronically (Section 4.2.2). The situation in vivo is time critical and more complex, in that expansion at different levels takes place at various stages of the cardiac cycle. Thubrikar et al. [141, 142] for instance studied the motion of the aortic root in vivo in dogs and found that the radius of the base of the leaflet attachment is at a maximum at end diastole and at a minimum at the end of systole, after the valve just closed. This is contrary to the simulated maximum at peak systole and minimum at diastole. It has to be kept in mind, that the aortic valve is not isolated and it should therefore not be surprising that its dynamics, influenced by surrounding tissues like the contracting left ventricle, cannot be captured by the static application of uniform pressure. Additionally, in vivo deformation of the aortic root was found to be asymmetrical [145] including root elongation, shear and torsion [37]. The choice of symmetry assumptions, boundary and loading conditions of the current models hinder such modes of deformation.

Deformation of the aortic root was studied by numerous researchers by placing some form of marker at prominent points of the tissue, e.g. the top of the commissural heights and sinotubular junction or the nadir of leaflet annulus. The motion of the marker was then recorded as a function of pressure. This was done on dog valves in a pulse duplicator [9] or in vivo [141, 142], on porcine [148] and human [92, 116] valves in a pulse duplicator and in vivo in sheep [86]. Regardless of the limitations to reproduce the dynamics of the aortic root as discussed above, the dimensional changes of the simulated root are in tune with the results of those experiments. A detailed comparison of the relative increase of radii at various levels from diastole to peak systole can be found in Table 4.5. Moreover, the finding that the commissural radius is slightly smaller than the sinotubular value in diastole and slightly larger in peak systole [86] is correctly reflected in the model. The chosen setup of the aortic root model thus provided a physiologically meaningful environment for the leaflet to operate in, and since the emphasis was on the leaflet material, the simplifications were considered justified.

As mentioned earlier, model properties of earlier finite element models differ substantially, starting from the initial open or closed configuration, the choice of material models and parameters, to the application of loads and boundary conditions. A direct comparison of results is therfore only meaningful, if those differences are kept in mind. Beck et al. [2] for example report a maximum leaflet stress of only 300 kPa in their model with extensible root, compared to a substantially greater maximum of 4.4 MPa in the ILE model (with properties closest to theirs). They have used an isotropic linear elastic model with the same high modulus of 6 MPa for both leaflet and root and started the diastolic analysis from a closed leaflet position, which accounts for these differences. Stresses in the aortic root on the other hand compare well with the results of De Hart et al. [39], especially in terms of distribution. Their maximum stress of 249 kPa is again significantly lower than the 692 kPa reported here. They however concentrate on the systolic phase and assume a stress–free state at 80 mmHg. Other results, particularly of the TILE model, lie in the same region as reported by Grande–Allen et al. [58], although they only employed a linear finite element model. Differences are along the leaflet attachment, where the values reported here are considerably higher, due also to the different starting point of the analysis with the leaflet in an open position.

The peak systolic leaflet gestalt with a triangular orifice in all models is a feature in fact observed experimentally, e.g. in pulse duplicator systems [108, 116], and is also consistent with the model deformation of De Hart et al. [39]. The same is true for the closed diastolic shape. A look at the corresponding figures (Figures 4.14, 4.16, 4.18, and 4.20) shows, that only the ILE model fully closes and all other models exhibit some degree of central insufficiency, IHYP being the most severe case. The natural leaflet has a thickening in that area, the nodule of Arrantius, which has not been accounted for in the models but would seal the valves and enables the TIHYP leaflet to fully close without any compressive stresses in that area.

Differences in the results of the four models are more readily seen in diastole. The first striking distinction is in the amount of coaptation surface, with the highest value in the TIHYP model. Leaflet free edge angle on the other hand does not vastly sway and is probably more influenced by valve geometry and dimensions. The average value of all models is 23.2° and is somewhat smaller than the average of 40° measured on excised human valve [139]. This value is however an average over all valves and pressures in their study and a value of 25° (similar to the TILE value) at 80 mmHg pressure was indeed recorded.

Peak values of stress are greatly reduced in the TI models. In particular, the magnitudes of compressive stresses are reduced in the hyperelastic models in agreement with findings by Patterson et al. [109] who concluded that linear models would overestimate the damage compressive stresses might have on leaflet tissue. Peak values of strain are considerably lower in the non–linear models. In fact, the peak strains of the linear models in the area of leaflet attachment in excess of 50% are not likely physiological. On the contrary, strains of that magnitude are up to a factor two greater than reported failure strains in the circumferential leaflet direction [110, 38, 150].

Considering the differences in the constitutive models used for the leaflets, the qualitative similarity of maximum stresses in the circumferential direction is remarkable. It was observed that they are directed at a downward angle in the commissural heights and coaptation area and only in the leaflet belly do they align with the circumferential direction. This orientation seems to agree with the coarse collagen fibre distribution in the leaflet [5], as seen in Figure 2.13 and Figure 2.14, and should probably be taken into account when defining the fibre direction $\mathbf{a}_0$.

Chapter 5

Conclusion and Recommendations

5.1 Conclusion

Non–linear finite element models of the aortic heart valve have been presented in the previous chapter with a detailed analysis on how leaflet non–linearity and anisotropy affect the results.

To render the study computationally feasible, a number of simplifications were necessary. Among the most significant were the static nature of the analyses, the assumption of symmetries that allow the models to be reduced to one sixth of the valve and the retreat to an isotropic linear elastic material model for the aortic root. By adjusting Young's modulus of that model until the root yielded diameter compliance in accordance with a value measured in vivo, a physiologically relevant environment has been provided for the leaflets.

It was demonstrated that the constitutive model for the TIHYP leaflet is capable of fitting uniaxial tension test data obtained from fresh leaflet strips in different directions. A finite element model of a leaflet incorporating the observed high degrees of both anisotropy and non–linearity and operating in a distensible aortic root subject to full physiological pressures has not previously been published.

This investigation has been confined to static analyses, and exactly how the constitutive models impact on the complex dynamics of the valve has to be left for future work incorporating dynamics. The results nevertheless show some important aspects of aortic valve mechanics. Taking into account the anisotropy of leaflets with their radial compliance is crucial to obtain proper coaptation. Material non-linearities impact on the simulated fields with a more even distribution and more importantly, peak strains and stresses are in the elastic range of the tissue.

5.2 Recommendations

An obvious route to improve the presented finite element models of the aortic valve is to eradicate the need for some of the simplifications imposed. Mesh refinement, possibly employing adaptive techniques, could be beneficial. Dynamic analyses, as mentioned above, should be carried out to fully understand valve functioning. Above all, a non-linear constitutive model should be employed for the aortic root.

As far as the constitutive model for the leaflets is concerned, it might prove fruitful to investigate modifications to extend its capabilities to represent biaxial tensile test data. Furthermore, the model should be implemented as one user supplied subroutine (UMAT) in ABAQUS. This would also enable the use of the model to further study collagen fibre remodelling, recently embarked on by Driessen et al. [45, 46].

Since the orientation of maximum principal stresses in the leaflet seem to roughly follow the collagen architecture of the natural leaflet, an investigation into the impact of fibre orientation in the leaflet on deformation and stress could be very useful to gain insight into valve mechanics. This information might aid in the design of scaffolds for tissue engineering of aortic valves, especially if optimization techniques to target fibre architecture are employed.

Bibliography

[1] R.I. Bashey, T. Torii, and A. Angrist. Age-related collagen and elastin content of human heart valves. *J. Gerontol.*, 22:203–208, 1967.

[2] A. Beck, M.J. Thubrikar, and F. Robicsek. Stress analysis of the aortic valve with and without the sinuses of valsalva. *J. Heart Valve Dis.*, 10:1–11, 2001.

[3] B.J. Bellhouse and L. Talbot. The fluid mechanics of the aortic valve. *J. Fluid Mech.*, 35:721–735, 1969.

[4] T. Belytschko, W.K. Liu, and B. Moran. *Nonlinear Finite Elements for Continua and Structures.* John Wiley & Sons, Chichester, UK, 2000.

[5] K.L. Billiar and M.S. Sacks. Biaxial mechanical properties of the natural and glutaraldehyde treated aortic valve cusp – part i: Experimental results. *J. Biomech. Eng.*, 122:23–30, 2000.

[6] K.L. Billiar and M.S. Sacks. Biaxial mechanical properties of the natural and glutaraldehyde-treated aortic valve cusp: Part ii – a structural constitutive model. *J. Biomech. Eng.*, 122:327–335, 2000.

[7] M.M. Black, I.C. Howard, X. Huang, and E.A. Patterson. A three-dimensional analysis of a bioprosthetic heart valve. *J. Biomechanics*, 24:793–801, 1991.

[8] S.A. Blome-Eberwein, D. Mrowinski, J. Hofmeister, and R. Hetzer. Impact of mechanical heart valve prosthesis sound on patients' quality of life. *Ann. Thorac. Surg.*, 61:594–601, 1996.

[9] R.J. Brewer, J.D. Deck, B. Capati, and S.P. Nolan. The dynamic aortic root. *J. Thorac. Cardiovasc. Surg.*. 72:413–417, 1976.

[10] G. Burriesci, I.C. Howard, and E.A. Patterson. Influence of anisotropy on the mechanical behaviour of bioprosthetic heart valves. *J. Med. Eng. Tech.*, 23:203–215, 1999.

[11] G. Cacciola, G.W.M. Peters, and P.J.G. Schreurs. A three-dimensional mechanical analysis of a stentless fibre-reinforced aortic valve prosthesis. *J. Biomechanics*, 33:521–530, 2000.

[12] G.R. Cacciola. *Design, simulation and manufacturing of fiber reinforced polymer heart valves.* PhD thesis, Technische Universiteit Eindhoven, Netherlands, 1998.

[13] N.A. Campbell. *Biology.* The Benjamin/Cummings Publishing Company, Redwood City, USA(CA), third edition, 1993.

[14] E. Carew, J.E. Barber, and I. Vesely. Role of preconditioning and recovery time in repeated testing of aortic valve tissue: Validation through quasilinear viscoelastic theory. *Ann. Biomed. Eng.*, 28:1093 1100, 2000.

[15] T.E. Carew, R.N. Vaishnav, and D.J. Patel. Compressibility of the arterial wall. *Circ. Res.*, 23:61–68, 1968.

[16] A. Cataloglu, R.E. Clark, and P.L. Gould. Stress analysis of aortic valve leaflets with smoothed geometrical data. *J. Biomechanics*, 10:153–158, 1977.

[17] A. Cataloglu, P.L. Gould, and R.E. Clark. Refined stress analysis of human aortic heart valves. *J. Mech. Eng. Div.*, 102:135–150, 1976.

[18] K.B. Chandran, S.-H. Kim, and G. Han. Stress distribution on the cusps of a polyurethane trileaflet heart valve prosthesis in the closed position. *J. Biomechanics*, 24:385–395, 1991.

[19] G.G. Chew, I.C. Howard, and E.A. Patterson. Simulation of damage in a porcine prosthetic heart valve. *J. Med. Eng. Tech.*, 23:178–189, 1999.

[20] M. Chiquet, A.S. Renedo, F. Huber, and M. Flück. How do fibroblasts translate mechanical signals into changes in extracellular matrix production? *Matrix Biol.*, 22:73–80, 2003.

[21] S.J. Choo, G. McRae, J.P. Olomon, G. St. George, W. Davis, C.L. Burleson-Bowles, D. Pang, H.H. Luo, D. Vavra, D.T. Cheung, J.H. Oury, and C.M.G. Duran. Aortic root geometry: Pattern of differences between leaflets and sinuses of valsalva. *J. Heart Valve Dis.*, 8:407–415, 1999.

[22] G.W. Christie and B.G. Barratt-Boyes. Identification of a failure mode of the antibiotic sterilized aortic allograft after 10 years: Implications for their long-term survival. *J. Cardiac Surg.*, 6:462–467, 1991.

[23] G.W. Christie and B.G. Barratt-Boyes. On stress reduction in bioprosthetic heart valve leaflets by the use of a flexible stent. *J. Cardiac Surg.*, 6:476–481, 1991.

[24] G.W. Christie and B.G. Barratt-Boyes. Age-dependent changes in the radial stretch of human aortic valve leaflets determined by biaxial testing. *Ann. Thorac. Surg.*, 60:S156–S159, 1995.

[25] G.W. Christie and B.G. Barratt-Boyes. Biaxial mechanical properties of explanted aortic allograft leaflets. *Ann. Thorac. Surg.*, 60:S160–S164, 1995.

[26] G.W. Christie and B.G. Barratt-Boyes. Mechanical properties of porcine pulmonary valve leaflets: How do they differ from aortic leaflets? *Ann. Thorac. Surg.*, 60:S195–S199, 1995.

[27] G.W. Christie and I.C. Medland. A non-linear finite element stress analysis of bioprosthetic heart valves. In R.H. Gallagher, B.R. Simon, P.C. Johnson, and J.F. Gross, editors, *Finite Elements in Biomechanics*, chapter 9. John Wiley and Sons, Hoboken, USA(NJ), 1982.

[28] C.J. Chuong and Y.C. Fung. Compressibility and constitutive equation of arterial wall in radial compression experiments. *J. Biomechanics*, 17:35–40, 1984.

[29] R.E. Clark. Stress-strain characteristics of fresh and frozen human aortic and mitral leaflets and chordae tendineae. *J. Thorac. Cardiovasc. Surg.*, 66:202–208, 1973.

[30] R.E. Clark and G.A.M. Butterworth. Characterization of the mechanics of human aortic and mitral valve leaflets. *Surg. Forum*, 22:134–136, 1971.

[31] R.E. Clark and E.H. Finke. Scanning and light microscopy of human aortic leaflets in stressed and relaxed states. *J. Thorac. Cardiovasc. Surg.*, 67:792–804, 1974.

[32] S.E. Clift and J. Fisher. Finite element stress analysis of a new design of synthetic leaflet heart valve. *Proc. Instn. Mech. Engrs. Part H*, 210:267–272, 1996.

[33] M. Comninou and I.V. Yannas. Dependence of stress-strain nonlinearity of connective tissues on the geometry of collagen fibers. *J. Biomechanics*, 9:427–433, 1976.

[34] M.A. Crisfield. A fast incremental/iterative solution procedure that handles "snap-through". *Computers & Structures*, 13:55–62, 1980.

[35] M.A. Crisfield. *Non-linear Finite Element Analysis of Solids and Structures*, volume 1: Essentials. John Wiley & Sons, Chichester, UK, 1991.

[36] M.A. Crisfield. *Non-linear Finite Element Analysis of Solids and Structures*, volume 2: Advanced Topics. John Wiley & Sons, Chichester, UK, 1997.

[37] P. Dagum, G.R. Green, F.J. Nistal, G.T. Daughters, T.A. Timek, L.E. Foppiano, A.F. Bolger, N.B. Ingels, and D.C. Miller. Deformational dynamics of the aortic root. *Circulation*, 100:II54–II62, 1999.

[38] H. David, D.R. Boughner, I. Vesely, and G. Gerosa. The pulmonary valve. is it mechanically suitable for use as an aortic valve replacement? *ASAIO J.*, 40:206–212, 1994.

[39] J. De Hart, F.P.T. Baaijens, G.W.M. Peters, and P.J.G. Schreurs. A computational fluid-structure interaction analysis of a fiber-reinforced stentless aortic valve. *J. Biomechanics*, 36:699–712, 2003.

[40] J. De Hart, G. Cacciola, P.J.G. Schreurs, and G.W.M. Peters. A three-dimensional analysis of a fibre-reinforced aortic valve prosthesis. *J. Biomechanics*, 31:629–638, 1998.

[41] J. De Hart, G.W.M. Peters, P.J.G. Schreurs, and F.P.T. Baaijens. A three-dimensional computational analysis of fluid-structure interaction in the aortic valve. *J. Biomechanics*, 36:103–112, 2003.

[42] J. De Hart, G.W.M. Peters, P.J.G. Schreurs, and F.P.T. Baaijens. Collagen fibers reduce stresses and stabilize motion of aortic valve leaflets during systole. *J. Biomechanics*, 37:303–311, 2004.

[43] W.F. Decraemer, M.A. Maes, and V.J. Vanhuyse. An elastic stress-strain relation for soft biological tissues based on a structural model. *J. Biomechanics*, 13:463–468, 1980.

[44] H. Demiray. A note on the elasticity of soft biological tissues. *J. Biomechanics*, 5:309–311, 1972.

[45] NJB. Driessen, G.W.M. Peters, J.M. Huyghe, C.V.C. Bouten, and F.P.T. Baaijens. Remodelling of continuously distributed collagen fibres in soft connective tissues. *J. Biomechanics*, 36:1151–1158, 2003.

[46] NJB. Driessen, W. Wilson, C.V.C. Bouten, and F.P.T. Baaijens. A computational model for collagen fibre remodelling in the arterial wall. *J. Theo. Biol.*, 226:53–64, 2004.

[47] N. Dürrlemann, M. Pellerin, D. Bouchard, Y. Hebert, R. Cartier, L.P. Perrault, A. Basmadjian, and M. Carrier. Prosthetic valve thrombosis: Twenty-year experience at the montreal heart institute. *J. Thorac. Cardiovasc. Surg.*, 127:1388–1392, 2004.

[48] C. Ferraresi, A. Manuello Bertetto, C. Mazza, W. Franco, and D. Maffiodo. Opening mechanics of the aortic root: Non homogeneous and non isotropic f.e.m. model of biological structure. *Mech. Res. Commun.*, 25:405–413, 1998.

[49] O. Frank. Die grundform des arteriellen pulses erste abhandlung: Mathematische analyse. *Z. Biol.*, 37:483–526, 1899.

[50] Free Software Foundation, http://www.gnuplot.info. *GNUPLOT*, 2002.

[51] J.R. Fuchs, A. Nasseri, and J.P. Vacanti. Tissue engineering: A 21st century solution to surgical reconstruction. *Ann. Thorac. Surg.*, 72:577–591, 2001.

[52] Y.C. Fung. *Biomechanics: Mechanical properties of living tissue.* Springer-Verlag, New York, USA(NY), second edition, 1993.

[53] Y.C. Fung, K. Fronek, and P. Patitucci. Pseudoelasticity of arteries and the choice of its mathematical expression. *Am. J. Phyisol.*, 237:H620–H631, 1979.

[54] V. Gerhardt, editor. *Kant zum Vergnügen. "Man merkt leicht, daß auch kluge Leute bisweilen faseln".* Philipp Reclam jun., Stuttgart, Germany, 2003.

[55] R. Gnyaneshwar, R.K. Kumar, and K.R. Balakrishnan. Dynamic analysis of the aortic valve using a finite element model. *Ann. Thorac. Surg.*, 73:1122–1129, 2002.

[56] P.L. Gould, A. Cataloglu, G. Dhatt, A. Chattopadhyay, and R.E. Clark. Stress analysis of the human aortic valve. *Computers & Structures*, 3:377–384, 1973.

[57] K.J. Grande. *The aortic root-aortic valve relationship in the normal, diseased, and surgically repaired states.* PhD thesis, University of Washington, USA, 1998.

[58] K.J. Grande, R.P. Cochran, P.G. Reinhall, and K.S. Kunzelman. Stress variations in the human aortic root and valve: The role of anatomic asymmetry. *Ann. Biomed. Eng.*, 26:534–545, 1998.

[59] K.J. Grande, R.P. Cochran, P.G. Reinhall, and K.S. Kunzelman. Mechanisms of aortic valve incompetence in aging: a finite element model. *J. Heart Valve Dis.*, 8:149–156, 1999.

[60] K.J. Grande, R.P. Cochran, P.G. Reinhall, and K.S. Kunzelman. Mechanisms of aortic valve incompetence: Finite element modeling of aortic root dilation. *Ann. Thorac. Surg.*, 69:1851–1897, 2000.

[61] K.J. Grande, K.S. Kunzelman, R.P. Cochran, T.E. David, and E.D. Verrier. Porcine aortic leaflet arrangement may contribute to clinical xenograft failure. *ASAIO J.*, 39:918–922, 1993.

[62] K.J. Grande-Allen, R.P. Cochran, P.G. Reinhall, and K.S. Kunzelman. Recreation of sinuses is important for sparing the aortic valve: A finite element study. *J. Thorac. Cardiovasc. Surg.*, 119:753–763, 2000.

[63] K.J. Grande-Allen, R.P. Cochran, P.G. Reinhall, and K.S. Kunzelman. Finite-element analysis of aortic valve-sparing: Influence of graft shape and stiffness. *IEEE Transact. Biomed. Eng.*, 48:647–659, 2001.

[64] A.E. Green and W. Zerna. *Theoretical Elasticity*. Oxford University Press, London, UK, second edition, 1968.

[65] L. Gross and M.A. Kugel. Topographic anatomy and histology of the valves of the heart. *Am. J. Pathol.*, 7:445–473, 1931.

[66] M.S. Hamid, H.N. Sabbah, and P.D. Stein. Influence of stent height upon stresses on the cusps of closed bioprosthetic valves. *J. Biomechanics*, 19:759–769, 1986.

[67] M.S. Hamid, H.N. Sabbah, and P.D. Stein. Vibrational analysis of bioprosthetic heart valve leaflets using numerical models: Effects of leaflet stiffening, calcification, and perforation. *Circ. Res.*, 61:687–694, 1987.

[68] Hibbitt, Karlsson, Sorenson, Inc., http://www.abaqus.com. *ABAQUS*, 2002.

[69] G.A. Holzapfel, R. Eberlein, P. Wriggers, and H.W. Weizsäcker. Large strain analysis of soft biological membranes: Formulation and finite element analysis. *Comput. Methods Appl. Mech. Engrg.*, 132:45–61, 1996.

[70] X. Huang, M.M. Black, I.C. Howard, and E.A. Patterson. A two-dimensional finite element analysis of a bioprosthetic heart valve. *J. Biomechanics*, 22:753–762, 1990.

[71] P. Human and P. Zilla. Characterization of the immune response to valve bioprostheses and its role in primary tissue failure. *Ann. Thorac. Surg.*, 71:S385–S388, 2001.

[72] J.D. Humphrey, R.K. Strumpf, and F.C.P. Yin. Determination of a constitutive relation for passive myocardium: I. a new functional form. *J. Biomech. Eng.*, 112:333–339, 1990.

[73] J.D. Humphrey, R.K. Strumpf, and F.C.P. Yin. Determination of a constitutive relation for passive myocardium: Ii.— parameter estimation. *J. Biomech. Eng.*, 112:340–346, 1990.

[74] J.D. Humphrey and F.C.P. Yin. A new constitutive formulation for characterizing the mechanical behavior of soft tissues. *Biophys. J.*, 52:563–570, 1987.

[75] J.D. Humphrey and F.C.P. Yin. Biomechanical experiments on excised myocardium: Theoretical considerations. *J. Biomechanics*, 22:377–383, 1989.

[76] International Center for Numerical Methods in Engineering (CIMNE), http://gid.cimne.upc.es. *GiD*, 2002.

[77] S. Kalath, P. Tsipouras, and F.H. Silver. Non-invasive assessment of aortic mechanical properties. *Ann. Biomed. Eng.*, 14:513–524, 1986.

[78] J. Kastelic and E. Baer. Deformation in tendon collagen. *Symp. Soc. Exp. Biol.*, 34:397–420, 1980.

[79] D.W. Kitzman, D.G. Scholz, P.T. Hagen, D.M. Ilstrup, and W.D. Edwards. Age-related changes in normal human hearts during the first 10 decades of life. part ii (maturity): A quantitative anatomic study of 765 specimens from subjects 20 to 99 years old. *Mayo Clin. Proc.*, 63:137–146, 1988.

[80] B. Knierbein, U. Mohr-Matuschek, M. Rechlin, H. Reul, G. Rau, and W. Michaeli. Evaluation of mechanical loading of a trileaflet polyurethane blood pump valve by finite element analysis. *Int. J. Artif. Organs*, 13:307–315, 1990.

[81] S. Krucinski, I. Vesely, M.A. Dokainish, and G. Campbell. Numerical simulation of leaflet flexure in bioprosthetic valves mounted on rigid and expansile stents. *J. Biomechanics*, 26:929–943, 1993.

[82] K.S. Kunzelman, K.J. Grande, T.E. David, R.P. Cochran, and E.D. Verrier. Aortic root and valve relationships. *J. Thorac. Cardiovasc. Surg.*, 107:162 170, 1994.

[83] W.M. Lai, D. Rubin, and E. Krempl. *Introduction to continuum mechanics.* Pergamon Press, Oxford, UK, 1993.

[84] Y. Lanir. A structural theory for the homogeneous biaxial stress-strain relationships in collagenous tissues. *J. Biomechanics*, 12:423–436, 1979.

[85] Y. Lanir. Constitutive equations for fibrous connective tissues. *J. Biomechanics*, 16:1–12, 1983.

[86] E. Lansac, H.S. Lim, Y. Shomura, K.H. Lim, N.T. Rice, W. Goetz, C. Acar, and C.M.G. Duran. A four-dimensional study of the aortic root dynamics. *Eur. J. Cardiothorac. Surg.*, 22:497–503, 2002.

[87] T.C. Lee, R.J. Midura, V.C. Hascall, and I. Vesely. The effect of elastin damage on the mechanics of the aortic valve. *J. Biomechanics*, 34:203–210, 2001.

[88] J. Li, X.Y. Luo, and Z.B. Kuang. A nonlinear anisotropic model for porcine aortic heart valves. *J. Biomechanics*, 34:1279–1289, 2001.

[89] K.O. Lim and D.R. Boughner. The low frequency dynamic viscoelastic properties of human aortic valve tissue. *Circ. Res.*, 39:209–214. 1976.

[90] G. Limbert and M. Taylor. On the constitutive modeling of biological soft connective tissues. a general theoretical framework and explicit forms of the tensors of elasticity for strongly anisotropic continuum fibre-reinforced composites at finite strain. *Int. J. Solids Structures*, 39:2343–2358, 2002.

[91] D. Lo and I. Vesely. Biaxial strain analysis of the porcine aortic valve. *Ann. Thorac. Surg.*, 60:S374–S378, 1995.

[92] K.J. Lockie, M. Butterfield, J. Fisher, N.P. Juster, K. Watterson, and G.A. Davies. Geometry of homograft valve leaflets: Effect of dilation of the aorta and the aortic root. *Ann. Thorac. Surg.*, 56:125–130, 1993.

[93] V.B. Makhijani, H.Q. Yang, P.J. Dionne, and M.J. Thubrikar. Three-dimensional coupled fluid-structure simulation of pericardial bioprosthetic aortic valve function. *ASAIO J.*, 43:M387–M392, 1997.

[94] M. Matthaeus, T. Koch, N. Davies, D. Bezuidenhout, R. Hetzer, and P. Zilla. Mechanical and morphological characterization of decellularized biological heart valve tissue. *to be published*, 2004.

[95] D. Mavrilas and Y. Missirlis. An approach to the optimization of preparation of bioprosthetic heart valves. *J. Biomechanics*, 24:331–339, 1991.

[96] K. May-Newman and F.C.P. Yin. A constitutive law for mitral valve tissue. *J. Biomech. Eng.*, 120:38–47, 1998.

[97] A.S.D. Mayne, G.W. Christie, B.H. Smaill, P.J. Hunter, and B.G. Barratt-Boyes. An assessment of the mechanical properties of leaflets from four second-generation porcine bioprostheses with biaxial testing techniques. *J. Thorac. Cardiovasc. Surg.*, 98:170–180, 1989.

[98] A.D. McCulloch. Cardiac biomechanics. In J.D. Bronzino, editor, *The Biomedical Engineering Handbook*, chapter 28. CRC Press, Boca Raton, USA(FL), 2000.

[99] J.L. Mercer, M. Benedicty, and H.T. Bahnson. The geometry and construction of the aortic leaflet. *J. Thorac. Cardiovasc. Surg.*, 65:511–518, 1973.

[100] M. Mooney. A theory of large elastic deformation. *J. Appl. Phys.*, 11:582–592, 1940.

[101] F.H. Netter. *Interactive Atlas of Human Anatomy.* Novartis, Summit, USA(NJ), 1998.

[102] S. Neuenschwander and S.P. Hoerstrup. Heart valve tissue engineering. *Transplant Immunology*, 12:359–365, 2004.

[103] Y.L. Ng and J.E.C. Wright. Effect of preservation on the elasticity of human aortic valve homografts. *Thorax*, 30:266–270, 1975.

[104] W.W. Nichols and M.F. O'Rourke. *McDonald's blood flow in arteries. Theoretical, experimental and clinical principles.* Arnold, London, UK, fourth edition, 1998.

[105] M.A. Nicosia, R.P. Cochran, D.R. Einstein, C.J. Rutland, and K.S. Kunzelman. A coupled fluid-structure finite element model of the aortic valve and root. *J. Heart Valve Dis.*, 12:781–789, 2003.

[106] M.A. Nicosia, J.S. Kasalko, R.P. Cochran, D.R. Einstein, and K.S. Kunzelman. Biaxial mechanical properties of porcine ascending aortic wall tissue. *J. Heart Valve Dis.*, 11:680–687, 2002.

[107] R.W. Ogden. *Non-linear elastic deformations.* Ellis Horwood, Chichester, UK, 1984.

[108] R.T. Padula, G.S.M. Cowan, and R.C. Camishion. Photographic analysis of the active and passive components of cardiac valvular action. *J. Thorac. Cardiovasc. Surg.*, 56:790–798, 1968.

[109] E.A. Patterson, I.C. Howard, and M.A. Thornton. A comparative study of linear and nonlinear simulations of the leaflets in a bioprosthetic heart valve during the cardiac cycle. *J. Med. Eng. Tech.*, 20:95–108, 1996.

[110] B. Purinya, V. Kasyanov, J. Volkolakov, R. Latsis, and G. Tetere. Biomechanical and structural properties of the explanted bioprosthetic valve leaflets. *J. Biomechanics*, 27:1–11, 1994.

[111] S.H. Rahimtoola. Choice of prosthetic heart valve for adult patients. *J. Am. Coll. Cardiol.*, 41:893–904, 2003.

[112] K. Reid. The anatomy of the sinus of valsalva. *Thorax*, 25:79–85, 1970.

[113] H. Reul, A. Vahlbruch, M. Giersiepen, Th. Schmitz-Rode, V. Hirtz, and S. Effert. The geometry of the aortic root in health, at valve disease and after valve replacement. *J. Biomechanics*, 23:181–191, 1990.

[114] E. Riks. An incremental approach to the solution of snapping and buckling problems. *Int. J. Solids Structures*, 15:529–551, 1979.

[115] F. Robicsek and M. Thubrikar. Are we implanting half-valves? the role of sinus wall compliance in aortic valve function. *Ann. Thorac. Surg.*, 67:597, 1999.

[116] F. Robicsek and M.J. Thubrikar. Role of sinus wall compliance in aortic leaflet function. *Am. J. Cardiol.*, 84:944–946, 1999.

[117] E.P.M. Rousseau, A.A.H.J. Sauren, M.C. van Hout, and A.A. van Steenhoven. Elastic and viscoelastic material behaviour of fresh and glutaraldehyde-treated porcine aortic valve tissue. *J. Biomechanics*, 16:339–348, 1983.

[118] E.P.M. Rousseau, A.A. van Steenhoven, J.D. Janssen, and H.A. Huysmans. A mechanical analysis of the closed hancock heart valve prosthesis. *J. Biomechanics*, 21:545–562, 1988.

[119] H.N. Sabbah, M.S. Hamid, and P.D. Stein. Estimation of mechanical stresses on closed cusps of porcine bioprosthetic valves: Effects of stiffening, focal calcium and focal thinning. *Am. J. Cardiol.*, 55:1091–1096, 1985.

[120] H.N. Sabbah, M.S. Hamid, and P.D. Stein. Mechanical stresses on closed cusps of porcine bioprosthetic valves: Correlation with sites of calcification. *Ann. Thorac. Surg.*, 42:93–96, 1986.

[121] M.S. Sacks. The biomechanical effects of fatigue on the porcine bioprosthetic heart valve. *J. Long-Term Eff. Med. Impl.*, 11:231–247, 2001.

[122] M.S. Sacks, D.B Smith, and E.D. Hiester. The aortic valve microstructure: Effect of transvalvular pressure. *J. Biomed. Mat. Res.*, 41:131 141, 1998.

[123] Y. Sahasakul, W.D. Edwards, J.M. Naessens, and A.J. Tajik. Age-related changes in aortic and mitral valve thickness: Implications for two-dimensional echocardiography based on an autopsy study of 200 normal human hearts. *Am. J. Cardiol.*, 62:424–430, 1988.

[124] M.P. Sands, E.A. Rittenhouse, H.M. Mohri, and K.A. Merendino. An anatomical comparison of human, pig, calf, and sheep aortic valves. *Ann. Thorac. Surg.*, 8:407–414, 1969.

[125] A.A.H.J. Sauren. *The mechanical behaviour of the aortic valve.* PhD thesis, Technische Universiteit Eindhoven, Netherlands, 1981.

[126] A.A.H.J. Sauren, W. Kuijpers, A.A. van Steenhoven, and F.E. Veldpaus. Aortic valve histology and its relation with mechanics — preliminary report. *J. Biomechanics*, 13:97–104, 1980.

[127] A.A.H.J. Sauren, M.C. van Hout, A.A. van Steenhoven, F.E. Veldpaus, and J.D. Janssen. The mechanical properties of porcine aortic valve tissues. *J. Biomechanics*, 16:327–337, 1983.

[128] C. Schild and B. Trueb. Mechanical stress is required for high-level expression of connective tissue growth factor. *Exp. Cell Res.*, 274:83–91, 2002.

[129] D.J. Schneck. An outline of cardiovascular structure and function. In J.D. Bronzino, editor, *The Biomedical Engineering Handbook*, chapter 1. CRC Press, Boca Raton, USA(FL), 2000.

[130] M. Scott and I. Vesely. Aortic valve cusp microstructure: The role of elastin. *Ann. Thorac. Surg.*, 60:S391–S394, 1995.

[131] P.A. Shoemaker, D. Schneider, M.C. Lee, and Y.C. Fung. A constitutive model for two-dimensional soft tissues and its application to experimental data. *J. Biomechanics*, 19:695 702, 1986.

[132] M.A. Silver and W.C. Roberts. Detailed anatomy of the normally functioning aortic valve in hearts of normal and increased weight. *Am. J. Cardiol.*, 55:454–461, 1985.

[133] P. Simon, M.T. Kasimir, G. Seebacher, G. Weigel, R. Ullrich, U. Salzer-Muhar, E. Rieder, and E. Wolner. Early failure of the tissue engineered porcine heart valve synergraft$^{\text{TM}}$ in pediatric patients. *Eur. J. Cardiothorac. Surg.*, 23:1002–1006, 2003.

[134] A.J.M. Spencer. *Deformations of fibre-reinforced materials.* Oxford University Press, London, UK, 1972.

[135] C. Stefanadis, C. Stratos, H. Boudoulas, C. Kourouklis, and P. Toutouzas. Distensibility of the ascending aorta: Comparison of invasive and non-invasive techniques in healthy men and in men with coronary artery disease. *Eur. Heart J.*, 11:990–996, 1990.

[136] B.T. Stojkov. *The valve primer.* Industrial Press, New York, USA(NY), 1994.

[137] A. Sud, F. Parker, and D.J. Magilligan Jr. Anatomy of the aortic root. *Ann. Thorac. Surg.*, 38:76–79, 1984.

[138] J.P. Sutton III, S.Y. Ho, and R.H. Anderson. The forgotten interleaflet triangles: A review of the surgical anatomy of the aortic valve. *Ann. Thorac. Surg.*, 59:419–427, 1995.

[139] W.M. Swanson and R.E. Clark. Dimensions and geometric relationships of the human aortic valve as a function of pressure. *Circ. Res.*, 35:871–882, 1974.

[140] A.J.K. Tan and D.L. Holt. The effects of sterilization and storage treatments on the stress-strain behavior of aortic valve leaflets. *Ann. Thorac. Surg.*, 22:188–194, 1976.

[141] M. Thubrikar. *The aortic valve.* CRC Press, Boca Raton, USA(FL), 1990.

[142] M. Thubrikar, J.L. Heckman, and S.P. Nolan. High speed cine-radiographic study of aortic valve leaflet motion. *J. Heart Valve Dis.*, 2:653–661, 1993.

[143] M.J. Thubrikar, J. Aouad, and S.P. Nolan. Comparison of the in vivo and in vitro mechanical properties of aortic valve leaflets. *J. Thorac. Cardiovasc. Surg.*, 92:29–36, 1986.

[144] M.J. Thubrikar, W.C. Piepgrass, L.P. Bosher, and S.P. Nolan. The elastic modulus of canine aortic valve leaflets in vivo and in vitro. *Circ. Res.*, 47:792–800, 1980.

[145] R.J. van Renterghem, A.A. van Steenhoven, T. Arts, and R.S. Reneman. Deformation of the dog aortic valve ring during the cardiac cycle. *Pflügers Arch.*, 412:647–653, 1988.

[146] D.R. Veronda and R.A. Westmann. Mechanical characterization of skin — finite deformations. *J. Biomechanics*, 3:111–124, 1970.

[147] I. Vesely. The role of elastin in aortic valve mechanics. *J. Biomechanics*, 31:115–123, 1998.

[148] I. Vesely. Aortic root dilation prior to valve opening explained by passive hemodynamics. *J. Heart Valve Dis.*, 9:16–20, 2000.

[149] I. Vesely, D.R. Boughner, and J. Leeson-Dietrich. Bioprosthetic valve tissue viscoelasticity: Implications on accelerated pulse duplicator testing. *Ann. Thorac. Surg.*, 60:S379–S383, 1995.

[150] I. Vesely, D.C. Casarotto, and G. Gerosa. Mechanics of cryopreserved aortic and pulmonary homografts. *J. Heart Valve Dis.*, 9:27–37, 2000.

[151] I. Vesely, L. Gonzalez-Lavin, D. Graf, and D. Boughner. Mechanical testing of cryopreserved aortic allografts. comparison with xenograft and fresh tissue. *J. Thorac. Cardiovasc. Surg.*, 99:119–123, 1990.

[152] I. Vesely, S. Krucinski, M.A. Dokainish, and G. Campbell. An optimal mounting frame to reduce flexural stresses of bioprosthetic heart valves. *ASAIO J.*, 40:199–205, 1994.

[153] I. Vesely and A. Lozon. Natural preload of aortic valve leaflet components during glutaraldehyde fixation: Effects on tissue mechanics. *J. Biomechanics*, 26:121–131, 1993.

[154] I. Vesely, A. Lozon, and E. Talman. Is zero pressure fixation truly stress free? *J. Thorac. Cardiovasc. Surg.*, 106:288–298, 1993.

[155] I. Vesely and R. Noseworthy. Micromechanics of the fibrosa and the ventricularis in aortic valve leaflets. *J. Biomechanics*, 25:101–113, 1992.

[156] F.E.M.G. Vollebergh and A.E. Becker. Minor congenital variations of cusp size in tricuspid aortic valves. possible link with isolated aortic stenosis. *Br. Heart J.*, 39:1006–1011, 1977.

[157] W. Wegner and H. Feder. Zur gewebsmechanik der aortenwand des schweines. *Res. Exp. Med.*, 168:129–141, 1976.

[158] J.A. Weiss, B.N. Maker, and S. Govindjee. Finite element implementation of incompressible, transversely isotropic hyperelasticity. *Comput. Methods Appl. Mech. Engrg.*, 135:107–128, 1996.

[159] J.W. Weiss. *A constitutive model and finite element representation for transversely isotropic soft tissues.* PhD thesis, University of Utah, USA, 1994.

[160] S. Westaby, R.B. Kark, E.H. Blackstone, and S.P. Bishop. Adult human valve dimensions and their surgical significance. *Am. J. Cardiol.*, 53:552–556, 1984.

[161] J.E.C. Wright and Y.L. Ng. Elasticity of human aortic valve cusps. *Cardiovasc. Res.*, 8:384–390, 1974.

[162] A.P. Yoganathan. Cardiac valve prostheses. In J.D. Bronzino, editor, *The Biomedical Engineering Handbook*, chapter 127. CRC Press, Boca Raton, USA(FL), 2000.

[163] A.P. Yoganathan, J.D. Lemmon, and J.T. Ellis. Heart valve dynamics. In J.D. Bronzino, editor, *The Biomedical Engineering Handbook*, chapter 29. CRC Press, Boca Raton, USA(FL), 2000.

[164] P. Zilla, P. Human, and D. Bezuidenhout. Bioprosthetic heart valves: The need for a quantum leap. *Biotechnol. Appl. Biochem.*, 40:57–66, 2004.

[165] P. Zilla, C. Weissenstein, P. Human, T. Dower, and U.O. von Oppel. High glutaraldehyde concentrations mitigate bioprosthetic root calcification in the sheep model. *Ann. Thorac. Surg.*, 70:2091–2095, 2000.

Appendix A

Fitting of Uniaxial Tension Test Data

A.1 Uniaxial Tensile Stress

Let λ_1 be the stretch in direction of elongation in a uniaxial tension test as illustrated in Figure A.1, λ_2 the stretch in-plane but orthogonal to λ_1 and finally λ_3 in the thickness direction perpendicular to the in-plane stretches. Incompressibility

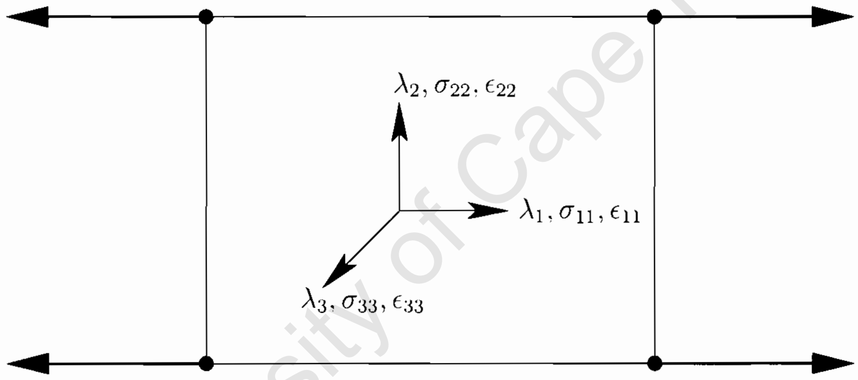

Figure A.1: In a uniaxial tension test, the 1- and 11-directions are in the direction of elongation, the 2- and 22-directions in-plane perpendicular to the former, and finally the 3- and 33-directions normal to the planar specimen.

then dictates

$$\det \mathbf{F} = \lambda_1 \lambda_2 \lambda_3 = 1 \;\Rightarrow\; \lambda_2 = \lambda_3 = \lambda_1^{-\frac{1}{2}}. \tag{A.1}$$

The deformation gradient in this case is the diagonal

$$\mathbf{F} = \begin{pmatrix} \lambda_1 & 0 & 0 \\ 0 & \lambda_1^{-\frac{1}{2}} & 0 \\ 0 & 0 & \lambda_1^{-\frac{1}{2}} \end{pmatrix}, \tag{A.2}$$

and the left and right Cauchy-Green tensors are the identical

$$\mathbf{F}^T \cdot \mathbf{F} = \mathbf{F} \cdot \mathbf{F}^T = \begin{pmatrix} \lambda_1^2 & 0 & 0 \\ 0 & \lambda_1^{-1} & 0 \\ 0 & 0 & \lambda_1^{-1} \end{pmatrix}. \tag{A.3}$$

The Cauchy stresses from Section 3.2.4 are equations (3.74), where the stress response is derived from a decoupled strain energy potential $U = U_1 + U_4$ as in equation (3.75),

$$\boldsymbol{\sigma} = 2\left\{ \frac{\partial U_1}{\partial I_1} \mathbf{B} + I_4 \frac{\partial U_4}{\partial I_4} \mathbf{a} \otimes \mathbf{a} \right\} + p\mathbb{I}, \tag{A.4}$$

to which the plane stress assumption is applied with the additional restriction that the fibres **a** remain in-plane,

$$\sigma_{33} = 2\frac{\partial U_1}{\partial I_1} B_{33} + p = 0 \;\Leftrightarrow\; p = -2\frac{\partial U}{\partial I_1}\lambda_1^{-1}. \tag{A.5}$$

If the elongation is perpendicular to the direction of the fibres, e.g. in the radial leaflet direction, and the fibres don't carry compressive stresses (like they were defined in Section 3.2.4), it then follows $\sigma_{22} = 0$ as required, and the stress component in the direction of elongation is

$$\sigma_{11} = 2\frac{\partial U_1}{\partial I_1}\left(\lambda_1^2 - \lambda_1^{-1}\right). \tag{A.6}$$

Specifically, using the strain energy potential for the leaflet matrix from Section 3.2.4 equation (3.76),

$$U_1 = \frac{c_{12}}{2c_{11}}\left(e^{c_{11}(I_1 - 3)} - 1\right), \tag{A.7}$$

with its first derivative

$$\frac{\partial U_1}{\partial I_1} = \frac{c_{12}}{2} e^{c_{11}(I_1 - 3)}. \tag{A.8}$$

and introducing logarithmic strain

$$\epsilon_{11} = \ln \lambda_1 \;\Leftrightarrow\; \lambda_1 = e^{\epsilon_{11}}, \tag{A.9}$$

the uniaxial stress as a function of logarithmic strain reads

$$\sigma_{11} = c_{12}\, e^{c_{11}(e^{2\epsilon_{11}}+2e^{-\epsilon_{11}}-3)} \left(e^{2\epsilon_{11}} - e^{-\epsilon_{11}}\right). \tag{A.10}$$

If the fibres $\mathbf{a}_0$ are parallel and the elongation is in the direction of the fibres, a fibre stress term σ_f has to added to equation (A.6),

$$\sigma_f = 2\, I_4 \frac{\partial U_4}{\partial I_4}, \tag{A.11}$$

which follows from equation (A.4) and from the deformation gradient equation (A.2) applied to the vector field $\mathbf{a}_0$ that now is in the direction of elongation and hence

$$\mathbf{a} \otimes \mathbf{a} = \begin{pmatrix} 1 & 0 & 0 \\ 0 & 0 & 0 \\ 0 & 0 & 0 \end{pmatrix}. \tag{A.12}$$

For the strain energy potential of the fibre part equation (3.77) proposed in Section 3.2.4

$$U_4 = \frac{c_{42}}{2c_{41}}(e^{c_{41}(I_4-1)^2} - 1), \tag{A.13}$$

with its first derivative

$$\frac{\partial U_4}{\partial I_4} = c_{42}(I_4 - 1)\, e^{c_{41}(I_4-1)^2}, \tag{A.14}$$

and noting that $I_4 = \lambda_f^2 = \lambda_1^2$, the fibre stress results in

$$\sigma_f = 2\, c_{42} \left(e^{4\epsilon_{11}} - e^{2\epsilon_{11}}\right) e^{c_{41}(e^{2\epsilon_{11}}-1)^2}. \tag{A.15}$$

A.2 Data Fitting

The stresses of the previous sections as functions of logarithmic strain can be fitted to uniaxial tension test data, e.g. the test results for aortic valve leaflets of Section 2.2.4. The starting point is the stress of the matrix equation (A.10).

That function is fitted to data of a tension test perpendicular to fibres. i.e. in the case of aortic valve leaflets the radial direction. Having thus established the two constants c_{11} and c_{12}. the sum of equation (A.10) and equation (A.15) is fitted to test data along the fibre direction, i.e. the circumferential direction in aortic valve leaflets. That determines the fibre properties c_{41} and c_{42}.

In the case where the fibre behaviour clearly dominates the stress response along the fibres. the matrix contribution equation (A.10) can be neglected to simplify the determination of fibre properties c_{41} and c_{42}. Since this is evident in aortic valve leaflet mechanics, that route has been taken.

Fitting was carried out using the GNUPLOT implementation of the non-linear least-squares Marquardt-Levenberg algorithm [50].

Appendix B

Implementation of U_1 in ABAQUS

B.1 Requirements

The exponential strain energy function equation (3.76)

$$U_1 = \frac{c_{12}}{2c_{11}} \left(e^{c_{11}(I_1-3)} - 1\right) \tag{B.1}$$

is not available in ABAQUS. However, the software provides an interface to program any isotropic strain energy function of invariants I_1, I_2 and I_3 via the user supplied subroutine UHYPER.

The implementation of this subroutine is straightforward. In addition to the strain energy function itself, it only requires the derivatives with respect to the invariants as code. In the case of equation (B.1) these read

$$U_{1,1} = \frac{\partial U_1}{\partial I_1} = \frac{c_{12}}{2} e^{c_{11}(I_1-3)} \quad \text{and} \tag{B.2}$$

$$U_{1,11} = \frac{\partial^2 U_1}{\partial I_1^2} = \frac{c_{11}c_{12}}{2} e^{c_{11}(I_1-3)} \; . \tag{B.3}$$

Since U_1 is a function of I_1 only and incompressibility $I_3 = 1$ is assumed, all other derivatives vanish.

B.2 Implementation

The user supplied subroutine UHYPER implementing equation (B.1) in FORTRAN77 is listed in Table B.2. The parameters c_{11} and c_{12} are specified in the input file of the model and are available in the subroutine in the array `PROPS`.

```
      SUBROUTINE UHYPER(BI1,BI2,AJ,U,UI1,UI2,UI3,TEMP,NOEL,CMNAME,
     $                  INCMPFLAG,NUMSTATEV,STATEV,NUMFIELDV,
     $                  FIELDV,FIELDVINC,NUMPROPS,PROPS)
C
      INCLUDE 'ABA_PARAM.INC'
C
      CHARACTER*80 CMNAME
      DIMENSION UI1(3),UI2(6),UI3(6)
     $          ,STATEV(*),FIELDV(*),
     $          FIELDVINC(*),PROPS(*)
C
      PARAMETER (ZERO=0.0D0,ONE=1.0D0, TWO=2.0D0, THREE=3.0D0)
C
      C1 = PROPS(1)
      C2 = PROPS(2)
C
C    DEFINING STRAIN ENERGY AND DERIVATIVES
C
      ETERM=(C2/TWO)*EXP(C1*(BI1-THREE))
      U=(ETERM-C2/TWO)/C1
      UI1(1)=ETERM
      UI2(1)=C1*ETERM
C
      UI1(2)=ZERO
      UI1(3)=ZERO
      UI2(2)=ZERO
      UI2(3)=ZERO
      UI2(4)=ZERO
      UI2(5)=ZERO
      UI2(6)=ZERO
      UI3(1)=ZERO
      UI3(2)=ZERO
      UI3(3)=ZERO
      UI3(4)=ZERO
      UI3(5)=ZERO
      UI3(6)=ZERO
      RETURN
      END
```

Table B.1: Listing of subroutine UHYPER

Appendix C

Implementation of U_4 in ABAQUS

C.1 Requirements

It was discussed in Section 3.3.4 that the transverse direction is introduced in the elements with REBARS, the ABAQUS feature to define reinforcement in elements. REBARS basically define the vector field $\mathbf{a}_0$ and are furthermore assigned material properties distinct from those of the parent element. However, ABAQUS does not support the assignment of hyperelastic material behaviour for the REBARS, but provides a means to incorporate hyperelastic fibres by means of a user supplied subroutine, UMAT.

The subroutine has to calculate the stresses and the tangent elastic moduli for the constitutive model in the current configuration. For the constitutive models proposed in Section 3.2 the respective fibre contributions have to be coded in UMAT.

The fibre contribution to Cauchy stress reads

$$\boldsymbol{\sigma}_f = 2\left\{ I_4 \frac{\partial U_4}{\partial I_4} \mathbf{a} \otimes \mathbf{a} \right\}, \tag{C.1}$$

and its tangent moduli

$$\mathfrak{C}_f = \frac{\partial^2 U_4}{\partial I_4^2} I_4^2 \mathbf{a} \otimes \mathbf{a} \otimes \mathbf{a} \otimes \mathbf{a}. \tag{C.2}$$

The strain energy potential for the fibres is U_4

$$U_4 = \frac{c_{42}}{2c_{41}} (e^{c_{41}(I_4-1)^2} - 1), \tag{C.3}$$

whose first and second derivatives enter equation (C.1) and equation (C.2) and are

$$\frac{\partial U_4}{\partial I_4} = c_{42}(I_4 - 1)\, e^{c_{41}(I_4-1)^2}, \text{ and} \tag{C.4}$$

$$\frac{\partial^2 U_4}{\partial I_4^2} = \left\{1 + 2\, c_{41}\, (I_4 - 1)^2\right\}\, c_{42}\, e^{c_{41}(I_4-1)^2}. \tag{C.5}$$

C.2 Implementation

The FORTRAN77 listing of subroutine UMAT implementing U_4 can be found in Table C.2. ABAQUS takes care of rotations of the REBARS, so that **a** in the stress and tangent moduli calculations of the previous sections is always in the 1-direction. Consequently, the tensors formed by **a** can be dropped and what is left is the only component that needs to be implemented, `STRESS(1)` the fibre stress and `DDSDDE(1,1)` the tangent modulus. The invariant I_4 is labelled `FS` in the subroutine and calculated from the logarithmic strain that is passed in from ABAQUS.

The derivatives of the strain energy potential U_4 are coded in variables `U4` and `U44`, that take the two constants `C41` and `C42` passed in via the `PROPS` array.

```
      SUBROUTINE UMAT(STRESS,STATEV,DDSDDE,SSE,SPD,SCD,
     1 RPL,DDSDDT,DRPLDE,DRPLDT,STRAN,DSTRAN,
     2 TIME,DTIME,TEMP,DTEMP,PREDEF,DPRED,MATERL,NDI,NSHR,NTENS,
     3 NSTATV,PROPS,NPROPS,COORDS,DROT,PNEWDT,CELENT,
     4 DFGRD0,DFGRD1,NOEL,NPT,KSLAY,KSPT,KSTEP,KINC)
C
      INCLUDE 'ABA_PARAM.INC'
C
      CHARACTER*8 MATERL
      DIMENSION STRESS(NTENS),STATEV(NSTATV),
     1 DDSDDE(NTENS,NTENS),DDSDDT(NTENS),DRPLDE(NTENS),
     2 STRAN(NTENS),DSTRAN(NTENS),DFGRD0(3,3),DFGRD1(3,3),
     3 TIME(2),PREDEF(1),DPRED(1),PROPS(NPROPS),COORDS(3),DROT(3,3)
C
C      DIMENSION INTV(2), REALV(1)
C CHARACTER*8 CHARV(1)
      PARAMETER(ZERO=0.D0, ONE=1.D0, TWO=2.D0, THREE=3.D0, FOUR=4.D0)
C
C    ELASTIC PROPERTIES
C
C41=PROPS(1)
C42=PROPS(2)
C
C    TOTAL STRAIN AND FS (FIBRE STRETCH SQUARED, INVARIANT I4)
C
TSTRAN=STRAN(1)+DSTRAN(1)
FS=EXP(2*TSTRAN)
C
C    ELASTIC STIFFNESS AND STRESS
C
IF(FS.GE.ONE) THEN
  EXPTERM=C42*EXP(C41*(FS-ONE)**TWO)
  U4=(FS-ONE)*EXPTERM
  U44=(ONE+TWO*C41*(FS-ONE)**TWO)*EXPTERM
  STRESS(1)=TWO*FS*U4
  DDSDDE(1,1)=FOUR*FS**TWO*U44
ELSE
  STRESS(1)=ZERO
  DDSDDE(1,1)=ZERO
END IF
C
      RETURN
      END
```

Table C.1: Listing of subroutine UMAT